CRS4

Centre for Advanced Studies, Research
and Development in Sardinia
Cagliari - Italy

BRITE-Euram
— Low NOx III —
Project number: BE 95-1381
Contract number: BRPR CT95-0122

Theme V, Task 2: Reduced Reaction Mechanisms

CRS4 Final Deliverable

Dicembre, 1999

Prepared by:
M.C. Barbato

Fluid Dynamics and Combustion Area
Tel. +39 070 2796 - 258; Fax: -216;
E-mail barbato@crs4.it

Contents

Chapter 1

Activity Summary

1.1 Introduction

The present document reports about CRS4 activity for the task 2 of theme V of the LowNOx III project. In this Chapter a summary of what has been done at CRS4 during this time is presented. In the following Chapters a description of the physical models and computational tools used for the calculation is done. In Chapter 2 the combustion model specially implemented to afford calculation of combustion flows in different combustion regimes is presented. Chapter 3 and 4 concern the combustion model validation. Chapter 5 and 6 present ILDM and classical approaches to reduced chemistry. ILDM software testing is proposed in Chapter 7. A simple application of the Combustion model package EDC+PSR, developed for the CFX code, is presented in Chapter 8.

Finally a series of appendixes gives the necessary documentation for the EDC+PSR software package.

1.2 Activity description

The CRS4 task was to test CFD applicability of the reduced reaction mechanisms set up by the University of Heidelberg in the framework of the LowNOx II - Type II Project.

To be able to simulate several combustion regimes, i.e. non-premixed, partially-premixed and premixed, and to account for chemical kinetics, the Eddy Dissipation Concept (EDC) of Magnussen [1] has been chosen to model turbulent combustion. The CFD platform used is a code developed at CRS4 named `GTTURBO` which has been designed to simulate non-premixed turbulent flames with a PDF approach. The numerics of this code is inspired to the standard approach of pressure-based codes [2] which is the most diffuse in research and commercial CFD package suitable for turbulent combustion simulations.

The CRS4 activity in this project can therefore be summarized in the following steps:

- definition of which CFD platform and turbulent combustion model are suitable for the activity assigned;
- preliminary testing of the CFD code on non-premixed flames using conventional reduced reaction mechanisms;
- definition of the turbulent combustion model EDC+PSR ;
- implementation of the EDC+PSR model;
- testing of the model using conventional reduced reaction mechanisms;
- implementation of ILDM tables already available, i.e., for $CO-H_2$ and for CH_4 combustion in air;
- testing of the CFD code with ILDM tables;
- definition of *pro* and *cons* of the tables in their initial structure;
- definition of a series of features for the design of *optimal* tables suitable for LowNOx CFD users;
- design of a software package for the EDC+PSR combustion model to distribute to Project partners.

Chapter 2

CFD Code Description

2.1 Introduction

The code used by CRS4 for the CFD simulations is the `GTTURBO` [3] code developed in house. It is a 2D/axisymmetric code suitable for turbulent combustion flows. In the next paragraphs the physics and the numerics plus the structure of the code will be described.

2.2 Physics

i **Gas-dynamics equations**: Gasdynamics is modeled using the multicomponent Navier-Stokes equations for incompressible flow of an ideal gas. Variation of density are allowed only as due to heat release (pressure based approach).

vi **turbulence**: The turbulent nature of the flow is modeled using a two equations $k-\epsilon$ (standard) model.

vii **Combustion and Chemistry** Combustion and its interaction with turbulence is modeled using the Eddy Dissipation Concept of Magnussen and detailed chemistry is accounted for coupling this model with a Perfect Stirred Reactor solver.

2.3 Numerics

i **Kind of space discretization**: The numerical formulation of the code is based on a Finite Volume approach which follows the approach suggested by Patankar. [2].

ii **Type and features of computational grid**: the code uses non-staggered structured grids with multi-block policy.

iv **Numerical scheme and solution procedure**: The solution procedure is the traditional SIMPLE algorithm [2]. The scheme used to discretize the convection-diffusion equations is either a hybrid central-upwind scheme [2] or a *TVD* (Total Variation Diminishing) scheme proposed by Jones [4].

vi **Accuracy**: the code is first order accurate with hybrid central-upwind scheme and second order accurate with the *TVD* scheme.

2.4 Model equations

2.4.1 Total mass

$$\frac{\partial \rho}{\partial t} + \nabla \cdot (\rho \, \mathbf{u}) = 0 \tag{2.1}$$

where ρ is the mass density and $\mathbf{u}$ is the velocity vector.

2.4.2 Mass of chemical species

$$\frac{\partial (\rho \, Y_j)}{\partial t} + \nabla \cdot (\rho \, \mathbf{u} \, Y_j) = \nabla \cdot (\rho \, \mathcal{D}_j \, \nabla Y_j) + W_j \, w_j \qquad j = 1, ..., NS \tag{2.2}$$

where for the generic chemical species J, Y_j is the mass fraction, w_j is the chemical source term and where molecular diffusion has been approximated via the Fick's law:

$$\rho \, Y_j \, \mathbf{U}_{d,j} = -\rho \mathcal{D}_j \, \nabla Y_j \tag{2.3}$$

$\mathcal{D}_j$ being the molecular diffusion coefficient for species j.

2.4.3 Momentum

$$\frac{\partial (\rho \, \mathbf{u})}{\partial t} + \nabla \cdot (\rho \, \mathbf{u} \, \mathbf{u}) = \rho \, \mathbf{g} + \nabla \cdot \mathbf{T} \tag{2.4}$$

where the stress tensor $\mathbf{T}$ reads [5]:

$$\mathbf{T} = -p \, \mathbf{I} + 2 \, \mu \, \left[\mathbf{E} - \frac{1}{3} (\nabla \cdot \mathbf{u}) \mathbf{I} \right] \tag{2.5}$$

with a spherical (pressure) and a deviatoric contribution. In the latter μ is the fluid viscosity and $\mathbf{E}$ is the deviatoric part of the deformation velocity:

$$\mathbf{E} = \frac{\nabla \mathbf{u} + (\nabla \mathbf{u})^T}{2} \quad . \tag{2.6}$$

2.4.4 Energy

$$\frac{\partial(\rho\, h)}{\partial t} + \nabla\cdot(\rho\,\mathbf{u}\, h) = \frac{Dp}{Dt} - \nabla\cdot(\mathbf{q}_c + \mathbf{q}_r + \sum_{j=1}^{NS} \rho\, Y_j\, \mathbf{U}_{d,j}\, h_j) + \underbrace{\underline{\mathbf{S}} : \underline{\mathbf{E}}}_{\Phi} \tag{2.7}$$

where $\mathbf{q}_c = -k\,\nabla T$ is the convective heat flux (k, molecular heat transfer coefficient) and $\mathbf{q}_r$ is the radiative heat flux. The term Φ represents the dissipation (into heat) of the kinetic energy, which is a strictly positive term; h_j is the specific enthalpy (for unit of mass) of the chemical species j:

$$h_j = \Delta h^0_{f,j} + \int_{T_0}^{T} C_{p,j}(\xi)\, d\xi \tag{2.8}$$

where $\Delta h^0_{f,j}$ is the formation contribution and $C_{p,j}(T)$ the specific heat.

(

Simplified expression) A considerable simplification can be made on the enthalpy equation on the basis of the following assumptions:

1. pressure term Dp/Dt negligible (acceptable for flows where $M^2 \ll 1$);
2. viscous dissipation term Φ negligible with respect the heat released by combustion (reasonable if $M \ll 1$);
3. molecular diffusion coefficient equal for all chemical species, i.e. $\mathcal{D}_1 = \mathcal{D}_2 = \ldots = \mathcal{D}_{NS} = \mathcal{D}$;
4. Lewis number equal one, i.e. $Le = \rho\,\mathcal{D}/(k/C_p) = 1$ where $\overline{C_p} = \sum_{j=1}^{NS} Y_j\, C_{p,j}$ is the specific heat of the chemical mixture;
5. adiabatic and non catalytic walls;
6. radiation term $\mathbf{q}_r$ negligible.

Finally the enthalpy conservation equation becomes an transport equation without source term:

$$\frac{\partial(\rho\, h)}{\partial t} + \nabla\cdot(\rho\,\mathbf{u}\, h) = \nabla\cdot(\rho\,\mathcal{D}\,\nabla h) \tag{2.9}$$

2.5 Reynolds averaged Navier-Stokes equations

2.5.1 Introduction

The approach commonly used for the numerical simulation of turbulent flows is based on the solution of conservation equations for the statistical averages (ensemble averages).

Conservation equations for time averaged quantities can be obtained applying the averaging operator to the instantaneous N-S equations. Unfortunately, second order correlation terms between turbulent fluctuations arise; these are generated by non linear contributions in the equations, i.e. convective transport and chemical source terms. For example, in the case of convective transport, considering for simplicity a constant density flow, it is:

$$\overline{\mathbf{u}\,\phi} = \overline{\mathbf{u}}\,\overline{\phi} + \overline{\mathbf{u}'\,\phi'} \tag{2.10}$$

where the term $\overline{\mathbf{u}'\,\phi'}$ represents transport of ϕ due to turbulence and it is an additional unknown of the problem for which doesn't exist and equation; the problem becomes undetermined. For this unknown a constitutive relation has to be postulated, i.e. a closure problem rises.

When dealing with density-varying flows, to average the equations, it is more convenient to use Favre averaging, i.e. weighted averaging with local density:

$$\tilde{\phi} = \frac{\overline{\rho\,\phi}}{\overline{\rho}} \tag{2.11}$$

$$\phi = \tilde{\phi} + \phi'' \tag{2.12}$$

in fact in this way, less correlation terms arise. In the following Sections the averaged transport equations for a stationary flow will be presented.

2.5.2 Total mass

$$\nabla \cdot (\overline{\rho}\,\tilde{\mathbf{u}}) = 0 \tag{2.13}$$

2.5.3 Mass of chemical species

$$\nabla \cdot (\overline{\rho}\,\tilde{\mathbf{u}}\,\tilde{Y}_j) + \nabla \cdot (\overline{\rho}\,\widetilde{\mathbf{u}''\,Y_j''}) = \nabla \cdot (\rho\,\mathcal{D}\,\nabla \tilde{Y}_j) + W_j\,\overline{w_j} \tag{2.14}$$

Closure have to be defined for the chemical source term and the turbulent transport term (Reynolds flux). To show why $\overline{w_j}$ needs closure, we consider a simple example: a bimolecular reaction of the type $A + B \rightarrow C$ whose reaction rate is given by $w_f = \exp(-T_a/T)\,c_A\,c_B$; developing it according to a Taylor series expansion up to the second order (around the initial point $\overline{T}$, $\overline{c_A}$, $\overline{c_B}$) and taking its time average yields:

$$\overline{\omega_f} = \underbrace{\exp(-T_a/\overline{T})\,\overline{c_A}\,\overline{c_B}}_{\omega_f(\overline{T},\overline{c_A},\overline{c_B})} \left[1 + \left(\frac{{T_a}^2}{\overline{\overline{T}}^2} - 2\,\frac{T_a}{\overline{\overline{T}}}\right)\frac{\overline{T'^2}}{\overline{\overline{T}}^2} + \frac{T_a}{\overline{\overline{T}}}\left(\frac{\overline{T'\,c_A'}}{\overline{\overline{T}}\,\overline{c_A}} + \frac{\overline{T'\,c_B'}}{\text{ø}verline T\,\overline{c_B}}\right) + \ldots\right] \tag{2.15}$$

This expression shows that in the case of intense turbulence and large $T_a/\overline{T}$ ratio (this is very common in turbulent combustion), it is not possible to approximate the average of the reaction rate $\overline{w_f}$ with the reaction rate calculated as $w_f(\overline{T}, \overline{c_A}, \overline{c_B})$; on the contrary, turbulent fluctuations assume a very important role and therefore many closures have to be formulated for the correlations in the Taylor series expansion Eq. (2.15). Considering also that in combustion it is possible to have up to $70-80$ chemical species for the most complex hydrocarbons, it is clear that the number of correlations to model becomes prohibitively large; some method to reduce the number of thermochemical independent parameters and the number of correlations to model is necessary.

2.5.4 Momentum

$$\nabla\cdot(\overline{\rho}\,\tilde{\mathbf{u}}\,\tilde{\mathbf{u}}) = -\nabla\overline{p} + \nabla\cdot\left[2\,\mu\,\left(\tilde{\mathbf{E}} - \frac{1}{3}(\nabla\cdot\tilde{\mathbf{u}})\,\mathbf{I}\right) - \overline{\rho}\,\widetilde{\mathbf{u}''\,\mathbf{u}''}\right] \tag{2.16}$$

where the molecular viscosity μ has been assumed constant and the time average of $\mathbf{E}$ has been approximated with the Favre counterpart[1]. The closure of the turbulent transport tensor $-\overline{\rho}\,\widetilde{\mathbf{u}''\,\mathbf{u}''}$ (Reynolds stresses tensor) is obtained as:

$$-\overline{\rho}\,\widetilde{\mathbf{u}''\mathbf{u}''} = 2\mu_t\left[\frac{\nabla\tilde{\mathbf{u}} + \nabla\tilde{\mathbf{u}}^T}{2} - \frac{1}{3}\,(\nabla\cdot\tilde{\mathbf{u}})\,\mathbf{I}\right] - \frac{2}{3}\,k\,\mathbf{I} \tag{2.17}$$

The turbulent viscosity μ_t reads:

$$\mu_t = c_\mu\,\overline{\rho}\,\frac{k^2}{\epsilon} \tag{2.18}$$

where k is the turbulent kinetic energy and ϵ is its dissipation rate.

2.5.5 Enthalpy

The enthalpy equation has been put in the form of mixture fraction f:

$$\nabla\cdot(\overline{\rho}\,\tilde{\mathbf{u}}\,\tilde{f}) + \nabla\cdot(\overline{\rho}\,\widetilde{\mathbf{u}''\,f''}) = \nabla\cdot(\rho\,\mathcal{D}\,\nabla\tilde{f}) \tag{2.19}$$

---

[1] These approximations are reasonable in the case of high Reynolds number flows where the ratio between turbulent and molecular transport is much larger than unity.

where:

$$f = \frac{h - h_{,a}}{h_{,f} - h_{,a}} = \frac{Z_i - Z_{i,a}}{Z_{i,f} - Z_{i,a}} \tag{2.20}$$

and

$$Z_i = \sum_{j=1}^{NS} a_{ij} \frac{W_i^{(e)}}{W_j} Y_j, \qquad i = 1, ..., NE \tag{2.21}$$

Z_i is the mass fraction of element i and a_{ij} the number of atoms in one molecule of species j ($W_i^{(e)}$ and W_j being respectively atomic and molecular weights).

2.6 Turbulence equations

2.6.1 $\kappa - \epsilon$ equations

The transport equations for k and ϵ are given by:

$$\nabla \cdot (\rho\, \tilde{\mathbf{u}}\, k) = \nabla \cdot \left(\frac{\mu_t}{\sigma_k} \nabla k\right) + P_k - \rho\epsilon \tag{2.22}$$

$$\nabla \cdot (\rho\, \tilde{\mathbf{u}}\, \epsilon) = \nabla \cdot \left(\frac{\mu_t}{\sigma_\epsilon} \nabla \epsilon\right) + P_\epsilon - c_2\, \rho\, \frac{\epsilon^2}{k} \tag{2.23}$$

where turbulent diffusion coefficients for k and ϵ have been taken proportional to the turbulent viscosity according to the Prandtl analogy (σ_k, σ_ϵ turbulent Prandtl numbers).

The production of turbulent kinetic energy, P_k, and the production of its dissipation rate,P_ϵ, are given by:

$$P_k = 2\,\mu_t \frac{\nabla\tilde{\mathbf{u}} + \nabla\tilde{\mathbf{u}}^T}{2} : \frac{\nabla\tilde{\mathbf{u}} + \nabla\tilde{\mathbf{u}}^T}{2} - \frac{2}{3}(\nabla \cdot \tilde{\mathbf{u}})\ [\mu_t(\nabla \cdot \tilde{\mathbf{u}}) + k] \tag{2.24}$$

$$P_\epsilon = c_1 \frac{\epsilon}{k} P_k \tag{2.25}$$

where $c_\mu = 0.09$, $c_1 = 1.44$, $c_2 = 1.92$, $\sigma_k = 1.0$, $\sigma_\epsilon = 1.3$ (standard $k - \epsilon$ coefficients).

been

2.7 Turbulent combustion: EDC combustion model

2.7.1 Combustion model overview

The Eddy Dissipation Concept (EDC) of Magnussen [1] is an approach to treat the interaction between chemistry and turbulence in flames. It is based on a physical modeling of turbulent processes which are relevant to turbulent combustion [6].

The concept is based on the idea that chemical species react when are mixed at molecular scale provided a sufficiently high temperature, and that turbulent fine structures can be assumed as chemical reactors.

2.7.2 Fine structures

Turbulent fine structures can be characterized looking at the process of energy cascade in a turbulent flow. This process is schematically represented in Fig. 2.1 taken from [1]: there we see how turbulent kinetic energy is transferred first from the mean flow to the largest eddies then to smaller up to the smallest eddies. These latter eddies are those where the major part of the mechanical energy dissipation into heat occurs. These smallest eddies structures are the so called *fine structures*.

Experimental studies on high Reynolds number turbulent flows [7], where a strong tendency to dissipation intermittency has been found, have shown that fine structures are not uniformly distributed in the flow but are concentrated in isolated regions called here *fine structures regions* [1]. The volume occupied by these regions is only a small fraction of that of the entire fluid [7] but sensibly larger than those of fine structures themselves.

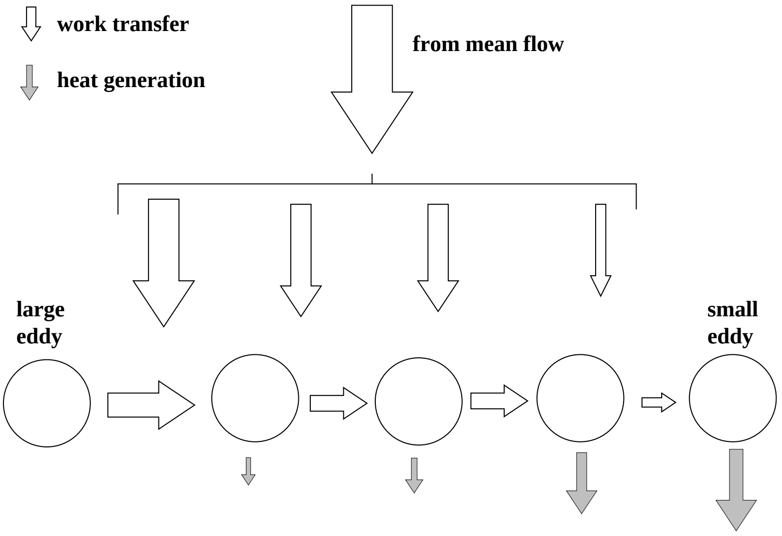

Figure 2.1: Classical concept for turbulent energy transfer. [1].

2.7.3 Homogeneous chemical reactor

Fine structures are assumed to be fluid zones where perfect mixing at molecular level is realized. In these structures, in the case of a reacting gas mixture, the assumption of perfect mixing, provided a sufficiently high temperature, means also chemical reactions. Therefore they can be assumed as being Well Stirred Reactors (see Fig. 2.2) where conversion from reactants to products is controlled by chemical rates and not by turbulent mixing of reactants.

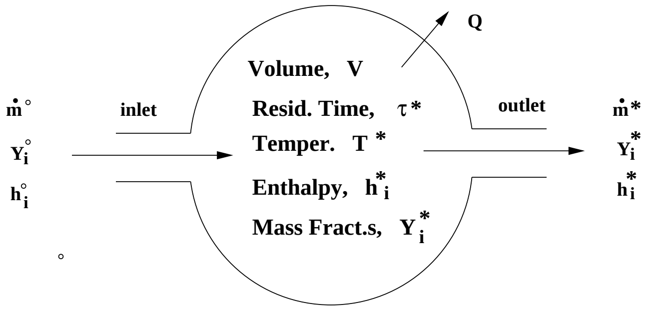

Figure 2.2: Schematic representation of a Well Stirred Reactor. From [8].

2.7.4 EDC-PSR combustion model

The EDC-PSR Combustion Model is based on the considerations presented above: for a turbulent combustion flow, the theory of Magnussen, by modeling the interaction between chemical reactions and turbulence, make possible to write the chemical source terms for the mean chemical species transport equations (Eqs. 2.14). Then, the model quantities related to fine structures, i.e. mixture composition and temperature, can be obtained modeling these structures using the Perfect Stirred Reactor (PSR) equations. Main features of this approach are shown in the following sections.

2.7.5 Model characteristic quantities

In this section the EDC model characteristic quantities are presented. For the derivation of them from the basics phenomena of turbulence see [9] and [1].

Magnussen, starting from the concept of fine structures located into fine structure regions dispersed in the mean fluid, identifies three fluid entities in the turbulent flow: the fine structures, the "surrounding fluid" i.e., the fluid in which they are plunged and with which they can exchange mass and energy, and finally the mean fluid. In the following quantities related with the surrounding fluid will be identified with the superscript ^{0} whereas quantities related to fine structures will be labeled with the superscript *. Mean fluid quantities will be overlined with a tilde.

The general relation between mean, fine structures and surrounding fluid quantities reads:

$$\tilde{\psi} = \gamma^* \chi \psi^* + (1 - \gamma^* \chi) \psi^o \quad . \tag{2.26}$$

For example for a generic mass fraction Y_i it is:

$$\tilde{Y}_i = Y_i^* \gamma^* \chi + (1 - \gamma^* \chi) Y_i^o \quad . \tag{2.27}$$

For mass density it is:

$$\frac{1}{\bar{\rho}} = \frac{\gamma^* \chi}{\rho^*} + \frac{1 - \gamma^* \chi}{\rho^o} \tag{2.28}$$

In these expressions the mass fraction of fine structure γ^* reads [1]:

$$\gamma^* = (\frac{3}{4} \frac{C_{D2}}{C_{D1}^2})^{3/4} (\frac{\nu^* \varepsilon}{\kappa^2})^{3/4} \tag{2.29}$$

where $C_{D1} = 0.134$ and $C_{D2} = 0.5$. The expression for the mass fraction of fine structure regions is [1]:

$$\gamma = (\frac{3}{4} \frac{C_{D2}}{C_{D1}^2})^{1/4} (\frac{\nu^* \varepsilon}{\kappa^2})^{1/4} \tag{2.30}$$

Assuming a steady state exchange of mass between fine structures and surrounding fluid, the mass flow rate through fine structures per unit mass can be expressed as:

$$\dot{m}^* = (\frac{3}{C_{D2}})^{1/2} (\frac{\varepsilon}{\nu^*})^{1/2} \tag{2.31}$$

The residence time into fine structures can be expressed as:

$$\tau^* = \frac{1}{\dot{m}^*} \tag{2.32}$$

and it is smaller than the Kolmogorov time scale $\tau_K = (\nu/\epsilon)^{1/2}$, in fact:

$$\tau^* = (\frac{C_{D2}}{3})^{1/2} (\frac{\nu^*}{\varepsilon})^{1/2} = (\frac{C_{D2}}{3})^{1/2} \tau_K \quad . \tag{2.33}$$

2.7.6 EDC source terms assessment

The EDC model assumes that only part of the fine structures are able to burn. Therefore a quantity χ is used to model the fraction of fine structures actually burning. This fraction is formed by two contributions:

$$\chi = \chi_h \cdot R_{ij} \tag{2.34}$$

The first factor on the RHS represents the degree of heating, and the second factor represents the probability of simultaneous presence of the reactants. For χ_h it is:

$$\chi_h = \begin{cases} \beta & \text{if} \quad \beta < 1 \\ 1 & \text{if} \quad \beta \geq 1 \end{cases} \tag{2.35}$$

with

$$\beta = \frac{1}{\gamma} \cdot \frac{\tilde{Y}_{pr}/(1+r_{fu})}{(\tilde{Y}_{pr}/(1+r_{fu}) + Y_{mim})} \tag{2.36}$$

and where r_{fu} is the stoichiometric air to fuel ratio (on mass basis) for complete combustion. Y_{min} is defined as:

$$Y_{min} = \begin{cases} \tilde{Y}_{fu} & \text{if} \quad \tilde{Y}_{fu} \leq (Y_{fu})_{st} \\ \tilde{Y}_{ox}/r_{fu} & \text{if} \quad \tilde{Y}_{fu} > (Y_{fu})_{st} \end{cases} \tag{2.37}$$

Notice that the expression:

$$\frac{\tilde{Y}_{pr}/(1+r_{fu})}{(\tilde{Y}_{pr}/(1+r_{fu}) + Y_{mim})} \tag{2.38}$$

represents the ratio between the reacted fuel mean concentration and the total burning fuel mean concentration.

In the previous equations the mass fraction of fuel species includes all the intermediates species that have the characteristics of a combustible, i.e.:

$$\tilde{Y}_{fu} = \sum_{i=1}^{NF} \frac{r_i}{r_{fu}} \tilde{Y}_i \tag{2.39}$$

where NF is the number of species with characteristics of a fuel, r_i is the stoichiometric air to fuel ratio on mass basis when species i is completely converted to H_2O and CO_2.

For R_{ij} it is:

$$R_{ij} = \frac{(\tilde{Y}_{pr}/(1+r_{fu}) + Y_{mim})^2}{(\tilde{Y}_{pr}/(1+r_{fu}) + \tilde{Y}_{fu})(\tilde{Y}_{pr}/(1+r_{fu}) + \tilde{Y}_{ox}/r_{fu})} \tag{2.40}$$

In many applications of the EDC model [10] [11] a simplifying assumption is made for the fraction of burning fine structures. In these works it is assumed that the whole fine structures burn, i.e., $\chi = 1$. This assumption has been adopted in this work also.

PSR equations

Fine structures can be thought as being Well Stirred Reactors. The latter can be modeled as *Perfect Stirred Reactors* (PSRs) i.e., ideal systems where the mixing rates are assumed to be infinitely fast [8]. In this "well-mixed" limit, there is negligible turbulence effect on mean chemical production and it can be assumed non depending on turbulent fluctuations [12]. This is the main assumption of this turbulent combustion model.

A PSR is an ideal apparatus into which there is a continuous supply of perfectly mixed reactant mixture and, through reactions, a continuous outflow of products (see Fig. 2.2). The PSR, besides mass exchange, allows also energy exchange with the surroundings (heat can be supplied or subtracted to the PSR during operation).

The modeling equations for the PSR are [8]:

$$\dot{m}(Y_i - Y_i^\circ) - \dot{\omega}_i W_i V = 0 \tag{2.41}$$

$$\dot{m}\sum_{i=1}^{NS}(Y_i h_i - Y_i^\circ h_i^\circ) + \dot{Q} = 0 \tag{2.42}$$

where, besides quantities already known, V is the reactor volume, $\dot{\omega}_i$ is the molar rate of production by chemical reaction of species i per unit volume, W_i is the molecular weight of species i, h_i are the specific enthalpies, and $\dot{Q}$ is the reactor heat loss flux.

In the EDC model the PSR exchange mass (and in the most general version also energy) and energy with the so called *surrounding fluid*. Therefore in Eqs. (2.41) and (2.42) the exponent "o" stays for surrounding fluid. Composition and temperature of the gas exiting the reactor, that are, in fact, composition and temperature of fine structures, can then be found by solving these two equations.

The PSR equations are solved at steady state using a solution algorithm for the transient problem:

$$\frac{dY_i}{dt} = -\frac{1}{\tau}(Y_i - Y_i^\circ) + \frac{\dot{\omega}_i W_i}{\rho} \tag{2.43}$$

$$\frac{dh_i}{dt} = -\frac{1}{\tau}\sum_{i=1}^{NS}(Y_i h_i - Y_i^\circ h_i^\circ) - \frac{\dot{Q}}{\rho V} \tag{2.44}$$

where τ is a fluid-dynamic residence time. Magnussen in the EDC model assumed this time equal to the fluid-dynamic residence time in the fine structures:

$$\tau = \tau^* = \frac{1}{\dot{m}^*} \tag{2.45}$$

The rates of production $\dot{\omega}_i$ in Eq. (2.43) are set up on the basis of the thermochemical scheme used. Different degree of sophistication can be assumed: fast chemistry, reduced reaction mechanisms, and detailed chemical reactions schemes. The fast chemistry assumption leads to a one step reaction that from reactants gives products. This is the simplest and only the source term for fuel (F) as to be set up and the PSR solution is obvious. When reduced or detailed mechanisms are used the source terms are built on the basis of the contribution of each reaction involved and the number of equations to solve depends on the number of species involved. Therefore, when detailed mechanisms are complex, i.e. involve very many chemical species and many reactions, it is clear what advantage can come by using reduced reactions mechanisms.

EDC+PSR source terms

Therefore, burning fine structures have been modeled as Perfect Stirred Reactors. A further assumption is used: adiabaticity of these PSR, i.e., they exchange matter, but no energy, with the surrounding fluid. The modeling equations for such a reactors read [6]:

$$\dot{m}^* \left(Y_i^* - Y_i^0 \right) = \frac{\dot{\omega}_i^* W_i}{\rho^*} \qquad i = 1, ..., NS \tag{2.46}$$

and for enthalpy:

$$h^* = h^0 \tag{2.47}$$

To obtain these equations in terms of starred and mean quantities, we use Eqs. (2.27) in to Eqs. (2.46):

$$\frac{\dot{m}^*}{1 - \chi\gamma^*} \left(Y_i^* - \tilde{Y}_i \right) = \frac{\dot{\omega}_i^* W_i}{\rho^*} \qquad i = 1, ..., NS \tag{2.48}$$

For enthalpy it is simply:

$$\tilde{h} = h^* \quad . \tag{2.49}$$

Therefore the chemical species reaction rates for the fine structures can be written as:

$$\dot{w}_i^* \equiv \frac{\dot{\omega}_i^* W_i}{\rho^*} = \frac{\dot{m}^*}{1 - \chi\gamma^*} \left(Y_i^* - \tilde{Y}_i \right) \qquad i = 1, ..., NS \tag{2.50}$$

If only the fine structure contribution is considered (no contribution from surrounding fluid) the mean reaction rates read:

$$\tilde{\dot{w}}_i = \gamma^* \chi \dot{w}_i^* \qquad i = 1, ..., NS \tag{2.51}$$

Then, using Eq. (2.50), the source terms for the chemical species transport equations:

$$\nabla \cdot (\bar{\rho}\, \tilde{U}\, \tilde{Y}_i) + \nabla \cdot (\bar{\rho}\, \widetilde{U'' Y_i''}) = \nabla \cdot (\bar{\rho}\, \mathcal{D}\, \nabla \tilde{Y}_i) + \bar{\rho}\, \widetilde{\dot{w}_i} \qquad i = 1, ..., NS \tag{2.52}$$

can be written as:

$$\tilde{w}_i = \frac{\dot{m}^* \gamma^* \chi}{1 - \chi \gamma^*} \left(Y_i^* - \tilde{Y}_i \right) \qquad i = 1, ..., NS \tag{2.53}$$

Numerical experiments performed by Magnussen for premixed flames showed that this reaction rates were too low [1]. Therefore a corrective parameter η was introduced, yielding to the final expression for the chemical species source terms:

$$\tilde{w}_i = \frac{\dot{m}^* \gamma^* \chi \eta}{1 - \gamma^* \chi} \left(Y_i^* - \tilde{Y}_i \right) \qquad i = 1, ..., NS \tag{2.54}$$

In these expressions η is:

$$\eta = \begin{cases} \frac{1}{\gamma} & \text{if } \frac{1}{\gamma} \leq \eta_{lim} \\ \eta_{lim} & \text{if } \frac{1}{\gamma} > \eta_{lim} \end{cases} \tag{2.55}$$

and

$$\eta_{lim} = 1 + \frac{\tilde{Y}_{pr}}{\tilde{Y}_{min}(1 + r_{fu})} \tag{2.56}$$

Besides, it is:

$$\tilde{Y}_{pr} = \tilde{Y}_{H_2O} + \tilde{Y}_{CO_2} \tag{2.57}$$

and [13]:

$$\tilde{Y}_{min} = \begin{cases} \tilde{Y}_{fu} & \text{if } \tilde{Y}_{fu} \leq (Y_{fu})_{st} \\ \tilde{Y}_{ox}/r_{fu} & \text{if } \tilde{Y}_{fu} > (Y_{fu})_{st} \end{cases} \tag{2.58}$$

where $\tilde{Y}_{fu}$ comes from Eq. (2.39).

2.8 Numerical method

2.8.1 Introduction

The numerical solution of the Navier-Stokes equations is performed by `GTTURBO_EDC` via a finite volumes method. The solution domain is divided with a structured grid of finite volumes; the conservation equations for total mass, momentum, energy and other relevant quantities such as turbulent kinetic energy and its dissipation rate are integrated over the generic finite volume and set in linearized form. When the Mach number is low ($M \leq 0.1$), the conventional compressible formulation—where density is numerically obtained from the equation of mass conservation and pressure from the equation of state—does not work. Here, the approach based on the solution of a Poisson-type equation for pressure is instead adopted and density is calculated from the equation of state. A semi-implicit algorithm is used for the iterative solution of the discretized steady Navier-Stokes equations.

2.8.2 Finite volume discretization

The numerical solution of the Navier-Stokes equations is based here on the finite volume method. The solution domain is decomposed with a structured grid of finite volumes as shown in Fig. 2.3; the discretized transport equation for a generic quantity ϕ can be obtained by integrating its continuous equation on the generic finite volume V_P[2]

$$\int_{V_P}\left[\frac{\partial(\rho\,\phi)}{\partial t}+\frac{\partial(\rho\,u\,\phi)}{\partial x}+\frac{1}{r}\,\frac{\partial(r\,\rho\,v\,\phi)}{\partial r}\right]\,dV=\int_{V_P}\left[\frac{\partial}{\partial x}\left(\Gamma\frac{\partial\phi}{\partial x}\right)+\frac{1}{r}\,\frac{\partial}{\partial r}\left(r\,\Gamma\,\frac{\partial\phi}{\partial r}\right)+w\right]\,dV \quad (2.59)$$

where w is the source/sink term for ϕ.

The measure of one finite volume is given by (see figure 2.3) $V_P = r_m\,\Delta r\,\Delta x$, where:

$$r_m = \frac{1}{2}(r_n + r_s) \quad (2.60)$$

$$\Delta r = r_n - r_s \quad (2.61)$$

$$\Delta x = x_e - x_w \quad (2.62)$$

Applying the Gauss theorem[3] to (2.59), the differential terms can be transformed in flux integrals over the four finite volume faces:

$$\int_{V_P}\frac{\partial(\rho\,\phi)}{\partial t}\,dV+\int_{S_e}\left(\rho\,u\,\phi-\Gamma\,\frac{\partial\phi}{\partial x}\right)\,r\,dr-\int_{S_w}\left(\rho\,u\,\phi-\Gamma\,\frac{\partial\phi}{\partial x}\right)\,r\,dr+$$
$$\int_{S_n}\left(r\,\rho\,v\,\phi-r\,\Gamma\,\frac{\partial\phi}{\partial r}\right)\,dx-\int_{S_s}\left(r\,\rho\,v\,\phi-r\,\Gamma\,\frac{\partial\phi}{\partial r}\right)\,dx=\int_{V_P}w\,dV \quad (2.64)$$

The volume and surface integrals in this equation are approximated with the values of the variables in the volume and surface centers, times the volume V_P and surface S_α, $\alpha = E, W, N, S$; therefore, the approximation for equation (2.64) is:

$$\frac{\partial(\rho_P\,\phi_P)}{\partial t}V_P+\left[\left(\rho\,u\,\phi-\Gamma\,\frac{\partial\phi}{\partial x}\right)\,S\right]_w^e+\left[\left(\rho\,v\,\phi-\Gamma\,\frac{\partial\phi}{\partial r}\right)\,S\right]_s^n=w_P\,V_P \quad (2.65)$$

---

[2] The equation is written here for $2D$ planar or axisymmetric flows without swirl, i.e. $w = 0$. In the planar case the finite volume has a depth of 1 m, in the axisymmetric case of 1 rad. In the planar case it has to be assumed $r = 1$, $\partial r = \partial y$.

[3] Given a vector field $\mathbf{u}$, the Gauss theorem states:

$$\int_V \nabla\cdot\mathbf{u}\,dV=\int_S \mathbf{u}\cdot\mathbf{n}\,dS \quad (2.63)$$

where V is a geometric volume and S the surface surrounding it; $\mathbf{n}$ is the normal to the surface directed from the inside to the outside.

where the east and west surfaces are given by $S_e = S_w = r_m \, \Delta r$, the north surface is given by $S_n = r_n \, \Delta x$ and the south one by $S_s = r_s \, \Delta x$.

The values of variables on the cell faces have to be expressed as function of the values in the adjacent nodes. The first order derivatives related to gradient diffusion are approximated assuming a linear distribution between cell nodes (see figure 2.4 where the $1D$ case is reported); for example at the east boundary this approximation yields:

$$\left.\frac{\partial \phi}{\partial x}\right|_e \simeq \frac{\phi_E - \phi_P}{x_E - x_P} \tag{2.66}$$

This approximation corresponds to second order central differencing for the term $\partial^2\phi/\partial x^2$ in node P; in fact, it can be shown (via a Taylor series expansion with initial point P) that on uniform meshes the accuracy of the discretization is proportional to Δx^2, i.e.:

$$\frac{1}{x_e - x_w}\left[\frac{\phi_E - \phi_P}{x_E - x_P} - \frac{\phi_P - \phi_W}{x_P - x_W}\right] = \left.\frac{\partial^2 \phi}{\partial x^2}\right|_P + O[\Delta x^2] \tag{2.67}$$

The approximation of convective terms using a linear distribution on cell boundaries (central differencing) can give the well-known problem of wiggles oscillations for convection dominated flows. In order to avoid this problem an approximation of the convective terms based on the values of ϕ in the upwind nodes (upwinding) is commonly employed; the effect of upwinding is to locally introduce some *numerical diffusion* which has a dumping effect on the wiggles generated by central differencing.

Two different upwind schemes are actually implemented in GTTURBO:

- *Hybrid central-upwind scheme.* A central approximation is used when the face Peclet number[4] is less than 2, while a full upwinding (first order accuracy) when $Pe \geq 2$. Therefore (east boundary):

$$(\rho \, u \, \phi)_e \simeq (\rho \, u)_e \frac{\phi_E + \phi_P}{2}, \qquad \text{if:} \quad Pe_e < 2 \tag{2.69}$$

$$(\rho \, u \, \phi)_e \simeq \frac{(\rho \, u)_e + (\rho \, |u|)_e}{2} \phi_P + \frac{(\rho \, u)_e - (\rho \, |u|)_e}{2} \phi_E, \qquad \text{if:} \quad Pe_e \geq 2 \tag{2.70}$$

  Relation (2.70) can be written as the central difference approximation of the sum between a convection and a numerical diffusion terms:

$$(\rho \, u \, \phi)_e \simeq (\rho \, u)_e \frac{\phi_P + \phi_E}{2} - \underbrace{\frac{(\rho \, u)_e}{2}(x_E - x_P)}_{\Gamma_e^{num}} \frac{\phi_E - \phi_P}{x_E - x_P}, \qquad \text{if:} \quad Pe_e \geq 2 \tag{2.71}$$

---

[4] The Peclet number is given (for example at the east boundary) by:

$$Pe_e = \frac{(\rho \, |u|)_e \, (x_E - x_P)}{\Gamma_e} \tag{2.68}$$

It is simple to verify from this relation that the effect of first order upwinding is to lower the effective face Peclet number to $Pe = 2$, reducing the convective dominance of the discretized equations; therefore, a large numerical diffusion is introduced by the hybrid central-upwind scheme for the case of convection dominated flows and this can negatively influence the results accuracy.

Note that when $Pe \geq 2$ the effect of physical diffusion is neglected in order to guarantee continuity between the central and upwind discretizations.

- *Hybrid central-TVD (Total Variation Diminishing) scheme.* This scheme is globally second order accurate. It is very similar to the previous scheme; when $Pe < 2$ the central approximation (2.69) is used, when $Pe \geq 2$ an upwind approximation of the type (2.71) is used but the numerical diffusion coefficient $\Gamma_{num} = (\rho\, u)_e / 2 (x_E - x_P)$ is decreased by a limiting function ψ (Van Leer limiter):

$$\begin{aligned}
(\rho\, u\, \phi)_e &\simeq (\rho\, u)_e \frac{\phi_P + \phi_E}{2} - \frac{(\rho\, u)_e}{2} (x_E - x_P)(1 - \psi_e) \frac{\phi_E - \phi_P}{x_E - x_P} && (2.72)\\
\psi_e &= \frac{r_e + |r_e|}{1 + r_e} && (2.73)\\
r_e &= \frac{\phi_P - \phi_W}{\phi_E - \phi_P}, \qquad \text{if:} \quad u_e > 0 && (2.74)\\
r_e &= \frac{\phi_E - \phi_{EE}}{\phi_P - \phi_E}, \qquad \text{if:} \quad u_e < 0 && (2.75)
\end{aligned}$$

In all cases, the discretized transport equation (2.65) for ϕ can be set as:

$$\begin{aligned}
\frac{\partial(\rho_P\, \phi_P)}{\partial t} V_P \quad + & \\
& \left[(\rho\, u)_e \frac{\phi_P + \phi_E}{2} - \Gamma^\star_e \frac{\phi_E - \phi_P}{x_E - x_P} \right] S_e - \\
& \left[(\rho\, u)_w \frac{\phi_P + \phi_W}{2} - \Gamma^\star_w \frac{\phi_P - \phi_W}{x_P - x_W} \right] S_w + \\
& \left[(\rho\, v)_n \frac{\phi_P + \phi_N}{2} - \Gamma^\star_n \frac{\phi_N - \phi_P}{r_N - r_P} \right] S_n - \\
& \left[(\rho\, v)_s \frac{\phi_P + \phi_S}{2} - \Gamma^\star_s \frac{\phi_P - \phi_S}{r_P - r_S} \right] S_s - w_P\, V_P = 0 \qquad (2.76)
\end{aligned}$$

where the diffusion coefficients have to be expressed as given by (2.69)- (2.75) according to the faces Peclet number and the discretization scheme used.

Subtracting to the right hand side of equation (2.76) the mass residual term:

$$\phi_P \left[(\rho\, u)_e A_e - (\rho\, u)_w A_w + (\rho\, v)_n A_n - (\rho\, v)_s A_s \right] \qquad (2.77)$$

which is zero for stationary flows due to the mass conservation equation (2.1), the following linear form is obtained[5]:

$$A_P\,\phi_P = A_E\,\phi_E + A_W\,\phi_W + A_N\,\phi_N + A_S\,\phi_S + Q_P \tag{2.78}$$

where:

$$\begin{aligned}
A_E &= \left[-\frac{(\rho\,u)_e}{2} + \frac{\Gamma^\star_e}{x_E - x_P}\right] S_e && (2.79)\\
A_W &= \left[\frac{(\rho\,u)_w}{2} - \frac{\Gamma^\star_w}{x_P - x_W}\right] S_w && (2.80)\\
A_N &= \left[-\frac{(\rho\,u)_n}{2} + \frac{\Gamma^\star_n}{x_N - x_P}\right] S_n && (2.81)\\
A_S &= \left[\frac{(\rho\,u)_s}{2} - \frac{\Gamma^\star_s}{x_P - x_S}\right] S_s && (2.82)\\
A_P &= A_E + A_W + A_S + A_N && (2.83)\\
Q_P &= w_P\,V_P && (2.84)
\end{aligned}$$

2.8.3 Numerical solution of transport equations

The numerical solution of the discretized transport equations is performed via an iterative semi-implicit algorithm where the equations are solved sequentially and implicitly. In order to advance the solution by one time step, each transport equation is written as:

$$A_P\,\phi_P^{(n+1)} = A_E\,\phi_E^{(n+1)} + A_W\,\phi_W^{(n+1)} + A_N\,\phi_N^{(n+1)} + A_S\,\phi_S^{(n+1)} + Q_P^{(n)} \tag{2.85}$$

where the coefficients A_P, A_α are calculated with the last available values of the dependent variables according to relations (2.79)-(2.84). This system is characterized by a pentadiagonal matrix and it is solved in GTTURBO iteratively via a tridiagonal matrix algorithm (TDMA) [2].

It has been said in the introduction that—at low Mach number—the classical compressible formulation where density is calculated from the mass conservation equation and pressure from the equation of state does not work; this is due to the large difference existing between the propagation velocities of pressure and convective waves. The integration time step is in fact related to the fast pressure waves; during the time that a pressure wave cross a finite volume cell, the convective waves travel only for a little fraction of the cell characteristic length, slowing down the convergence rate of the iterative numerical solution algorithm.

---

[5] In this work only steady flows ($\partial\phi/\partial t \equiv 0$) will be taken in consideration; therefore the terms of the type $\partial\phi/\partial t$ have been neglected in the discretized equations.

In this work the equation of state is used to calculate density at a fixed pressure (which is the average pressure p_{av} in the flow domain), assuming negligible the effect of the small pressure variations ($\Delta p / p_{av} \simeq M^2$); therefore, in the case of non-reacting flows, the enthalpy conservation equation and the equation of state become redundant[6]. The pressure variations—which determinates momentum variations—are calculated from a Poisson-type equation obtained from the combination of momentum and total mass conservation ($\nabla \cdot (\rho \mathbf{u}) = 0$). In this case the limitation on the time step imposed by the pressure waves is removed because their speed is infinite (incompressible flows). The algorithm used in this work to calculate the pressure fluctuations is called SIMPLE (Semi-Implicit Method for Pressure Linked Equations) [2] and it can be summarized as follows:

- The conservation equations for u and v are solved at an intermediate step $n + 1/2$ with the pressure fixed at time n:

$$A_P^{(u)}\, u_P^{(n+1/2)} = \sum_{\alpha=E,W,N,S} A_\alpha^{(u)}\, u_\alpha^{(n+1/2)} - 0.5\,(p_E^{(n)} - p_W^{(n)})\, S_{ew} + Q_u^{(n)} \tag{2.86}$$

$$A_P^{(v)}\, v_P^{(n+1/2)} = \sum_{\alpha} A_\alpha^{(v)}\, v_\alpha^{(n+1/2)} - 0.5\,(p_N^{(n)} - p_S^{(n)})\, S_{ns} + Q_v^{(n)} \tag{2.87}$$

  where $S_{ew} = S_e = S_w$ e $S_{ns} = 0.5\,(S_n + S_s)$. Note that a central difference approximation has been used for the components of the pressure gradient.

- Then, the same equations are written at iteration step $n + 1$ with pressure considered also at $n + 1$:

$$A_P^{(u)}\, u_P^{(n+1)} = \sum_{\alpha=E,W,N,S} A_\alpha^{(u)}\, u_\alpha^{(n+1)} - 0.5\,(p_E^{(n+1)} - p_W^{(n+1)})\, S_{ew} + Q_u^{(n)} \tag{2.88}$$

$$A_P^{(v)}\, v_P^{(n+1)} = \sum_{\alpha} A_\alpha^{(v)}\, v_\alpha^{(n+1)} - 0.5\,(p_N^{(n+1)} - p_S^{(n+1)})\, S_{ns} + Q_v^{(n)} \tag{2.89}$$

  subtracting to these equations at iteration step $n + 1$, the equations (2.86) and (2.87) at the intermediate iteration step, yields:

$$A_P^{(u)}\,(u_P^{(n+1)} - u_P^{(n+1/2)}) = \sum_{\alpha} A_\alpha^{(u)}\,(u_\alpha^{(n+1)} - u_\alpha^{(n+1/2)}) - \frac{1}{2}\,(\delta p_E^{(n+1)} - \delta p_W^{(n+1)})\, S_{ew} \tag{2.90}$$

$$A_P^{(v)}\,(v_P^{(n+1)} - v_P^{(n+1/2)}) = \sum_{\alpha} A_\alpha^{(v)}\,(v_\alpha^{(n+1)} - v_\alpha^{(n+1/2)}) - \frac{1}{2}\,(\delta p_N^{(n+1)} - \delta p_S^{(n+1)})\, S_{ns} \tag{2.91}$$

  where $\delta p^{(n+1)} = p^{(n+1)} - p^{(n)}$. In the SIMPLE method the terms relative at nodes E, W, N, S are assumed zero (this doesn't introduce an error because

---

[6] At low Mach number the dissipation function Φ and the pressure term Dp/Dt in the enthalpy conservation equation are negligible. The equation becomes a convection diffusion equation for enthalpy; given a uniform inlet profile for h (for example, pure air with uniform temperature) and adiabatic boundary conditions, it will be $h = h_{inlet} = cost$ all over the flowfield. This explains the redundancy of the enthalpy conservation equation.

these terms are really zero at convergence of the iteration process). Therefore, the velocity components at time $n+1$ are given by the simple explicit formulas:

$$u_P^{(n+1)} = u_P^{(n+1/2)} - \underbrace{0.5\, S_{ew}/A_P^{(u)}}_{-D_P^{(u)}} (\delta p_E^{(n+1)} - \delta p_W^{(n+1)}) \tag{2.92}$$

$$v_P^{(n+1)} = v_P^{(n+1/2)} - \underbrace{0.5\, S_{ns}/A_P^{(v)}}_{-D_P^{(v)}} (\delta p_N^{(n+1)} - \delta p_S^{(n+1)}) \tag{2.93}$$

- Relations (2.92) and (2.93) are substituted in the mass conservation equation (2.1) written for steady flows and integrated over the finite volume yields:

$$\rho_e\, u_e\, S_e - \rho_w\, u_w\, S_w + \rho_n\, v_n\, S_n - \rho_s\, v_s\, S_s = 0 \tag{2.94}$$

and permits to obtain a transport equation for the pressure correction $\delta p^{(n+1)}$. In equation (2.94) the velocity components are needed on the cell faces, while in equations (2.92) and (2.93) are given at cell nodes. The most natural way to calculate velocities at cell faces is according to a linear interpolation of the values in the two neighbour nodes; it will be shown in the next paragraph that this approximation leads to strong unphysical oscillations in the solution of flows with a non-linear pressure distribution (pressure-velocity decoupling) [2]. In order to avoid this oscillations, equations (2.92) and (2.93) are written directly in terms of velocity components on the cell faces (for example at the east and north cell faces):

$$u_e^{(n+1)} = u_e^{(n+1/2)} + D_e^{(u)}\, (\delta p_E^{(n+1)} - \delta p_P^{(n+1)}) \tag{2.95}$$

$$v_n^{(n+1)} = v_n^{(n+1/2)} + D_n^{(v)}\, (\delta p_N^{(n+1)} - \delta p_P^{(n+1)}) \tag{2.96}$$

with $D_e^{(u)} = 0.5\,(D_P^{(u)} + D_E^{(u)})$ and $D_n^{(v)} = 0.5\,(D_P^{(v)} + D_N^{(v)})$. Details about the way to calculate $u_e^{(n+1/2)}$ and $v_n^{(n+1/2)}$ will be given in the next paragraph.

Replacing relations (2.95) and (2.96) in (2.94), the following Poisson-type equation for the pressure correction is obtained:

$$\begin{gathered}\rho_e\, S_e\, D_e^{(u)}\, (\delta p_E^{(n+1)} - \delta p_P^{(n+1)}) - \rho_w\, S_w\, D_w^{(u)}\, (\delta p_P^{(n+1)} - \delta p_W^{(n+1)}) + \\ \rho_n\, S_n\, D_n^{(v)}\, (\delta p_N^{(n+1)} - \delta p_P^{(n+1)}) - \rho_s\, S_s\, D_s^{(v)}\, (\delta p_P^{(n+1)} - \delta p_S^{(n+1)}) = -m_P^{n+1/2}\end{gathered} \tag{2.97}$$

where $m_P^{(n+1/2)}$ represents the mass residual calculated with the velocity components on cell faces at time $n+1/2$:

$$m_P^{(n+1/2)} = \rho_e\, u_e^{(n+1/2)}\, S_e - \rho_w\, u_w^{(n+1/2)}\, S_w + \rho_n\, v_n^{(n+1/2)}\, S_n - \rho_s\, v_s^{(n+1/2)}\, S_s \tag{2.98}$$

Also equation (2.97) can be set in the form (2.78):

$$A_P\, \delta p_P^{(n+1)} = \sum_\alpha A_\alpha\, \delta p_\alpha^{(n+1)} - m_P^{n+1/2} \tag{2.99}$$

and solved via the TDMA algorithm.

In order to improve the convergence performance of the iterative solution algorithm described here, the equations for the momentum components are relaxed as (in the following equation ϕ representing u or v):

$$A_P\, \phi_P^{(n+1)} = r_\phi \left[\sum_\alpha A_\alpha\, \phi_\alpha^{(n+1)} + Q_P^{(n)} \right] + (1 - r_\phi)\, A_P\, \phi_P^{(n)} \tag{2.100}$$

where r_ϕ is a relaxation parameter ($r_\phi \in (0, 1]$); values of $r_\phi = 0.5$ are typically used. The velocity components at the iteration step $n+1$ are calculated with the relations (2.95) and (2.96) using the entire pressure correction obtained from equation (2.99). Sometimes, for better convergence, it can be useful to calculate pressure at $n+1$ limiting the pressure correction as:

$$p^{(n+1)} = p^{(n)} + r_p\, \delta p^{(n+1)} \tag{2.101}$$

with $r_p \in (0, 1]$.

2.8.4 Boundary conditions

In this paragraph the boundary conditions used for each variable will be described.

Boundary conditions for all variables except pressure

Inlets. A full upwind approximation (figure 2.4) is used in GTTURBO at the inlets for all the variables.

Walls. The flow is assumed parallel to the rigid boundary. Considering for example the south boundary, this means that $\partial v/\partial y|_{wall} = 0$ and u_{wall}, $v_{wall} = 0$. These conditions can be simply imposed by setting $A_S^{(v)} = 0$ in the v transport equation for the cell adjacent to the boundary; the same condition has to be imposed for any scalar variable with zero net flux at the wall (adiabatic or non-catalytic boundary conditions).

Symmetry (only axisymmetric case). On the symmetry axis (considered for example at the south boundary) the conditions to impose are $v_{axis} = 0$ and $\partial\phi/\partial r|_{axis} = 0$ for all variables; the last of these can be imposed assuming $A_S^{(\phi)} = 0$.

Exit section. The condition at the exit section (considered for example at the east boundary) is based on the hypothesis of completely developed profile for each variable; it is therefore given by $\partial\phi/\partial x|_{exit} = 0$. This condition can be imposed simply setting $A_E^{(\phi)} = 0$ for the cell adjacent to the exit.

Boundary conditions for the pressure correction equation.

The boundary conditions for the pressure correction equation (2.99) are given by zero flux on all types of boundaries. This conditions are imposed setting equal to zero the coefficients $D^{(u)}$ and $D^{(v)}$ for the boundary cell faces.

According to relations (2.95) and (2.96), this means that the velocity all over the boundaries doesn't feel the effect of δp corrections (velocity is fixed at the boundaries). With these conditions, if the mass residual $m_P^{(n+1/2)}$ is different from zero (and generally it is because the momentum equations don't ensure mass conservation), the pressure correction equation doesn't have a solution; this problem is the same of heat conduction in a solid body with adiabatic surface and a heat source inside. In order to have a solution every iteration step, the velocity on the exit boundary (assumed at the east side) is modified as:

$$u_{e,mod}^{(n+1/2)} = u_P^{(n+1/2)} + u_c \tag{2.102}$$

where the correction u_c is given by:

$$u_c = \frac{\text{flowin} - \text{flowout}}{S_{exit}} \tag{2.103}$$

In this expression $flowin$ and $flowout$ are the volumetric fluxes respectively entering and exiting the flow domain; S_{exit} is the surface of the exit section. Note that $flowout$ is calculated with the value of velocity on the exit boundary before modification at the intermediate time $n + 1/2$ ($u_e^{(n+1/2)}$).

The modified total mass residual $m_{tot,mod}^{(n+1/2)}$ in the flow domain is given by the sum of the cell mass residual $m_P^{(n+1/2)}$ over all cells; due to the conservative nature of the finite volume method, this quantity is equal to the difference between the flow rate exiting and the one entering the flow domain:

$$m_{tot,mod}^{(n+1/2)} = \int_{A_{exit}} u_{e,mod}^{(n+1/2)} \, dA - \text{flowin} \tag{2.104}$$

replacing relation (2.102) in (2.104) yields:

$$m_{tot,mod}^{(n+1/2)} = \int_{A_{exit}} u_P^{(n+1/2)} \, dA - \text{flowout} + \text{flowin} - \text{flowin} \tag{2.105}$$

Due to the exit section boundary condition of full developed profile, i.e. $u_e^{n+1/2} = u_P^{n+1/2}$, relation (2.105) can be written as:

$$m_{tot,mod}^{(n+1/2)} = \int_{A_{exit}} u_e^{n+1/2}\, dA - \text{ flowout} = \text{ flowout} - \text{ flowout} = 0 \tag{2.106}$$

with correction (2.102) on the exit boundary, the total mass residual becomes zero and therefore the Poisson equation for the pressure correction δp admits a solution.

2.8.5 Non-staggered grid feature.

When the velocities components and pressure are located in the same nodes as in figure 2.3, the problem of pressure-velocity decoupling arises. To understand this problem reference [2] should be consulted; here, only a little explanation will be given.

In the case of pressure and velocity components located in the same nodes, a 2-Δx (or 2-Δy) central difference approximation has necessarily to be used for the pressure gradient components in the momentum conservation equations (2.86) and (2.87); with this approximation any variation of pressure in node P is not felt by the local values u_P and v_P of the velocity components, i.e. there is local pressure-velocity decoupling; in the case of non-linear variations of pressure, this decoupling generates strong unphysical oscillations in the solution. An example of such oscillations is shown in figures 2.5 a) where the pressure field contours are reported for the case of a turbulent flow in a axisymmetric combustion chamber that will be considered in a next paragraph. Strong pressure wiggles arise in the flowfield.

In order to avoid pressure-velocity decoupling, for many years the so-called staggered grid arrangement [2] has been used; with this grid arrangement, the velocity components are located on the cell faces as reported in figure 2.6. The components of the pressure gradient in the momentum conservation equations can be calculated in this case as:

$$\left.\frac{\partial p}{\partial x}\right|_w \simeq \frac{p_P - p_W}{x_P - x_W} \tag{2.107}$$

This is a central discretization based on 1-Δx (or 1-Δy) variation of pressure which avoids the pressure-velocity decoupling. The main problem of staggered grids is related with the setting of boundary conditions because three kinds of control volumes are involved: for u, v and all remaining scalars.

In order to maintain a non-staggered grid arrangement, Rhie and Chow [14] developed a novel procedure for the approximation of velocities components on cell boundaries. According to this procedure, the velocity components are calculated in the nodes with equations (2.86) and (2.87) using the 2-Δx (or 2-Δy) central approximation for the pressure derivatives but their values on the cell faces which are needed to calculate the fluxes of all the variables are calculated as follows (for example east boundary):

$$u_e = \frac{u_P + u_E}{2} - D_P^{(u)} \frac{-(p_E - p_W)}{x_E - x_W} - D_E^{(u)} \frac{-(p_{EE} - p_P)}{x_{EE} - x_P} + 0.5 * (D_P^{(u)} + D_E^{(u)}) \frac{-(p_E - p_P)}{x_E - x_P} \quad (2.108)$$

according to this formula the velocities components on the cell faces are calculated as linear interpolation of the velocities components in the cell nodes purified from the 2-Δx pressure contribution plus a correction given by the 1-Δx pressure contribution at the cell- face. Figure 2.6 b) shows the pressure field for a turbulent combustor obtained with the Rhie-Chow procedure; it can be seen that the strong pressure oscillation of figure 2.6 a) have been eliminated.

2.9 CFD code structure

A schematic representation of the CFD code structure is reported in Fig. 2.7. The initialization procedure assigns values to fluidodynamic and chemical quantities. Usually the mixture in the chamber is assumed unburned therefore a fresh mixture composition is assigned everywhere. For special needs, pockets of burnt mixture can be assigned in the field (hot spots) which can be useful to light up the flame. From this assigned initial field, the code solves momentum components and $\kappa - \epsilon$ equations with a segregated procedure, i.e. each equation is solved singularly, sequentially and implicitly. Then the scalars equations are singularly solved. The number of these equations depends on the chemical kinetics mechanism implemented, in fact, a number of equations equal to the number of independent chemical species as to be accounted for. The source terms for these equations are set up with the EDC-PSR model. After this step, mean density, mean temperature and all the set of mean mass fractions are updated. At this point, performing the convergence tests the code decides if further iterations are needed or if the degree of accuracy requested has been obtained.

Pre-processing, i.e., grid generation, as been performed by using the GEMS software [15]. Data post-processing has been performed using Tecplot [16].

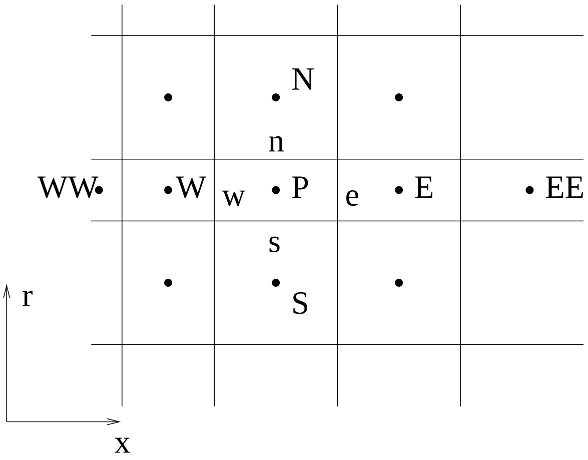

Figure 2.3: Finite volume grid.

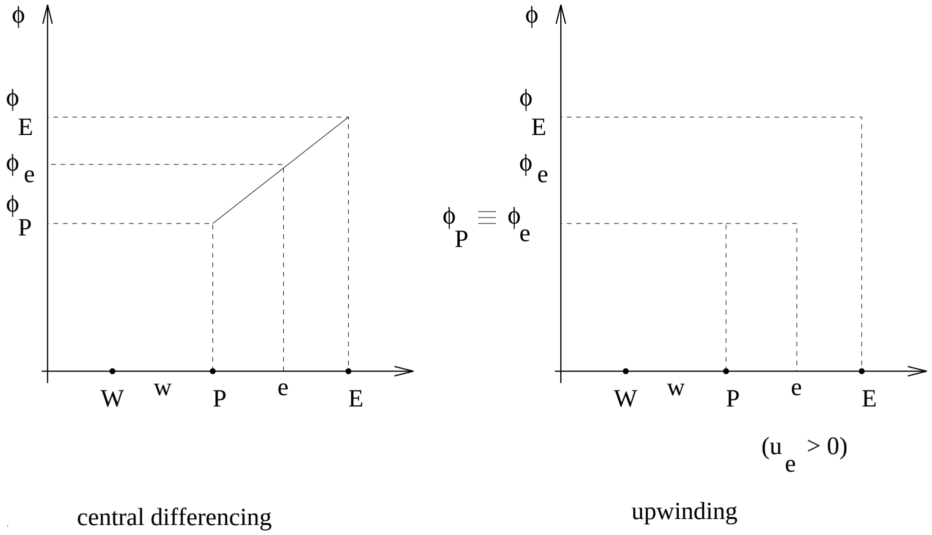

Figure 2.4: Central and upwind approximation of function ϕ on the east cell face.

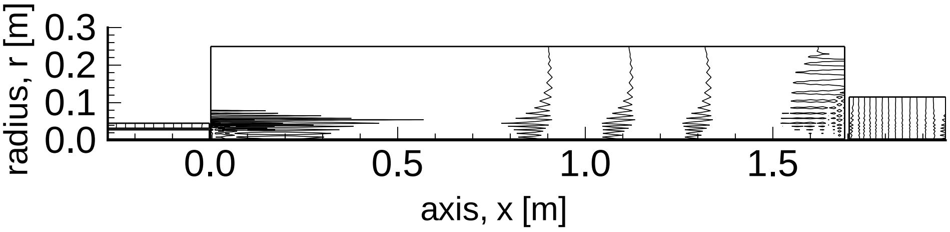

a) TURBULENT FLOW IN A COMBUSTOR.
Pressure field without Rhie-Chow
correction applyed.

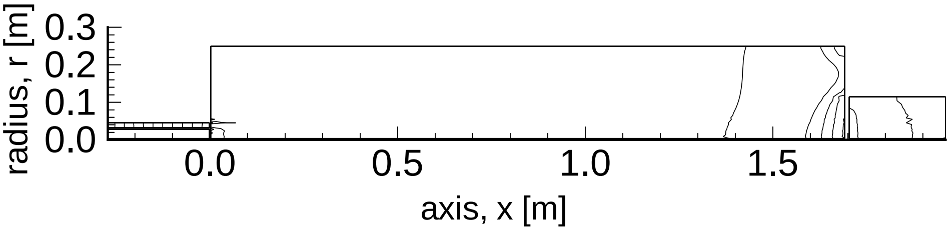

b) TURBULENT FLOW IN A COMBUSTOR.
Pressure field with the Rhie-Chow
correction applyed.

Figure 2.5: Effect of pressure-velocity decoupling when using non-staggered grids. From [3].

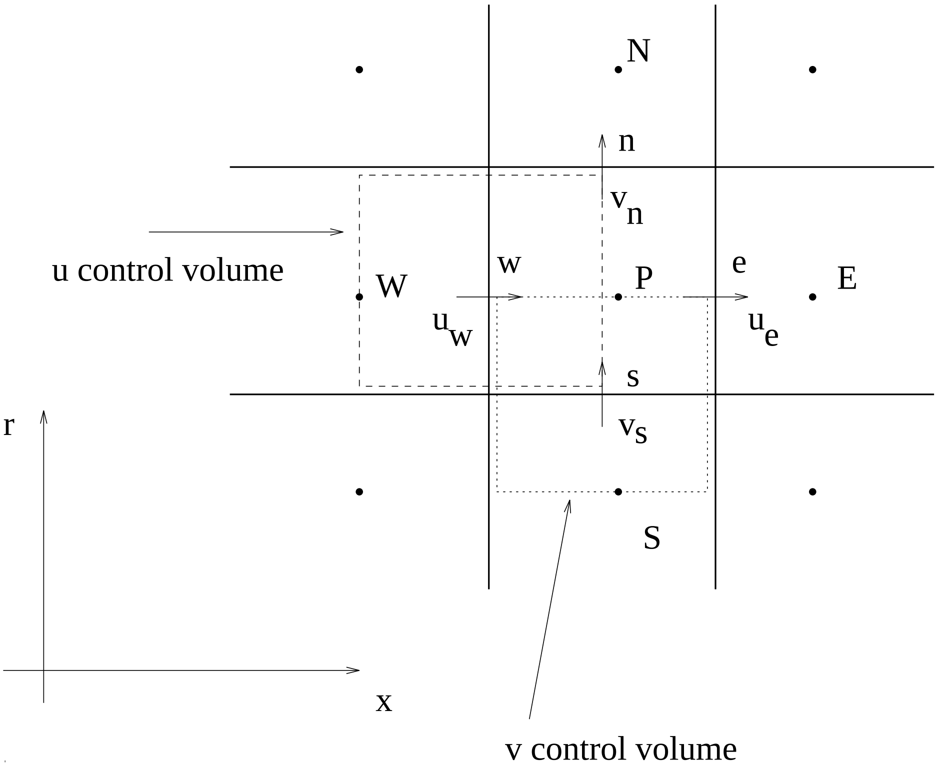

Figure 2.6: Staggered grid arrangement.

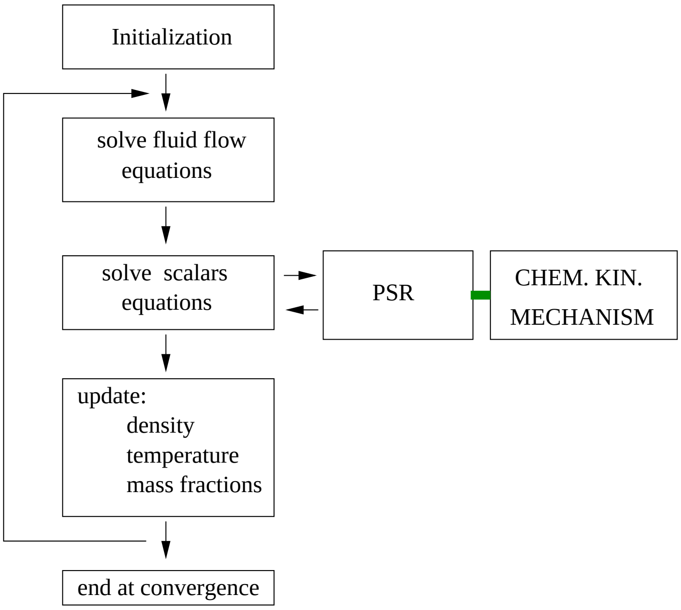

Figure 2.7: CFD code structure.

Chapter 3

Combustion Model Validation

3.1 Test case description

The test case considered in this chapter is a partially premixed turbulent combustion flow in a planar experimental combustor described in details in Refs. [17] and briefly presented in the following. The combustor is feed with two flows: the former is a homogeneous unburned mixture of CH_4 and air with equivalence fuel ratio $\phi = 0.8$, and the latter is a burned CH_4-air stoichiometric mixture ($\phi = 1$). A schematic of the experimental apparatus is shown in Fig. 3.1. Overall dimensions of the combustor are height .10 m (the combustor section is a square) and length 1.3 m. The two inlet flows are divided by a splitter plate: the burned gas inlet is .02 m high, the fresh mixture inlet .08 m high. The chamber walls are uncooled and equipped with probes to measure temperature and chemical species concentrations during the test. Each test lasts for 30 seconds [17].

3.2 Flow main features description

The burned gas entering from the lower inlet ignites the fresh mixture and stabilises the flame which then propagates along the combustor. The flow regime is turbulent and, for the range of velocities ($55 \div 200$ m/s) and turbulence intensity explored ($< 20\%$), no recirculations are expected.

It has been found that the velocity gradient between cold and hot flow favours the combustion efficiency [17]. An experiment with the two flows at the same velocity led to fresh mixture ignition but the flame developed more slowly. Therefore the pilot flow as been run at twice the velocity of the fresh mixture.

Turbulence has been found to affects much the flame behaviour, in fact experiments showed that increasing inlet turbulence yields to better combustion. Inlets

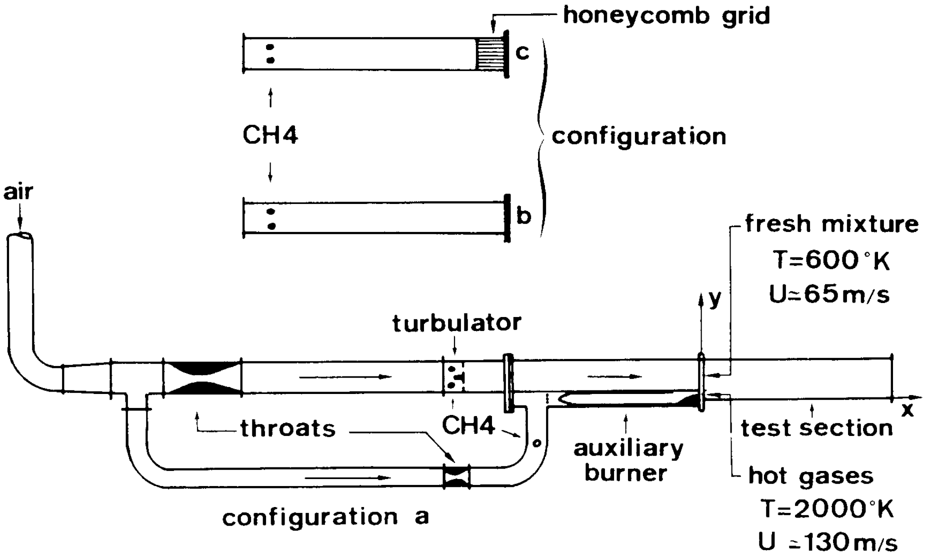

Figure 3.1: Moreau-Boutier experimental apparatus. Figure taken from Ref. [17].

levels of turbulence found for cold run increase of $1 \div 3\%$ when combustion occurs. This has been attributed to mechanical vibrations of the experimental apparatus. .

3.3 Numerical code

The numerical code used for the simulations of this test case is GTTURBO_EDC.

Combustion

The combustion model used is the Eddy Dissipation Concept by Magnussen [1] coupled with a Perfect Stirred Reactor solver taken from the CHEMKIN package [8].

Chemistry

This test case has been simulated by using the 6-steps reduced chemistry mechanism for CH_4-air combustion proposed by Chang and Chen [18] (see Section 6.3).

Modelling assumption

In this report the simulation has been performed assuming:

- two-dimensional flow;

Table 3.1: Test case characteristics

Flow regime	turbulent
Combustion regime	part.-premixed
Fuel	CH_4
Oxidiser	air
Pressure	1 atm
ϕ_u	0.8
ϕ_b	1.0
Geometry	plane
Unburned gas velocity (m/s)	65
Burnt gas velocity (m/s)	130
Unburned gas temp (K)	600
Burnt gas temp (K)	~ 2000

- adiabatic flow (negligible thermal exchange at combustor walls);
- non catalytic walls;
- radiation effects negligible.

3.4 Inlet and boundary conditions

Inlets conditions for the "base" test case have been set up taking the mean velocity and equivalence ratios suggested by the experimentalists (see Table 3.3). A level of turbulence of 10% has been assumed as first approximation. Uniform boundary conditions, i.e., flat profiles for all vectorial and scalar quantities, have been imposed. At combustor walls adiabaticity and no-slip conditions have been assumed. At the combustor exit a pressure outlet conditions has been imposed.

3.4.1 Grid and computational domain

In this case the computational domain coincides with the combustion chamber (see Fig. 3.2). After a grid independence test, a grid of 107 × 42 nodes has been chosen (Fig. 3.3).

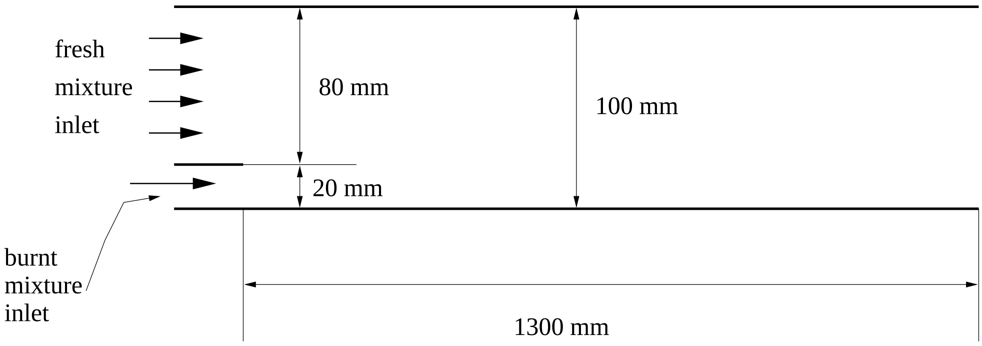

Figure 3.2: Schematic of the Moreau combustor.

3.5 Axial velocity profiles results

Figures 3.4 - 3.7 show comparisons between calculated (lines) and experimental (dots) mean velocities taken at different sections along the combustor.

A fair agreement has been found for the first two profiles (see Figs. 3.4 and 3.5) especially for the unburned part of the flow. A visible difference exists for the mean velocity in the lower part of the combustor. Figure 3.4 show also that the plug boundary conditions used at the inlets cannot follow the minimum of mean velocity coming from the matching of the two boundary layers after the splitter plate.

Moving downstream along the combustor the calculated velocities show a increasing disagreement with respect to experiments (see Figs.3.6 and 3.7). For the section at 650 mm from inlets, the peak mean velocity is 16 % lower than the experimental one whereas in the middle of the combustor the difference rises to 37 %.

To understand and explain these large differences, is better to have a look to the turbulent characteristics of the flow.

3.6 Turbulence intensity results

Figures 3.9 and 3.10 show turbulent intensity and velocity fluctuations profiles taken at several sections along the combustor. Experimental values of the same quantities taken from Ref. [17] are reported in Fig. 3.8. Comparisons of these data show that already at the section nearest to inlets the calculated levels of turbulent intensity are too low with respect to the measurements. In fact, looking at the profiles reported in Ref. [17] we see that unburned flow turbulence intensity is $\sim 13\%$ and burned flow turbulence intensity is $> 18\%$. In our results the peak of turbulence intensity due to the presence of the shear layer is correctly placed but the value is 40 % lower. The measurements downstream along the combustor, show that the peak of turbulence

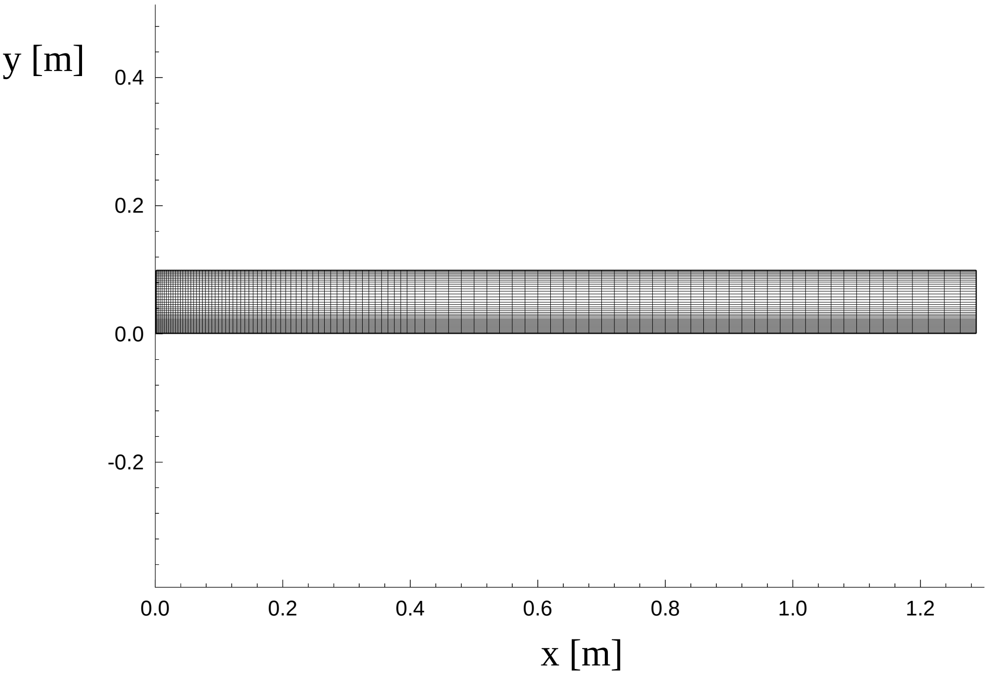

Figure 3.3: Computational Grid.

intensity is mainly due to the transverse velocity gradient located in correspondence of the zone of intense chemical reactions; its position rises following the rise of the flame front. This is not reproduced by the calculations where the maximum rises very slowly and remains located in the lower half of the combustor even for the farthest section (see Fig. 3.10).

3.7 Fuel concentration results

Figures 3.11 and 3.12 show the transverse profiles of CH_4 molar fractions scaled using N_2 molar fractions at 22 and 522 mm from inlet.

A fair agreement has been found at the first section even thought the calculation gives a too small CH_4 concentration just below the splitter plate showing a lower mixing whit respect to experiments. A very different scenario has been found on the farther section where experiments show much more fuel consumption in the higher part of the combustor. This, in agreement with what already said, shows that the simulation gives a less intense combustion due to the too small flame angle (i.e. too low turbulent flame velocity).

3.8 Results discussion

The large difference existing between the calculated results and the experimental data can be due to several factors. One is the correctness of boundary conditions imposed at inlets for the calculations. The difference between the turbulence levels has been already underlined in the previous Section. Another difference seems to exist for the burned gas axial mean velocity. Looking at Fig. 3.4 we see that already at 39 mm from inlet the experimental velocity is much lower than the calculated one. This let to think that a much more suitable value for the burned flow mean velocity should be $\sim 110 m/s$.

Furthermore, from the numerical results presented it is possible to conclude that the combustion model seems to give a poorer combustion which regard to the experiments. This can be seen looking at the velocity profiles at the farthest sections (see Figs. 3.6 and 3.7) and at the turbulence intensity profile which show the maxima located in the lower half part of the combustion section (see Fig. 3.9). In fact, assuming the turbulent rate be maximum in the combustion zone leads to a calculated flame front too flat (simulated turbulent flame velocity too small).

3.9 Effects due to inlet turbulence intensity

Results on turbulence intensity measured in the experiment and reported in Fig. 3.8 show two main characteristics: turbulence levels of the two inlet flows are different and both are higher than 10%. This lead to inquire the effect of changing inlet turbulent intensity on the combustion flow simulation. Inlet turbulence levels has been varied from 10 up to 20% for both cold and hot flows. Results are shown by Figs. 3.13 – 3.18.

Figure 3.13 shows a very little influence on the velocity profiles at the section nearer to the inlets (39 mm), the peak of velocity in the hot flow is unchanged as far as the unburned flow mean velocity. Small differences exist in the splitter plate wake.

Fig. 3.14 shows that a more sensitive effect can be found downstream in the combustor. The calculated profiles of mean velocity tend to became nearer to the experimental ones but, even for turbulence intensity of 20 %, the disagreement is still large.

From Fig. 3.17 we see that, changing the turbulent intensity at inlet, calculations give results which move towards experiments.

Figures 3.14 and 3.18 can be used to observe the effects of inlet turbulent intensity on combustion. The former shows as the combustion effectiveness rises whit inlet turbulent intensity but looking at the latter we can see a very small movement of the turbulent intensity maximum. This means that the flame front does not changes its angle very much, i.e. the turbulent flame velocity is almost the same in the three cases. To further inquire, $CH4$ profiles, obtained with different inlet turbulent intensity levels, are compared at the same combustor position, in Figure 3.19: even thought the increased turbulence level increases the CH_4 consumption, i.e. the combustion efficiency, the position of the flame in this section does not change very much and remains still far from the expected one.

3.10 Effects due to inlet mean velocity

Figure 3.20 shows a comparison between experiments and calculated mean velocity profiles obtained changing the inlet mean velocity value. The test case used is the one with inlet turbulent intensity set to 20%. The dashed line is the profile obtained using 110 m/s at inlet. It is evident how at 39 mm from inlet the difference underlined in one of the previous sections can be recovered with a lower inflow velocity for the burned gas. The same calculations are compared in Fig. 3.21 at 650 mm: the smaller inlet velocity for the burned gas lowers the peak of mean velocity in this section making the disagreement between experiments and calculations larger.

3.11 Conclusions

After examining the results presented the author concludes that the inflow velocity for the burnt gas should be assumed $\sim$ 110 m/s instead than 130 m/s. A suitable assumption for inlet turbulent intensity should be 13% for the unburned gas flow and 18% for the burnt gas flow. Starting from these new inlet conditions the computational results will produce more clear evidence about the effectiveness of the combustion model used. Therefore conclusions about combustion model tuning can be drawn once these boundary conditions modifications have been adopted.

Table 3.2: Boundary conditions for plug test case.

	Burnt gas inlet	Unburned gas inlet
u (m/s)	130.0	65.0
v (m/s)	.0	.0
w (m/s)	.0	.0
turb. int.	10 %	10 %
k (m^2/s^2)	253.5	63.37
$\mathcal{L}$ (m)	.02	.08
λ	.1	.1
ϵ (m^2/s^3)	181626	5675
ϕ	1.0	.8
Y_{CO_2}	.11177	.0
Y_{H_2O}	.10624	.0
Y_{CO}	.02084	.0
Y_{O_2}	.01612	.233
Y_{OH}	.00520	.0
Y_{H_2}	.00074	.0
f	.05500	.04450

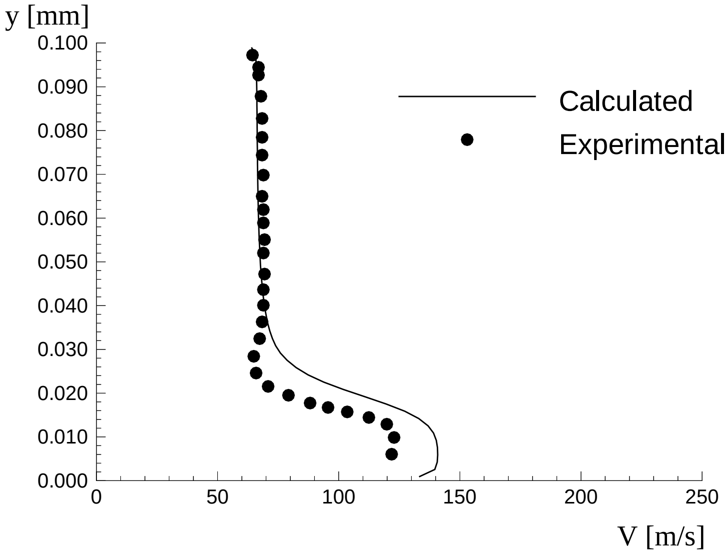

Figure 3.4: Mean velocity profiles at 39 mm from inlets: comparison with experimental data.

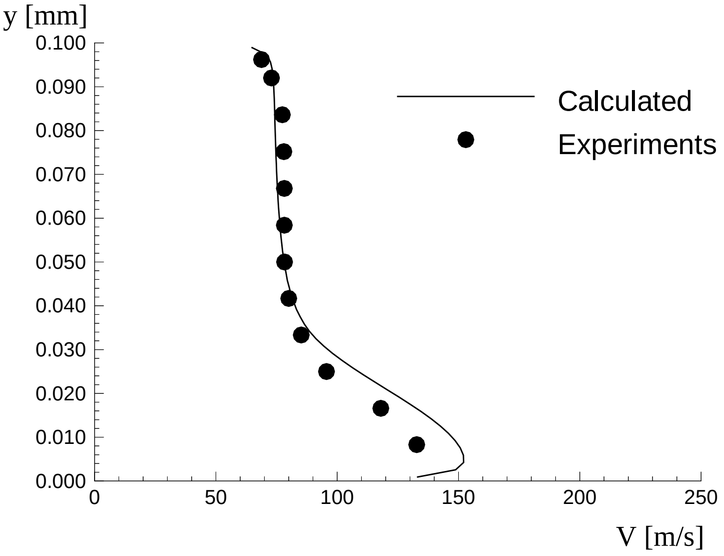

Figure 3.5: Mean velocity profiles at 151 mm from inlets: comparison with experimental data.

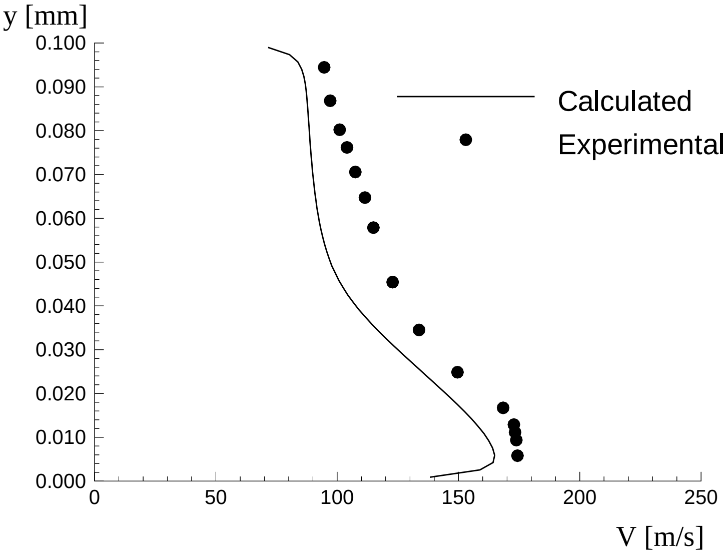

Figure 3.6: Mean velocity profiles at 351 mm from inlets: comparison with experimental data.

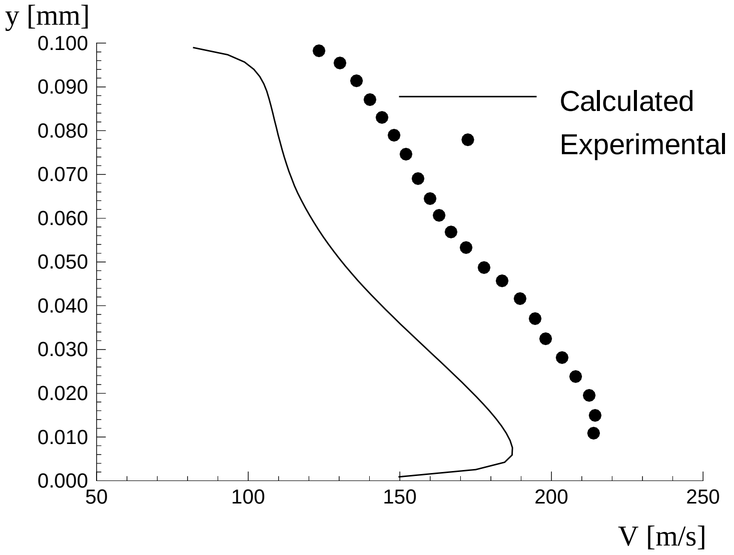

Figure 3.7: Mean velocity profiles at 650 mm from inlets: comparison with experimental data.

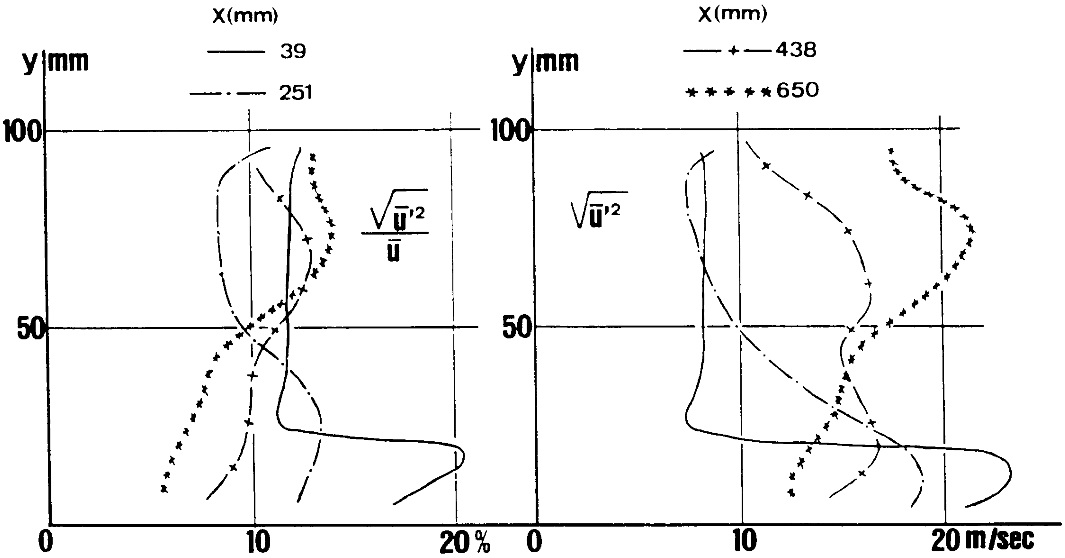

Figure 3.8: Turbulent rate and velocity fluctuation in x direction: profiles measured at different axial sections. Figure taken from Ref. [17].

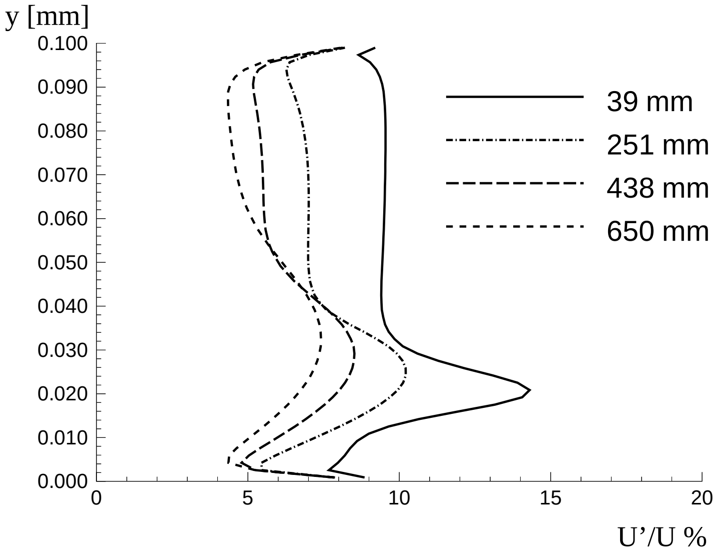

Figure 3.9: Ratio between velocity fluctuation and mean velocity in *x* direction: profiles calculated at different axial sections.

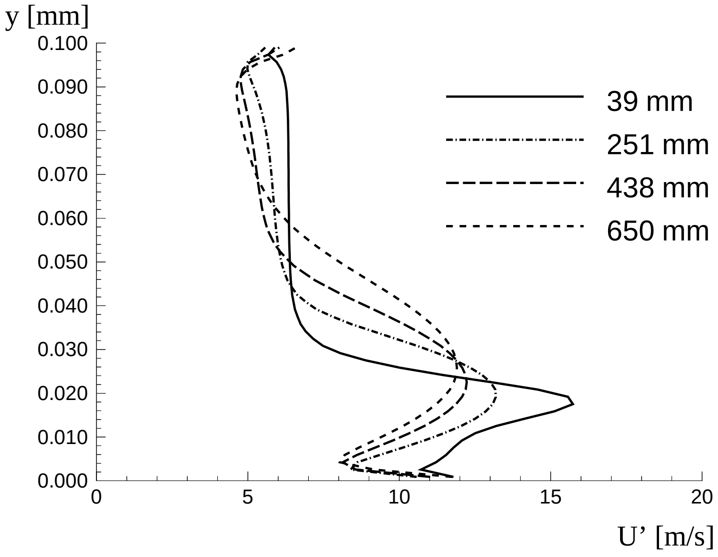

Figure 3.10: Velocity fluctuation in *x* direction: calculated profiles at different axial sections.

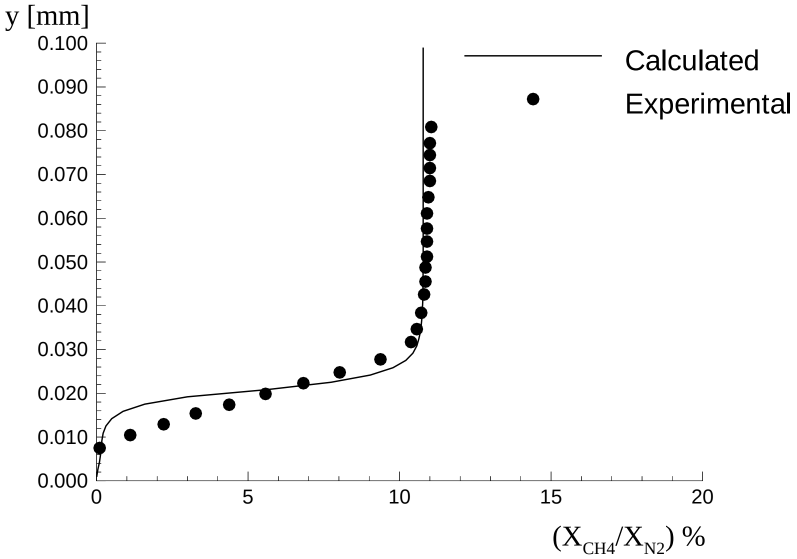

Figure 3.11: Comparison between calculations and experiments for CH_4 molar fractions scaled using N_2 molar fractions: profiles at 22 mm from inlet.

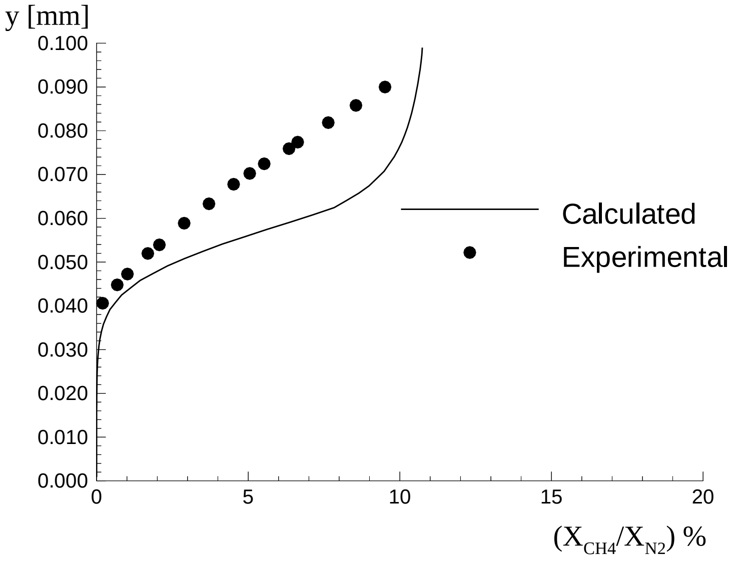

Figure 3.12: Comparison between calculations and experiments for CH_4 molar fractions scaled using N_2 molar fractions: profiles at 522 mm from inlet.

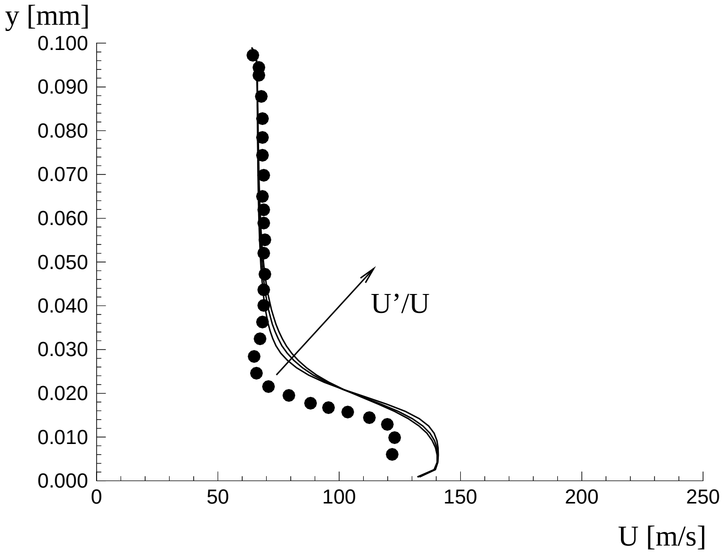

Figure 3.13: Mean velocity profiles at 39 mm from inlet: comparison for different inlet levels of turbulent intensity (10, 15, 20 %).

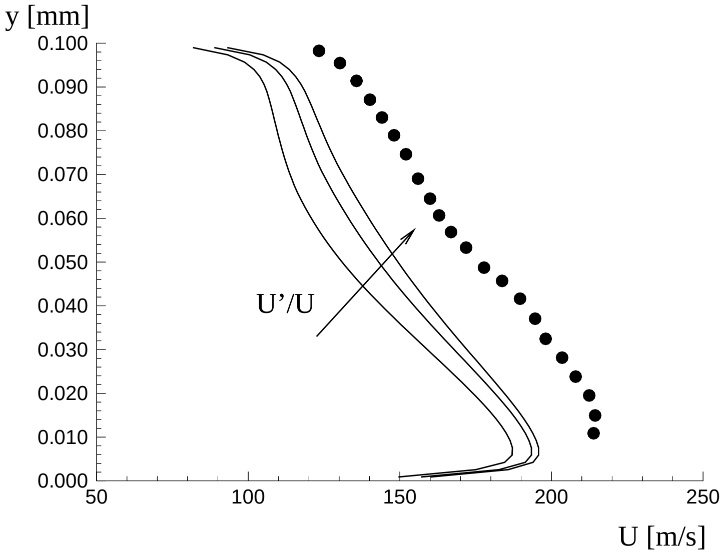

Figure 3.14: Mean velocity profiles at 650 mm from inlet: comparison for different inlet levels of turbulent intensity (10, 15, 20 %).

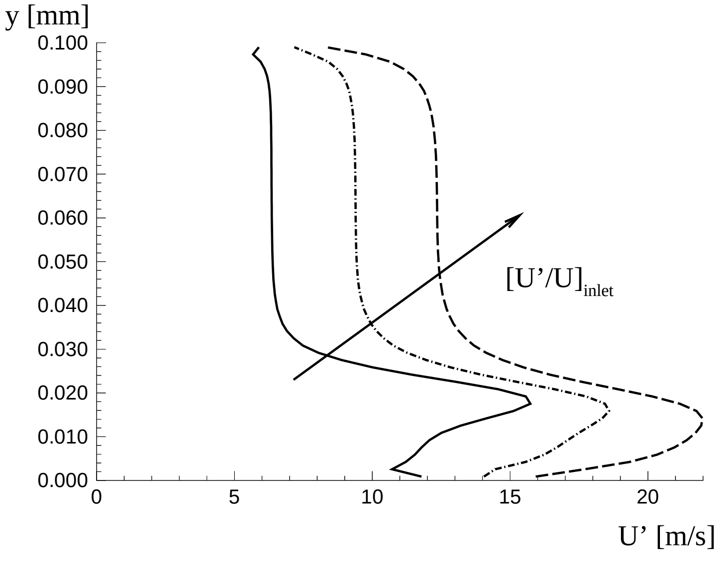

Figure 3.15: Velocity fluctuation profiles at 39 mm from inlet: comparison for different inlet levels of turbulent intensity (10, 15, 20 %).

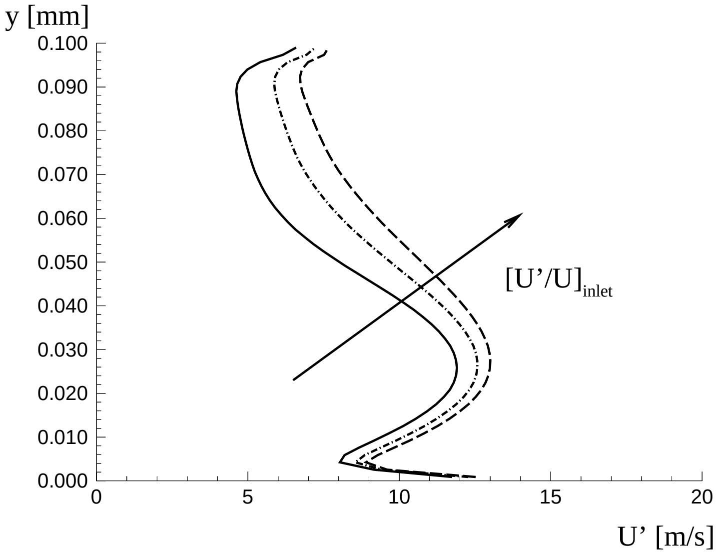

Figure 3.16: Velocity fluctuation at 650 mm from inlet: comparison for different inlet levels of turbulent intensity (10, 15, 20 %).

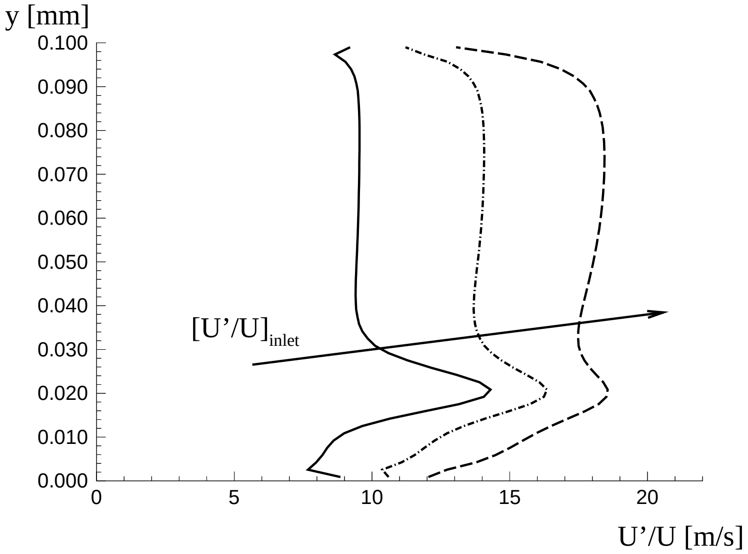

Figure 3.17: Turbulence intensity profiles at 39 mm from inlet: comparison for different inlet levels of turbulent intensity (10, 15, 20 %).

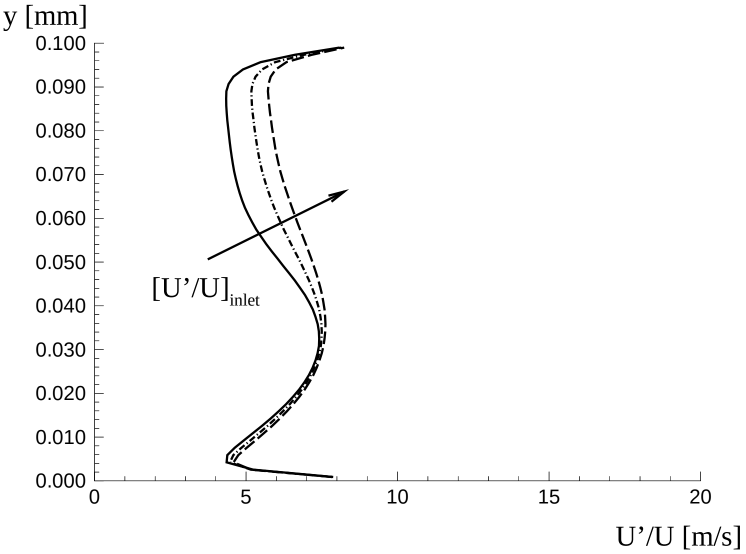

Figure 3.18: Turbulence intensity profiles at 650 mm from inlet: comparison for different inlet levels of turbulent intensity (10, 15, 20 %).

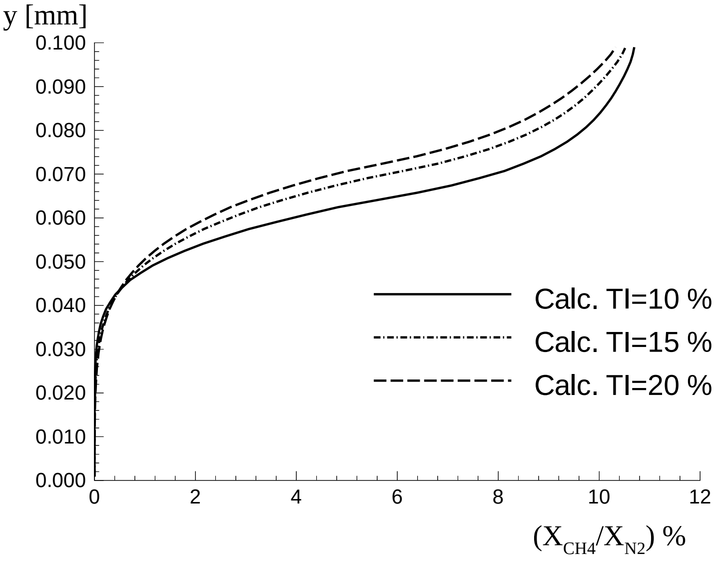

Figure 3.19: CH_4 concentration profiles at 650 mm from inlet: comparison for different inlet levels of turbulent intensity (10, 15, 20 %).

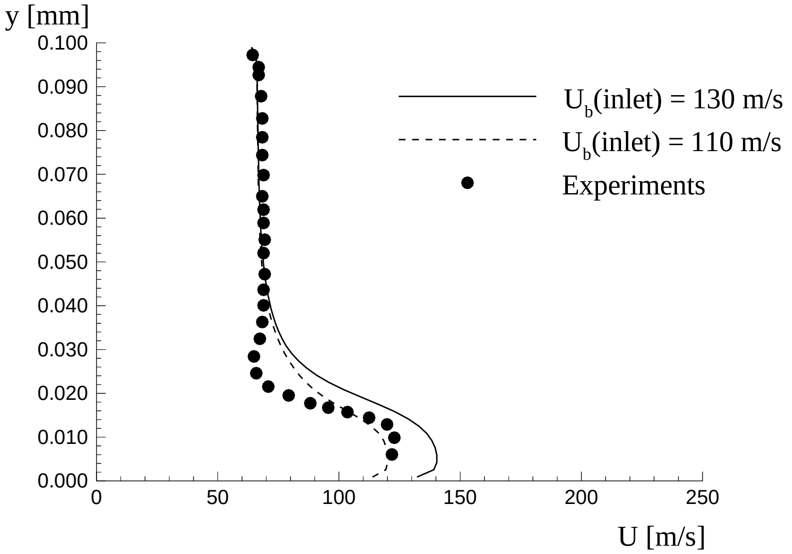

Figure 3.20: Mean velocity profiles at 39 mm from inlet: comparison for different values of inflow velocity.

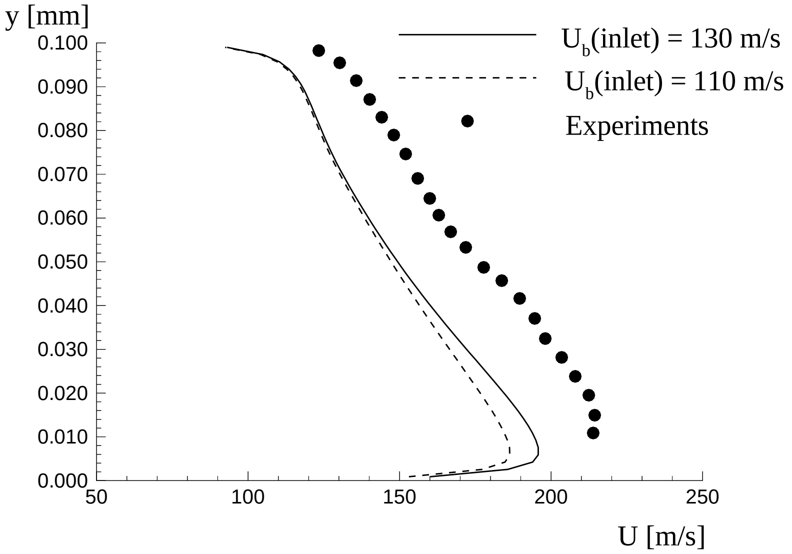

Figure 3.21: Mean velocity profiles at 650 mm from inlet: comparison for different values of inflow velocity.

Chapter 4

Combustion Model Tuning

4.1 Introduction

In this Chapter results of the EDC-PSR combustion model tuning are presented. The tuning has been done with the aim of reproducing at best the experimental measurements of the Moreau combustor presented in the previous Chapter.

4.2 Inlet and boundary conditions

Inlet conditions for the test cases presented here have been assessed on the basis of the results obtained in the previous Chapter and are resumed in Table 4.2. Also in this case, flat profiles for all vectorial and scalar quantities have been imposed at inlets. The other boundary conditions and the computational grid used are the same.

4.3 Combustion model tuning

The EDC-PSR model tuning has been performed acting on the value of the fine structures mass fractions, increasing the value defined in the original version of the EDC model. These has been decided to obviate to the too poor burning found using the original EDC combustion model for the Moreau combustor.

In this Chapter the results labelled "EDC Mod 1" have been obtained assuming that the relation between fine structure regions and mass fraction of fine structures is:

$$\gamma^* = (\gamma)^2 \tag{4.1}$$

Table 4.1: Inlet conditions: case 1.

	Burnt gas inlet	Unburnt gas inlet
u (m/s)	110.0	65.0
v (m/s)	.0	.0
w (m/s)	.0	.0
turb. int.	18 %	13 %
k (m^2/s^2)	253.5	63.37
$\mathcal{L}$ (m)	.02	.08
λ	.07	.07
ϵ (m^2/s^3)	1.673E+6	3.252E+4
ϕ	1.0	.8
Y_{CO_2}	.11177	.0
Y_{H_2O}	.10624	.0
Y_{CO}	.02084	.0
Y_{O_2}	.01612	.22263
Y_{OH}	.00520	.0
Y_{H_2}	.00074	.0
f	.05500	.04450

whereas for the EDC original approach it is $\gamma^* = (\gamma)^3$ (see Section 2.7.4). The second set of results, labelled "EDC Mod 2", has been obtained by assuming:

$$\gamma^* = (\gamma) \quad . \tag{4.2}$$

4.3.1 Axial velocity profiles results

Figures 4.1 - 4.4 show comparisons among calculated (lines) and experimental (dots) mean velocities taken at several section along the combustor.

Figures 4.1 and 4.2 show that calculations reproduce well experiments and the best agreement has been achieved with the *EDC Mod 1*. These results are much more satisfactory than those reported for the same sections in the previous Chapter. This supports the conclusions drawn there concerning mean velocity and turbulence intensity at inlets.

However, results obtained at 351 and 650 mm from inlets show that this agreement is not longer conserved by the *EDC Mod 1* (see Figs. 4.3 and 4.4). At these locations the *EDC Mod 2* shows the best agreement with experiments. This let us to conclude that the turbulent flame speed obtained using *EDC Mod 1* is still too low and leads to a too small flame angle. On the contrary, the *EDC Mod 2*, which assumes the mass fraction of fine structures be identical to the mass fraction of fine structures region, seem able to reproduce with good agreement turbulent flame velocity and angle.

4.3.2 Fuel concentration profiles

Figures 4.5-4.8 present CH_4 volume concentration profiles scaled using N_2 concentration. Similar to what has been seen for mean axial velocity, the first two figures show a fair agreement of our calculations with experiments. The major problem shown by these results is that the EDC model is not capable of reproducing the flame brush width. This is well shown by the difference in slope of calculated and experimental results. The EDC flame is much thinner and its width does not vary very much along the combustor, whereas experiments show a flame brush which becomes thicker and thicker as expected for this regimes of Intermediate Steady Propagation Flames [19].

4.4 Integral length scale increase

A further experiment has been performed on this test case with the aim of reproducing the flame measured flame thickness. After model tuning, the turbulent length scale has been slightly increased assigning a value of 10 % of the inlet dimensions. A summary of the final inlet conditions adopted for this test is shown in Table 4.5 and the results are reported in Figs. 4.9 – 4.13. The largest differences with respect to the previous case can be found in Figs. 4.11 and 4.12. Figure 4.13 shows a small increase of the flame thickness but the disagreement with experimental CH_4 concentration is still relevant.

4.5 Conclusions

From the results presented in this Chapter it is possible to conclude that the EDC-PSR model performs better when the original value of the mass fraction of burning fine structures is increased. A suitable value for the exponent for the mass fraction of fine structures region, γ is in the range $1 \div 2$. This tuning action made the model burning rate much near to the experimental results how it is shown by the better agreement of calculations with the mean velocity experimental data. The model has been found unable in reproducing the real width of the flame brush, which resulted

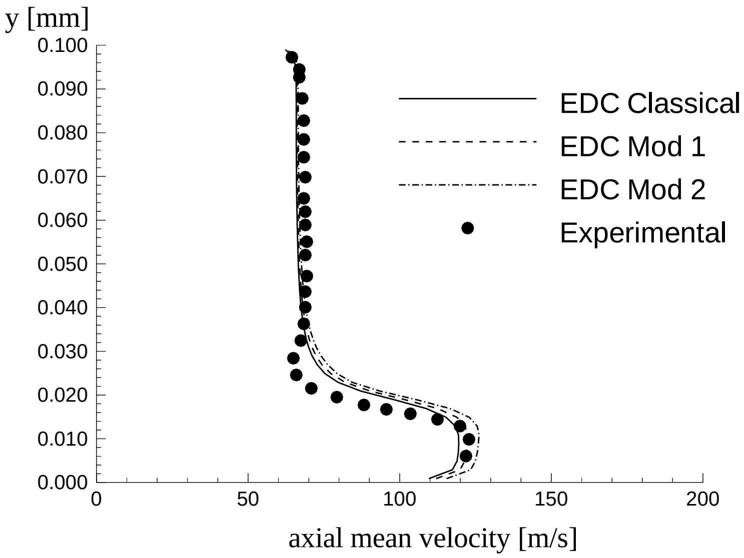

Figure 4.1: Mean velocity profiles at 39 mm from inlets: comparison with experimental data.

much more thin than the measured one and with thickness almost constant along the combustor. A tiny amelioramemt for this point has been found changing the integral length scale at inlets, but definitive progresses should not be possible being this behaviour a characteristic weak point of this combustion model as reported also in [20].

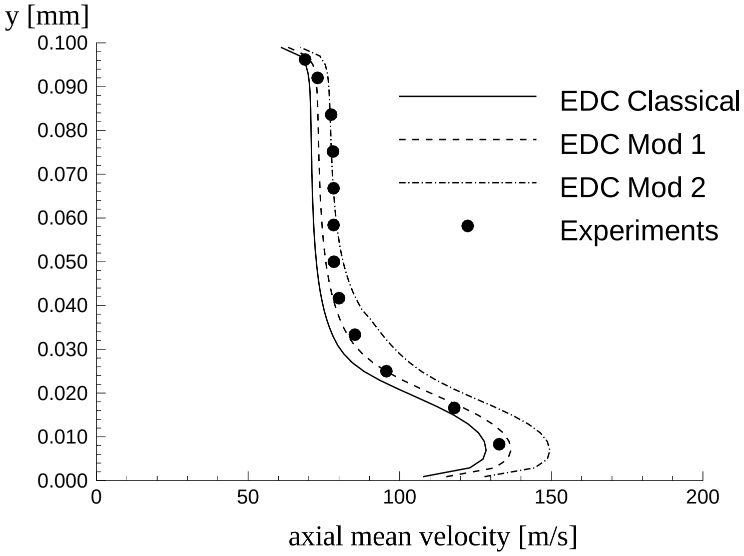

Figure 4.2: Mean velocity profiles at 151 mm from inlets: comparison with experimental data.

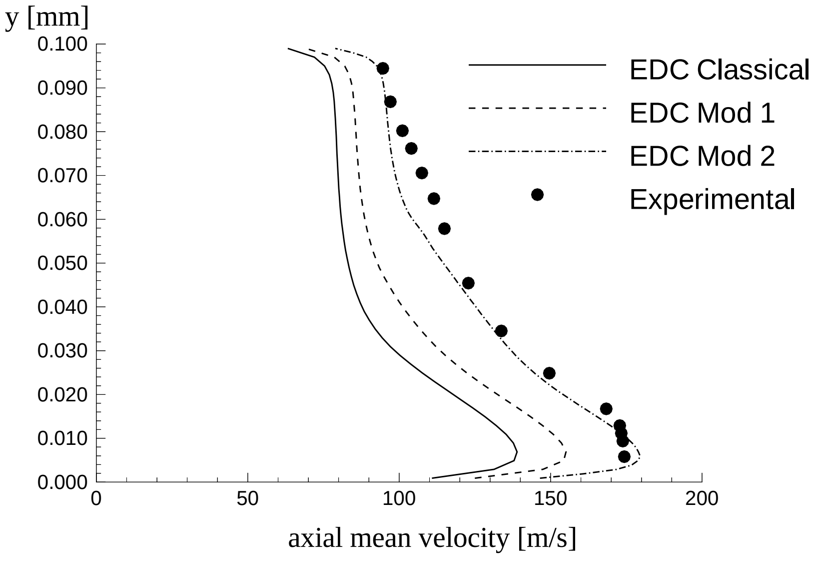

Figure 4.3: Mean velocity profiles at 351 mm from inlets: comparison with experimental data.

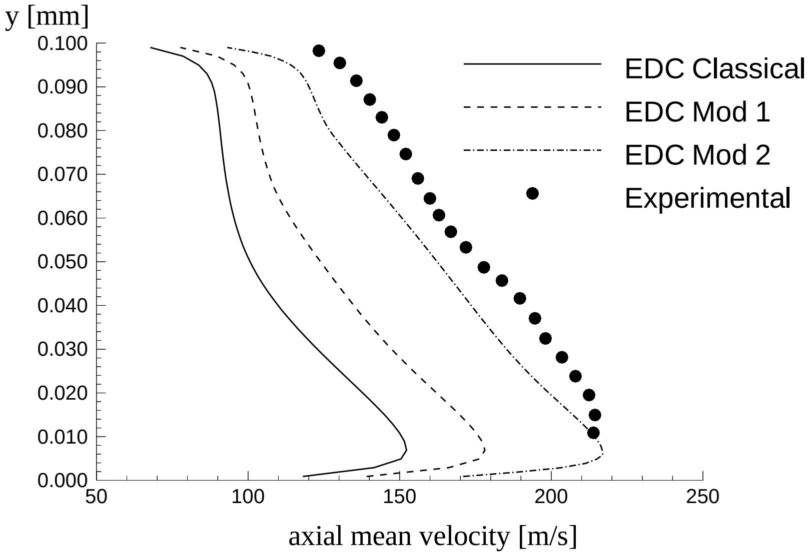

Figure 4.4: Mean velocity profiles at 650 mm from inlets: comparison with experimental data.

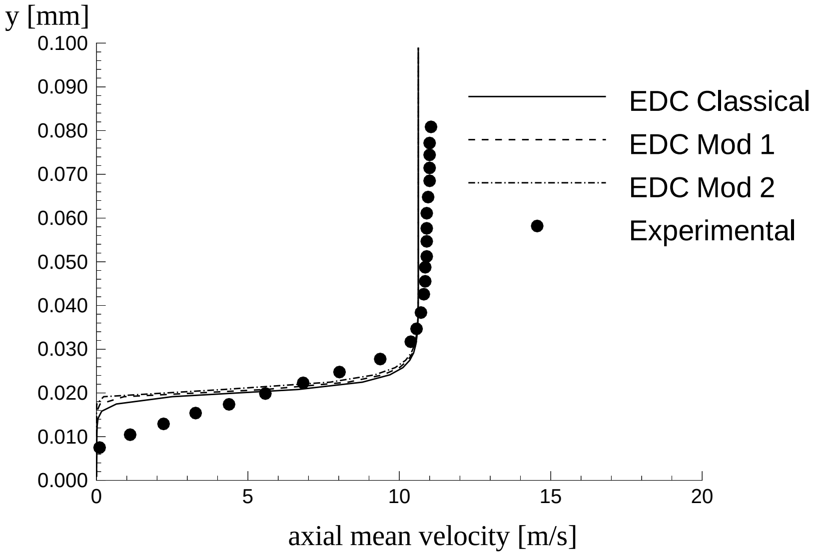

Figure 4.5: CH_4 molar fractions profiles scaled using N_2 molar fractions at 22 mm from inlet: comparison with experimental data.

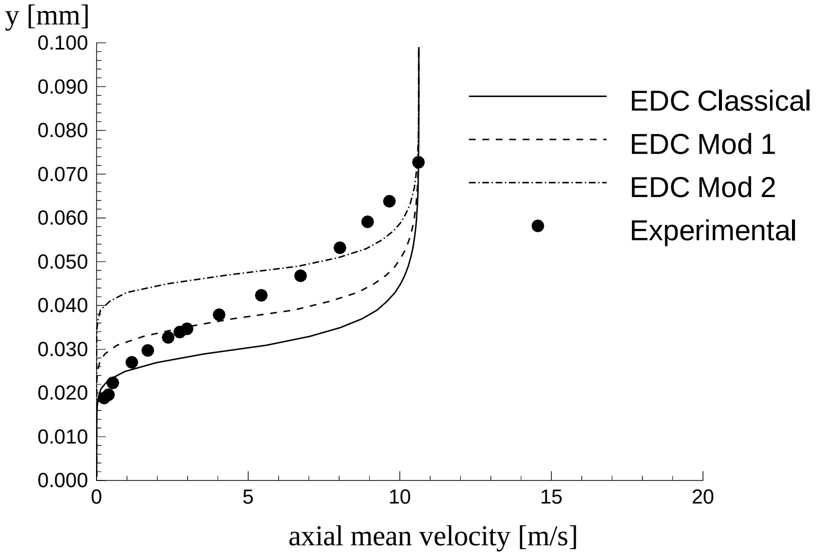

Figure 4.6: CH_4 molar fractions profiles scaled using N_2 molar fractions at 222 mm from inlet: comparison with experimental data.

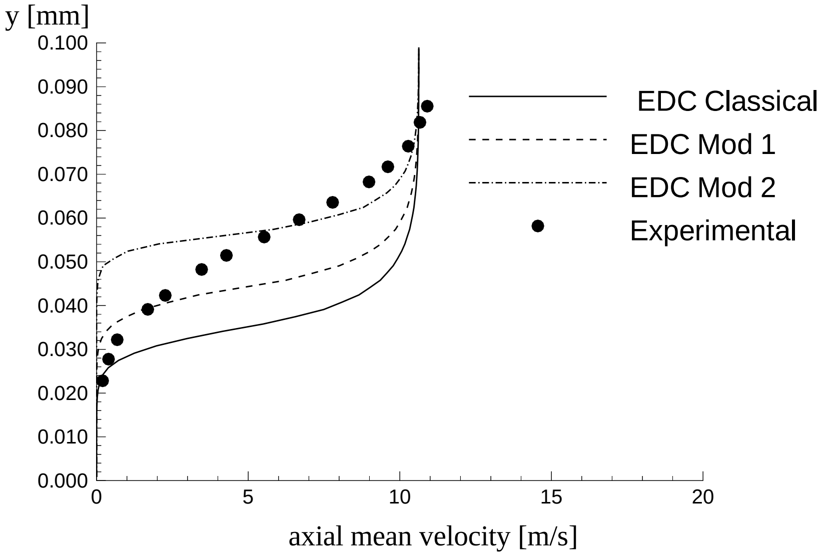

Figure 4.7: CH_4 molar fractions profiles scaled using N_2 molar fractions at 322 mm from inlet: comparison with experimental data.

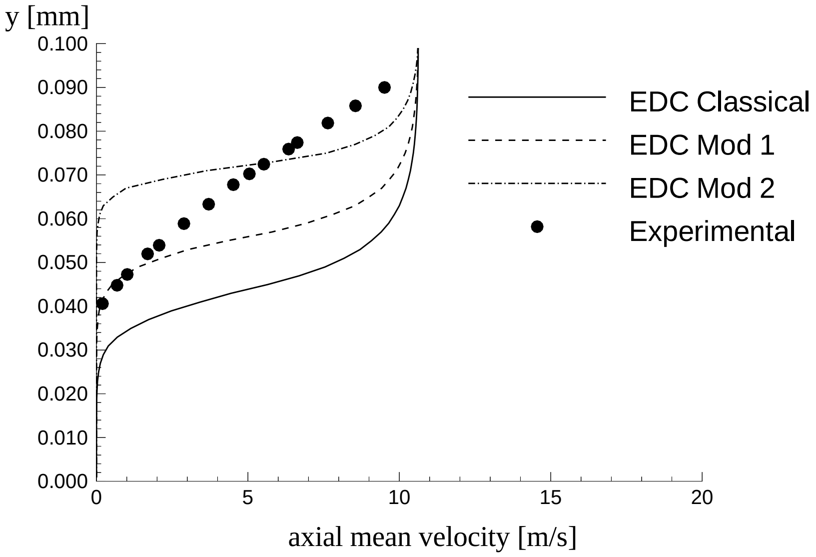

Figure 4.8: CH_4 molar fractions profiles scaled using N_2 molar fractions at 522 mm from inlet: comparison with experimental data.

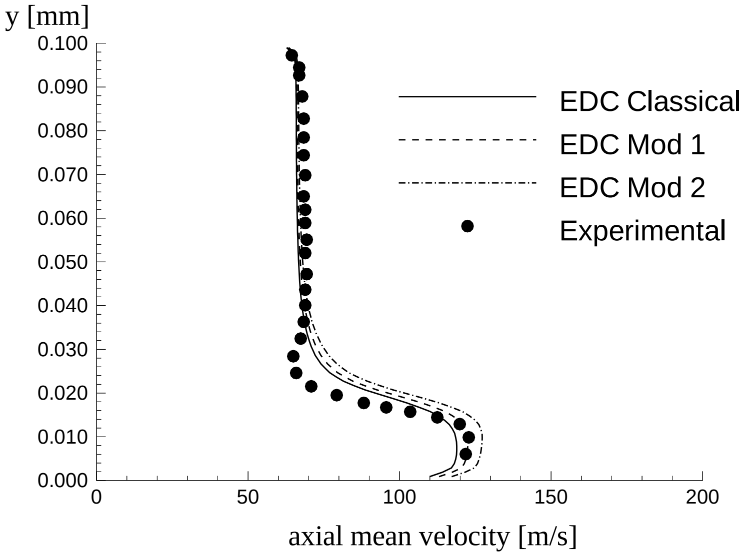

Figure 4.9: Mean velocity profiles at 39 mm from inlets: comparison with experimental data.

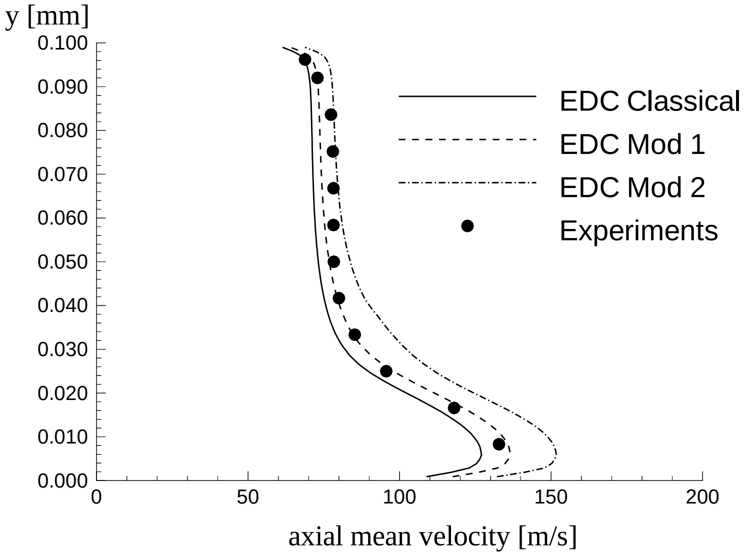

Figure 4.10: Mean velocity profiles at 151 mm from inlets: comparison with experimental data.

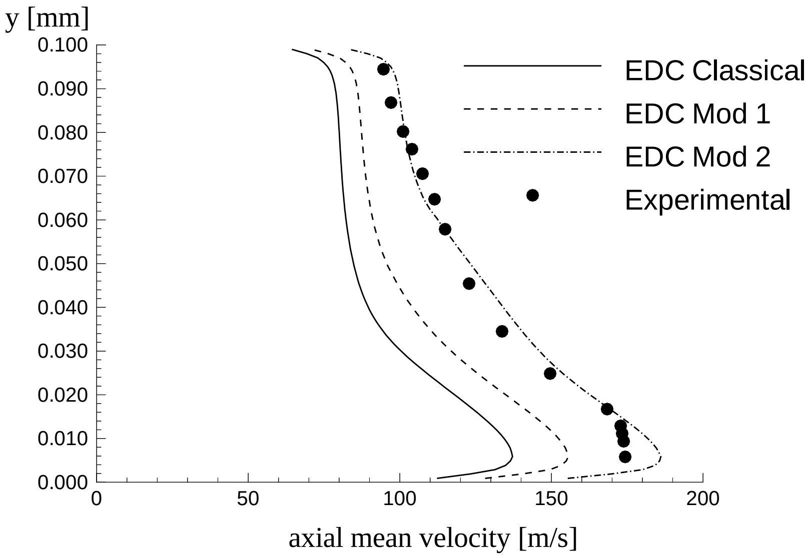

Figure 4.11: Mean velocity profiles at 351 mm from inlets: comparison with experimental data.

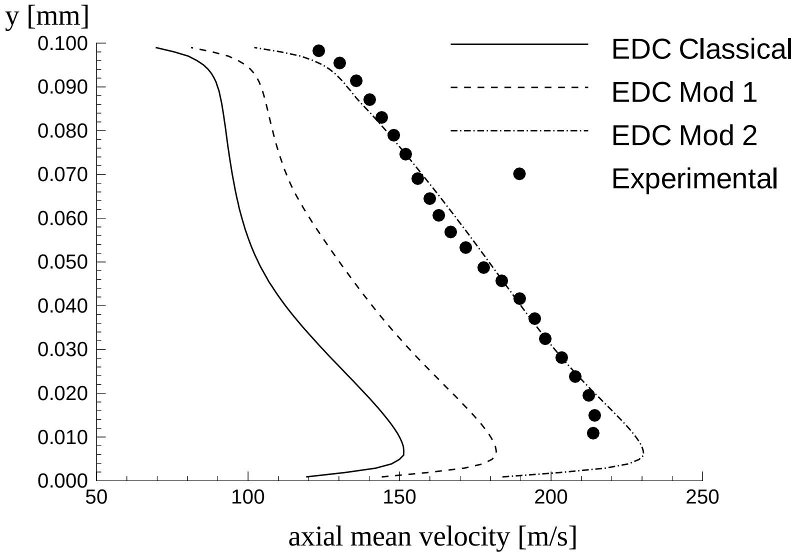

Figure 4.12: Mean velocity profiles at 650 mm from inlets: comparison with experimental data.

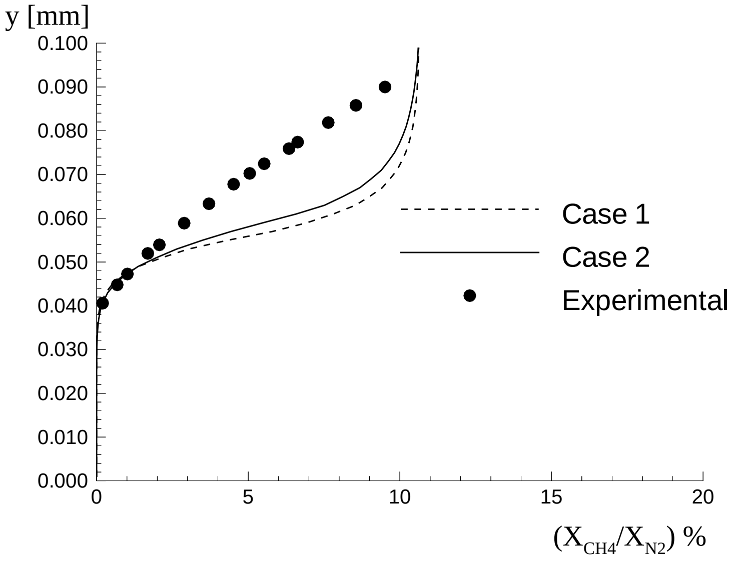

Figure 4.13: CH_4 molar fractions profiles scaled using N_2 molar fractions at 522 mm from inlets: comparison of "Mod 1" results varying turbulent length scale at inlet.

Table 4.2: Inlet conditions: case 2.

	Burnt gas inlet	Unburnt gas inlet
u (m/s)	110.0	65.0
v (m/s)	.0	.0
w (m/s)	.0	.0
turb. int.	18 %	13 %
k (m^2/s^2)	253.5	63.37
$\mathcal{L}$ (m)	.02	.08
λ	.1	.1
ϵ (m^2/s^3)	1.673E+6	3.252E+4
ϕ	1.0	.8
Y_{CO_2}	.11177	.0
Y_{H_2O}	.10624	.0
Y_{CO}	.02084	.0
Y_{O_2}	.01612	.22263
Y_{OH}	.00520	.0
Y_{H_2}	.00074	.0
f	.05500	.04450

Chapter 5

ILDM Reduced Chemistry Software

5.1 Introduction

Combustion of hydrocarbons is a process which involves very complicate chemical kinetics. Depending on the fuel used the number of species can go from tenths to hundreds and the number of reactions from hundreds to thousandths. The complexity of the chemical scheme is only part of the whole problem. A further origin of complexity is the large scattering of time scales which govern the combustion processes. In fact, these times scales can range from 10^{-9} to 10^{2} covering a range which is much wider than time scales representative of physical phenomena (e.g., diffusion). These characteristics lead to modeling equation systems which are very stiff and require special solution methods. But is really necessary to account for such a complicate phenomena? If we think that the detection of radicals such as OH and O is particularly important for the correct evaluation of the NO_x formation processes, we realize that such a kind of chemical kinetics information are necessary for a combustion simulation process intended to evaluate pollutants emissions. In any case the effort requested to include such a complicate processes in a CFD simulation is nowadays still far from being realizable.

5.2 The ILDM approach

A way of keeping a sufficient amount of chemical kinetic information together with an affordable numerical approach is offered by reduced reaction mechanisms which can reproduce, more or less exactly, main features of the original chemical kinetics. Besides the classical reduction methods based on global assumptions of partial equilibrium for some of the reaction steps and steady state for some of the chemical species, different approaches exist which make possible to keep a larger amount of chemical kinetics information. One of these approaches is the Intrinsic Low-Dimensional Manifold method [21] which is an automatic reduction method for generating simplified kinetic schemes. This method is based on a dynamical analysis of the chemical kinetics equations for the combustion process. To express in few word the approach we can say that for an assigned chemical kinetics mechanism the source terms Jacobian matrix is calculated. This is done by performing a response analysis of the source terms vector to the perturbation in all possible directions of the chemical species composition. Then an analysis of the Jacobian eigenvalues and eigenvectors is performed. Eigenvalues are associated with the typical chemical time scales whereas the eigenvectors are are associated with reaction groups. In this way it is possible to identify, in the reaction space, some "attractive" low dimensional sub-spaces where local equilibrium with respect to the fastest time scales exist [21]. The name attractive given to these manifolds is because, whichever are the initial conditions in the reaction space, after some fast relaxation process, the reaction trajectories approach the manifold where the progress of the reaction goes according to the slow time scales and proceeds up to a stationary condition which coincides with the chemical equilibrium condition. Being interested only to the sub-spaces, neglecting fast relaxation processes, it is possible to describe the whole chemical reaction system which a number of variables which is much smaller even though the content of kinetic information is still high.

This method gives reduced reaction mechanism with a wide range of validity contrary to what occurs to classical reduction approaches. In fact, the reduction conditions are applied locally and therefore don't have any constraint, such, for example, a specific mixture composition. The simplification of the detailed kinetics mechanism is done automatically optimizing the assumptions, which have a local validity in the space of compositions, once the number of degree of freedom has been fixed.

Furthermore, a major advantage of ILDM-reduced chemistry is the good estimation of minor species which, as already said above, are particularly important to predict pollutants.

5.3 ILDM software description

The Heidelberg software for ILDM tables is a complete package which allows to use the reduced chemistry for CFD simulations of combustion flows. The package contains all the thermo-chemical information of the chemical kinetics mechanism and has an internal structure which is completely transparent to the user. The package, depending on the complexity of the reduced mechanism, requires input values for two or three progress variables, for the mixture fraction (which can be absent for tables with fixed composition of the reactants) and the time increment. Output of this software are the updated values of progress variables, plus other thermo-chemical information such as mass fractions, mass density and temperature (see Fig. 5.1). Therefore the tables can also be used to look up mixture composition, temperature and density.

The tables already available from the Type II LowNOx program are those for Syngas and Methane. These software packages contain the FORTRAN routines plus the table database.

The first ILDM table is for a stoichiometric mixture of Syngas (0.4% CO, 0.3% H_2, 0.3% N_2) and air (0.21 % O_2, and 0.79 % N_2). It has been set up for a unburned mixture temperature of 298 K and enthalpy of -6.574·10^5 J/kg. The progress variables are CO_2 and H_2O and the stored properties are six mass fractions (CO_2, H_2O, CO, H_2, O_2, O), density and temperature of the mixture.

The second table is for Methane-air combustion. In this case the table is for a wide range of mixture fraction (0.001 $\div$ 0.999) and therefore can also be used for non premixed combustion test cases. The progress variables are CO_2 and H_2O, and the properties tabulated are four mass fractions (CO_2, H_2O, O, and N_2), mixture density and temperature. For this table the unburned mixture temperature is 298 K.

A new generation of tables has been produced in the framework of the LES/PDF-ECT project [22] for kerosene and propane.

For the kerosene table, dodecane has been taken as representative of this complex fuel. A detailed chemical kinetics mechanism with 38 species and 320 elementary reaction steps has been used to design an ILDM table which has four tabulation coordinates: two progress variables (CO_2 and H_2O), temperature and mixture fraction. This table has been optimized applying a new approach to handle molecular diffusion and mixing. In fact for a "conventional" ILDM table for kerosene less than 1 % of the memory storage is devoted to chemistry information, the rest contains data to handle molecular transport [22]. This new procedure lead to much more compact tables and can also allow to produce tables of acceptable dimensions even for very complex chemical kinetic mechanisms.

5.3.1 Implementation

How explained in the previous Chapters, the combustion model implemented in the `GTTURBO_EDC` code requires the solution of the adiabatic Perfectly Stirred Reactor equations : Eqs. (2.46) plus the obvious relation (2.47). The PSR solver implemented has been taken from the CHEMKIN library [8]. To write Eqs. (2.46) we need to know, for all chemical species accounted for, the molar rate of production by chemical reaction per unit volume: $\dot{\omega}_i$. When a detailed or a classical reduced mechanism is available, these quantities are assembled starting from rate expressions and chemical species concentration. Using the ILDM tables in the format available, we had to approximate the molar rate of production as follows:

$$\dot{\omega}_i \simeq \frac{Y_i^{new} - Y_i^{old}}{\Delta t} \rho \frac{1}{W_i} \quad \text{mole/(cm}^3\text{ s)} \quad i = 1, NS \tag{5.1}$$

where ρ is the mass density and Δt is the time increment. This expressions have been used both for progress variables and for the other tabulated chemical species.

The system of Eqs.(2.46) is solved using an iterative procedure (Newton Method); for each step of this procedure the ILDM software is called to build up the updated set of molar rates of production. Therefore, during the solution of the ODE system, a high number of calls to the table occurs. Furthermore, being mixture temperature and density, besides some of the mass fractions, available by table look up, the code has been modified to use calls to the tables each time these quantities have to be calculated.

A major problem has been found in setting up the complete set of mass fractions. The first generation of ILDM software, as already seen, besides the progress variables give some other mass fractions but not the complete set. To reproduce the chemistry in the PSR, the set of mass fractions has to be as much complete as possible. In fact, lack of “important” chemical species can lead to an inconsistence between the tabulated mechanism and the chemistry involved in the PSR. Therefore, being conscious of the approximation, conservation of elements has been used to increase the number of species mass fraction already available from the ILDM software output.

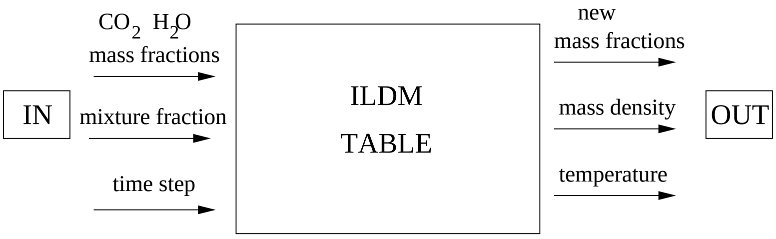

Figure 5.1: ILDM tables schematic

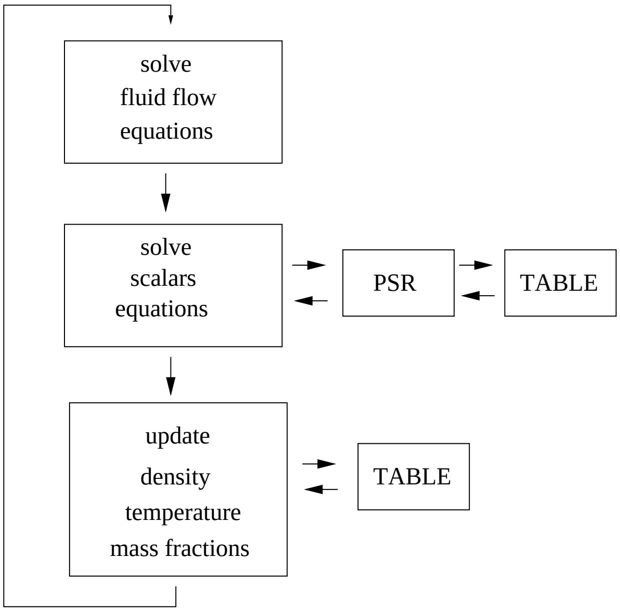

Figure 5.2: Flow chart of CFD code – ILDM tables coupling.

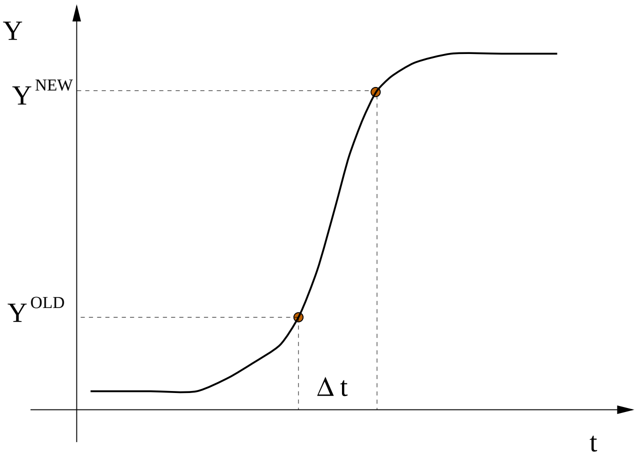

Figure 5.3: Reaction progress.

Chapter 6

Classical Reduced Reaction Mechanisms

6.1 Westbrook and Dryer 2 steps mechanism

An example of reduced reaction mechanism is the 2 steps mechanism for hydrocarbons oxidation proposed by Westbrook and Dryer [23]. In this mechanism the reaction rates have been empirically derived to fit the laminar premixed flame speed obtained with a detailed mechanism. The mechanism has been set up for a large number of hydrocarbons (up to decane $C_{10}H_{22}$).

The Westbrook and Dryer 2-step global mechanism reads:

$$\begin{array}{ccccccccc} C_nH_m & + & \left(\frac{n}{2}+\frac{m}{4}\right) O_2 & \rightarrow & nCO & + & \frac{m}{2} H_2O & & (I) \\ CO & + & \frac{1}{2} O_2 & \rightleftharpoons & CO_2 & & & & (II) \end{array} \tag{6.1}$$

with the following reaction rates (units are *cm-sec-mol-K-kcal*):

$$w_1 = A \exp(-E_a/\mathcal{R}T)\,[CH_4]^a\,[O_2]^b \tag{6.2}$$

$$w_{2f} = 10^{14.6} \exp(-40.0/\mathcal{R}T)\,[CO]\,[H_2O]^{0.5}\,[O_2]^{0.25} \tag{6.3}$$

$$w_{2b} = 5 \cdot 10^8 \exp(-40/\mathcal{R}T)\,[CO_2] \tag{6.4}$$

where for reaction (II) the backward contribution is also accounted. Coefficients for the reaction (I) rate for three different fuels are reported in Table 6.1. In this mechanism there are $NS = 5$ chemical species (C_nH_m, O_2, CO, H_2O, CO_2) and $NE = 3$ elements (C, O and H); Nitrogen N_2 can be considered to be a diluent.

Table 6.1: Westbrook-Dryer rates coefficients

Fuel	A	E_a	a	b
CH_4	2.8×10^9	48.4	-0.3	1.3
C_3H_8	1.0×10^{12}	30.0	0.1	1.65
CH_4	4.7×10^{11}	30.0	0.25	1.5

6.2 Peters' four steps mechanism

This mechanism has been obtained starting from a skeletal mechanism reported in Table 6.2 [24, 25]. It consists of 35 elementary steps among 15 reacting species CH_4, O_2, CO_2, H_2O, CO, H_2, H, OH, O, HO_2, CH_3, CHO, CH_2O, CH_3O, H_2O_2 plus N_2 which is considered as a passive diluent.

By analyzing results obtained with the detailed mechanism, Peters recommended steady state assumption for the the following 8 chemical species (radicals): OH, O, HO_2, CH_3, CHO, CH_2O, CH_3O, H_2O_2. Instead, the reactions considered to be the the fastest are R2, R3, R7, R13, R14, R17, R20, R22.

The final reduced reaction mechanism reads:

$$\begin{array}{ccccccccccc} CH_4 & + & 2H & + & H_2O & = & CO & + & 4H_2 & & (I) \\ & & CO & + & H_2O & = & CO_2 & + & H_2 & & (II) \\ & & 2H & + & M & = & H_2 & + & M & & (III) \\ & & O_2 & + & 3H_2 & = & 2H & + & 2H_2O & & (IV) \end{array} \tag{6.5}$$

The chemical species involved are 8, CH_4, CO, H, O_2, H_2, H_2O, CO_2, N_2 with 4 elements, C, O, H, N; The reaction rates are for the four steps are:

$$w_I = (w_{10f} - w_{10b}) + (w_{11f} - w_{11b}) + (w_{12f} - w_{12b}) \tag{6.6}$$

$$w_{II} = w_{9f} - w_{9b} \tag{6.7}$$

$$w_{III} = w_5 - (w_{10f} - w_{10b}) + w_{16} - w_{18} + w_{19} - w_{21} + (w_{23f} - w_{23b}) + w_{24} + w_{25} \tag{6.8}$$

$$w_{IV} = (w_{1f} - w_{1b}) + w_6 + w_{18} + w_{21} - (w_{23f} - w_{23b}) \tag{6.9}$$

Peters assumes that the contribution of the radicals, because of their negligible concentration with respect to the main species, can be neglected. Therefore, the independent parameters are given by the molar numbers of the chemical species appearing in the reduced mechanism.

Besides Peters assumes that less significant reaction rates in the strongly non-linear steady state relations can be neglected too.

The concentration of OH downstream the flame front, where equilibrium is reached, can be calculated to leading order from the equilibrium of reactions 3f and 3b:

$$[OH] = \frac{k_{3b}\,[H_2O]\,[H]}{k_{3f}\,[H_2]} \tag{6.10}$$

The concentrations of O and CH_3 are given from their steady state relations by:
O:

$$\begin{aligned} k_{1f}\,[H]\,[O_2] \quad + & \quad k_{2b}\,[OH]\,[H] + k_{4f}\,[OH]^2 = \\ & [O]\,\{k_{1b}\,[OH] + k_{2f}\,[H_2] + k_{4b}\,[H_2O] + k_{13}\,[CH_3] \end{aligned} \tag{6.11}$$

CH_3:

$$\begin{aligned} \{k_{11f}\,[H] \quad + & \quad k_{12f}\,[OH]\}\,[CH_4] = \\ & [CH_3]\,\{k_{10b}\,[H]\,[M] + k_{11b}\,[H_2] + k_{12b}\,[H_2O] + k_{13}\,[O]\} \end{aligned} \tag{6.12}$$

Reaction 18 doesn't appear in this relations because its effect is negligible. Eliminating $[CH_3]$ between the two relations yields:

$$[O] = \frac{-(B\,D + k_{13}\,(C - A)) + \sqrt{(B\,D + k_{13}\,(C - A))^2 + 4\,k_{13}\,B\,A\,D)}}{2\,k_{13}\,B} \tag{6.13}$$

where

$$\begin{aligned} A &= k_{1f}\,[H]\,[O_2] + k_{2b}\,[OH]\,[H] + k_{4f}\,[OH]^2 && (6.14) \\ B &= k_{1b}\,[OH] + k_{2f}\,[H_2] + k_{4b}\,[H_2O] && (6.15) \\ C &= \{k_{11f}\,[H] + k_{12f}\,[OH]\}[CH_4] && (6.16) \\ D &= k_{10b}\,[H]\,[M] + k_{11b}\,[H_2] + k_{12b}\,[H_2O] && (6.17) \end{aligned}$$

Solving the steady state relations for $[CH_3O]$, $[CH_2O]$ and $[HCO]$ in terms of $[OH]$, $[O]$ and $[CH_3]$ yields:

$$\begin{aligned} [CH_3O] &= \frac{k_{18}\,[CH_3]\,[O_2]}{k_{19}\,[H] + k_{20}\,[M]} && (6.18) \\ [CH_2O] &= \frac{k_{13}\,[CH_3]\,[O] + (k_{19}\,[H] + k_{20}\,[M])\,[CH_3O]}{k_{14}\,[H] + k_{15}\,[OH]} && (6.19) \\ [HCO] &= \frac{(k_{14}\,[H] + k_{15}\,[OH])\,[CH_2O]}{k_{16}\,[H] + k_{17}\,[M]} && (6.20) \end{aligned}$$

The steady state relation for $[HO_2]$ may be truncated by considering only the rates of reactions 5-8, since the others, involving $[HO_2]$, are small. This leads to

$$[HO_2] = \frac{k_5\,[H]\,[O_2]\,[M]}{(k_6 + k_7)\,[H] + k_8\,[OH]} \tag{6.21}$$

Finally, the steady state relation for $[H_2O_2]$ leads to

$$[H_2O_2] = \frac{k_{21}\,[HO_2]^2 + k_{22b}\,[OH]^2\,[M] + k_{23b}\,[H_2O]\,[HO_2]}{k_{22f}\,[M] + k_{23f}\,[OH]} \tag{6.22}$$

Some other reaction rates appearing in the rates (6.6)-(6.9) of the reduced mechanism can be eliminated because unimportant. Following Rogg [26], for example, these rates are approximated as:

$$\begin{aligned} w_I &= w_{11f} + w_{12f} && (6.23)\\ w_{II} &= w_{9f} - w_{9b} && (6.24)\\ w_{III} &= w_{16} + w_5 + w_{24} && (6.25)\\ w_{IV} &= w_{1f} - w_{1b} && (6.26) \end{aligned}$$

Therefore, reaction 10 has been neglected from w_I and w_{II}; reactions 18, 19, 21, 23, 25 have been neglected from w_{III} and reactions 6, 18, 21, 23 from w_{IV}.

The number of thermochemical independent parameters can be further reduced by three units, by writing the linear relations expressing the conservation of the mass of elements:

$$\begin{aligned} n_H^{(el)} &= n_H + 2\,n_{H_2} + 2\,n_{H_2O} + 4\,n_{CH_4} && (6.27)\\ n_O^{(el)} &= 2\,n_{O_2} + 2\,n_{CO_2} + n_{H_2O} + n_{CO} && (6.28)\\ n_C^{(el)} &= n_{CH_4} + n_{CO} + n_{CO_2} && (6.29)\\ n_N^{(el)} &= 2\,n_{N_2} && (6.30) \end{aligned}$$

where $n_i^{(el)}$ is the mole number of element i $(kmol/kg)$. Also in these relations, the contribution given by the steady state radicals has been neglected. Each of the elements mole numbers can be related to the mixture fraction f by the relations:

$$\begin{aligned} n_H^{(el)} &= \frac{4\,f}{W_{CH_4}} && (6.31)\\ n_O^{(el)} &= \frac{2\,\psi\,(1-f)}{\psi\,W_{O_2} + W_{N_2}} && (6.32)\\ n_C^{(el)} &= \frac{f}{W_{CH_4}} && (6.33)\\ n_N^{(el)} &= \frac{2\,(1-f)}{\psi\,W_{O_2} + W_{N_2}} + \frac{2\,f}{W_{N_2}} && (6.34) \end{aligned}$$

with $\psi = 0.21/0.79$. The number of independent parameters is given therefore by the number of chemical species involved, NS, minus the number of steady state assumption relations, S, minus the number of chemical elements, NE, plus 1: 16-8-4+1=5 .

No.	Reaction	A	α	E
1f.	$H + O_2 = OH + O$	$2.000E+14$	0.000	70.30
1f.	$OH + O = H + O_2$	$1.570E+13$	0.000	2.89
2f.	$O + H_2 = OH + H$	$1.800E+10$	1.000	36.93
2b.	$OH + H = O + H_2$	$8.000E+09$	1.000	28.29
3f.	$H_2 + OH = H_2O + H$	$1.170E+09$	1.300	15.17
3b.	$H_2O + H = H_2 + OH$	$5.090E+09$	1.300	77.78
4f.	$OH + OH = O + H_2O$	$6.000E+08$	1.300	0.00
4b.	$O + H_2O = OH + OH$	$5.900E+09$	1.300	71.26
5.	$H + O_2{+}M = HO_2{+}M$	$2.300E+18$	-0.800	0.00
6.	$H + HO_2 = OH + OH$	$1.500E+14$	0.000	4.20
7.	$H + HO_2 = H_2 + O_2$	$2.500E+13$	0.000	2.93
8.	$OH + HO_2 = H_2O + O_2$	$2.000E+13$	0.000	4.18
9f.	$CO + OH = CO_2 + H$	$1.510E+07$	1.300	-3.17
9b.	$CO_2 + H = CO + OH$	$1.570E+09$	1.300	93.74
10f.	$CH_4{+}M = CH_3 + H{+}M$	$6.300E+14$	0.000	435.19
10b.	$CH_3 + H{+}M = CH_4{+}M$	$5.200E+12$	0.000	-5.48
11f.	$CH_4 + H = CH_3 + H_2$	$2.200E+04$	3.000	36.61
11b.	$CH_3 + H_2 = CH_4 + H$	$9.570E+02$	3.000	36.61
12f.	$CH_4 + OH = CH_3 + H_2O$	$1.600E+06$	2.100	10.29
12b.	$CH_3 + H_2O = CH_4 + OH$	$3.020E+05$	2.100	72.90
13.	$CH_3 + O = CH_2O + H$	$6.800E+13$	0.000	0.00
14.	$CH_2O + H = HCO + H_2$	$2.500E+13$	0.000	16.70
15.	$CH_2O + OH = HCO + H_2O$	$3.000E+13$	0.000	5.00
16.	$HCO + H = CO + H_2$	$4.000E+13$	0.000	0.00
17.	$HCO{+}M = CO + H{+}M$	$1.600E+14$	0.000	61.51
18.	$CH_3 + O_2 = CH_3O + O$	$7.000E+12$	0.000	107.34
19.	$CH_3O + H = CH_2O + H_2$	$2.000E+13$	0.000	0.00
20.	$CH_3O{+}M = CH_2O + H{+}M$	$2.400E+13$	0.000	120.56
21.	$HO_2 + HO_2 = H_2O_2 + O_2$	$2.000E+12$	0.000	0.00
22f.	$H_2O_2{+}M = OH + OH{+}M$	$1.300E+17$	0.000	190.39
22b.	$OH + OH{+}M = H2O2{+}M$	$1.300E+17$	0.000	190.39
23f.	$H_2O_2 + OH = H_2O + HO_2$	$1.000E+13$	0.000	7.53
23b.	$H_2O + HO_2 = H_2O_2 + OH$	$2.860E+13$	0.000	137.21
24.	$OH + H{+}M = H_2O{+}M$	$2.200E+22$	-2.000	0.00
25.	$H + H{+}M = H_2{+}M$	$1.800E+18$	-1.000	0.00

Table 1. Skeletal mechanism of elementary reactions for $CH_4 - air$ combustion. Individual quantities are expressed in cm, mol, s, kJ, and K units. Coefficients are for the rate expression: $k = AT^{\alpha} \exp(-E/\mathcal{R}T)$.

The third-body efficiencies are 6.5 for CH_4, 0.40 for O_2, 1.50 for CO_2, 6.50 for H_2O, 0.75 for CO, 0.40 for N_2 and 1.00 for all other species.

6.3 Chang and Chen 6-steps mechanism

The 6-steps reduced chemistry mechanism for CH_4-air combustion proposed by Chang and Chen [18]:

$$\begin{array}{ccccccccccccl} & & & & 2O & = & O_2 & & & & & & (I) \\ & & H & + & O & = & OH & & & & & & (II) \\ & & H_2 & + & O & = & H & + & OH & & & & (III) \\ 2O & + & OH & + & 2CH_4 & = & 7H & + & H_2O & + & 2CO & & (IV) \\ & & & & H_2O & = & H & + & OH & & & & (V) \\ & & O & + & CO & = & CO_2 & & & & & & (VI) \end{array} \tag{6.35}$$

Ten chemical species are involved, $H2$, H, O, $O2$, OH, $H2O$, $CH4$, CO, $CO2$, and $N2$. This reduced mechanism, particularly suitable for lean to slightly rich mixtures, has been obtained from the GRI-Mech 1.2 that is a detailed mechanism for methane-air combustion [27] developed at the Gas Research Institute, Chicago. A complete set of routines, in CHEMKIN format, describing this mechanism can be found at the `WEB` site cited in [18].

Chapter 7

ILDM-CFD Testing

7.1 Introduction

The ILDM reduced chemistry software packages for $CO - H_2$ and CH_4 combustion presented in Chapter 5 have been implemented into the CFD code `GTTURBO_EDC` and their performance have been tested simulating the premixed combustor described in Chapter 3. To evaluate the tables behaviour, for the methane case their results have been compared with those obtained using three other "conventional" reduced reaction mechanisms: Westbrook and Dryer [23], Peters [25] and Chang and Chen [18]. For the syngas case, the comparison has been done with results obtained using a skeletal mechanism. Results of these comparisons are shown in Figs. 7.1 – 7.10.

7.2 Results

These results have been obtained with the EDC+PSR original version i.e., without tuning of the combustion model. For the Methane flame, with this version the Westbrook-Dryer mechanism give very low burning leading to the worst performance. Results of Peters and Chang-Chen and ILDM mechanisms show a flame front evolution along the combustor that can be seen by the fuel consumption profiles in Figs. 7.1–7.3. Peters and Chang-Chen have similar behaviour whereas the ILDM shows a peculiar trend especially for the mean temperature which in the flame brush has evident unphysical wiggles. This is due to the PSR source terms formulation (see Section 5.3.1) which, depending on the kinetics, can introduce severe approximations.

The limit of this formulation has been put in evidence also by the $CO - H_2$ flame results. In fact, in this case a substantial difference has been found between results obtained using a skeletal mechanism and the ILDM reduced chemistry (see Figs.

7.7–7.10).

7.3 Conclusions

ILDM tables implemented can give a heavy content of chemical kinetics information requiring to solve just two or three scalar equations. For their use with the EDC-PSR combustion model, the weak point has been found to be the absence of an explicit output of the chemical source terms for a sufficiently large number of chemical species. These tables give mass fraction increments and the consequent approximated evaluation of the source terms has been found unsatisfactory (notice for example the wiggles found in the mean temperature profiles of the methane flame). A modification of the source terms structure, including an attempt of using a variable δt in Eq. (5.1), has not brought to results quality enhancement. Therefore for the combustion model used in this work, ILDM tables, structured to give directly the chemical species source terms instead that the mass fractions increments, should be preferred.

7.4 Optimal ILDM package structure

From the tests performed at CRS4 with the ILDM tables a series of suggestions can be drawn that can represent useful headlines to generate a new family of ILDM software packages:

- the table has not to be generated for an assigned couple of temperature and pressure values. In fact, if p and T are assigned the table can be used only for fuel and air boundary conditions which have these values of temperature and pressure as constraints. Especially for industrial simulations the possibility of make calculations on an assigned geometry changing p and T at inlet is a must. For aero-engines the different flight conditions are a main example.

- the table should give the possibility to the user of choosing the main output format. In fact, depending on the combustion model used, can be more convenient to have chemical species source terms or mass fractions increments.

- output content and complexity: besides main output, e.g., source terms, density and temperature, the user should have the possibility to set the nature and the content of the secondary output. For example choosing mass or molar fractions, specify which set of chemical species have to be traced. A simple example can concern O and OH radicals which are particularly important to map thermal *NO* formation: the table should be able to give the user the possibility of changing the required chemical species and the quantities correlated.

In conclusions, looking at the application to CFD for aero-engines combustors simulations, the optimal ILDM software should be a package which includes these different needs. In fact, in this way, the range of applicability is extended to a variety of operative conditions.

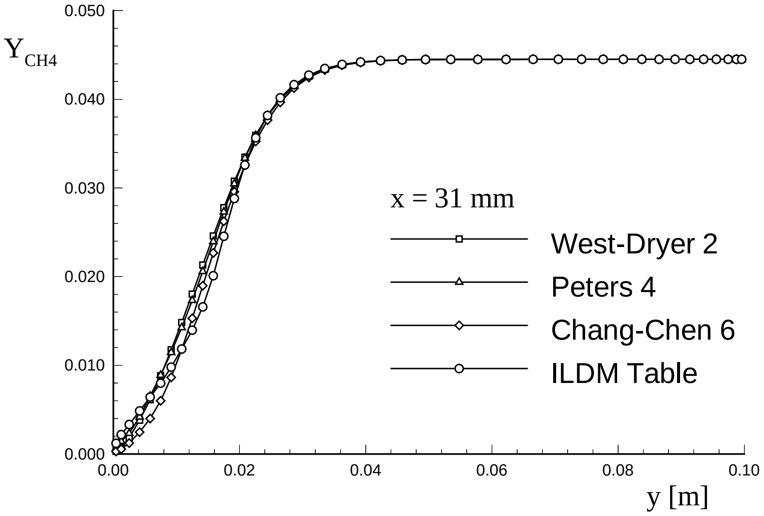

Figure 7.1: Methane mass fractions at 31 mm from inlets: comparison using different reduced reaction approaches.

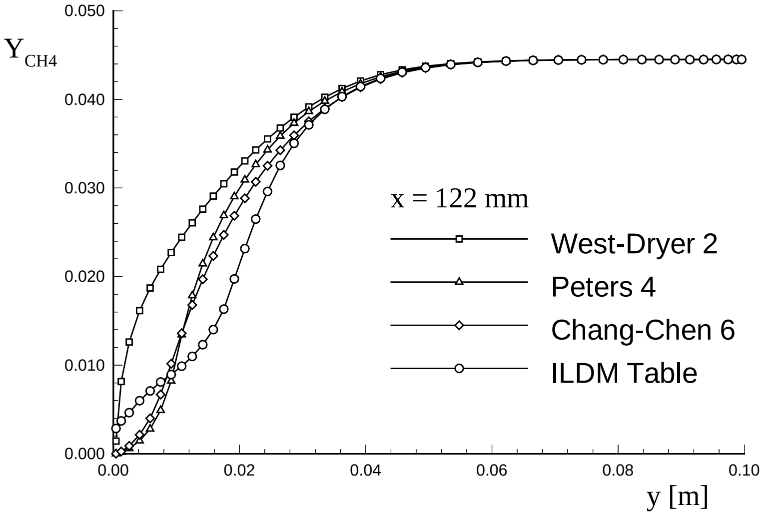

Figure 7.2: Methane mass fractions at 122 mm from inlets: comparison using different reduced reaction approaches.

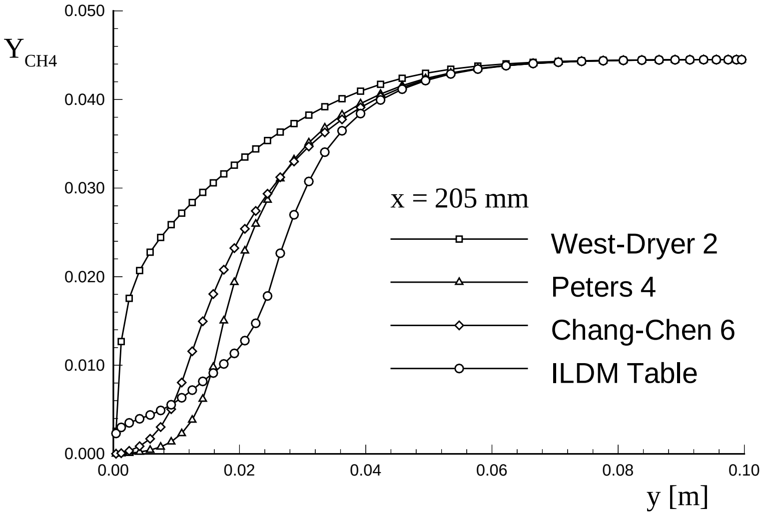

Figure 7.3: Methane mass fractions at 205 mm from inlets: comparison using different reduced reaction approaches.

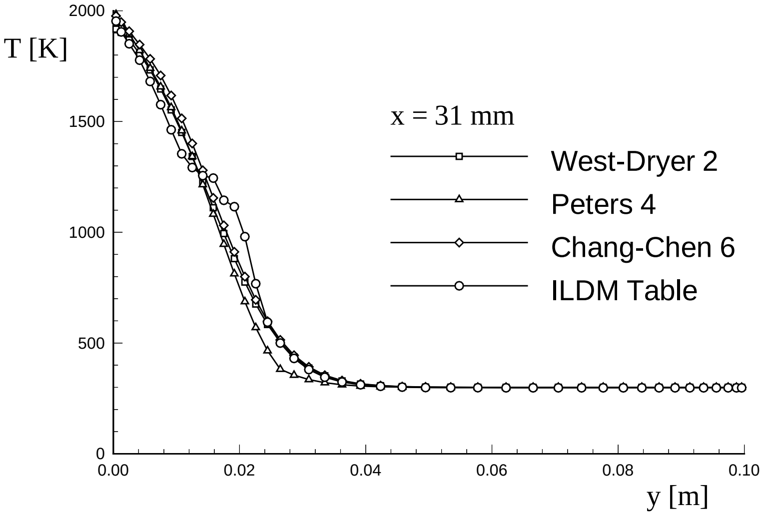

Figure 7.4: Mean temperature at 31 mm from inlets: comparison using different reduced reaction approaches.

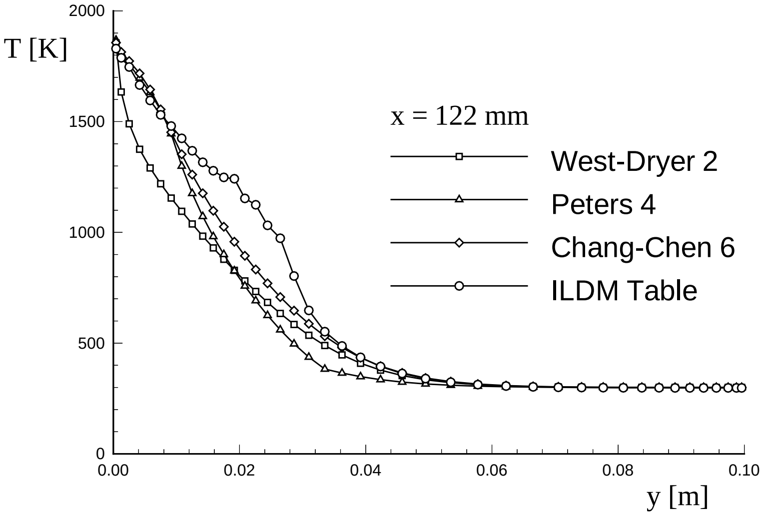

Figure 7.5: Mean temperature at 122 mm from inlets: comparison using different reduced reaction approaches.

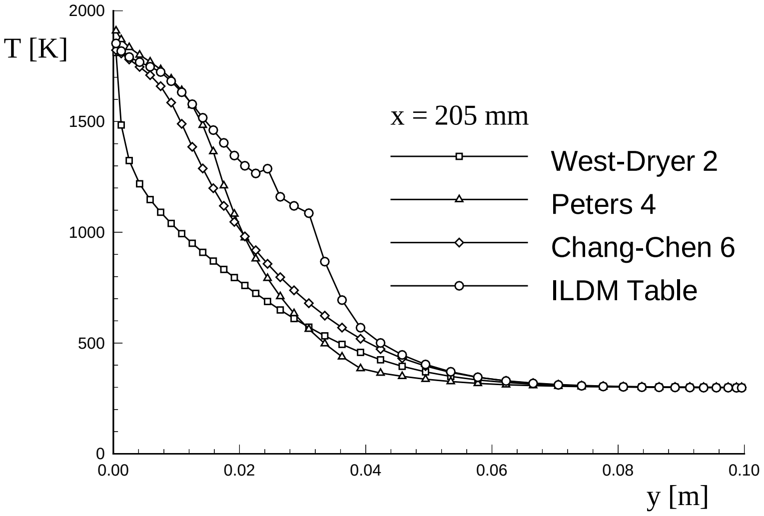

Figure 7.6: Mean temperature at 205 mm from inlets: comparison using different reduced reaction approaches.

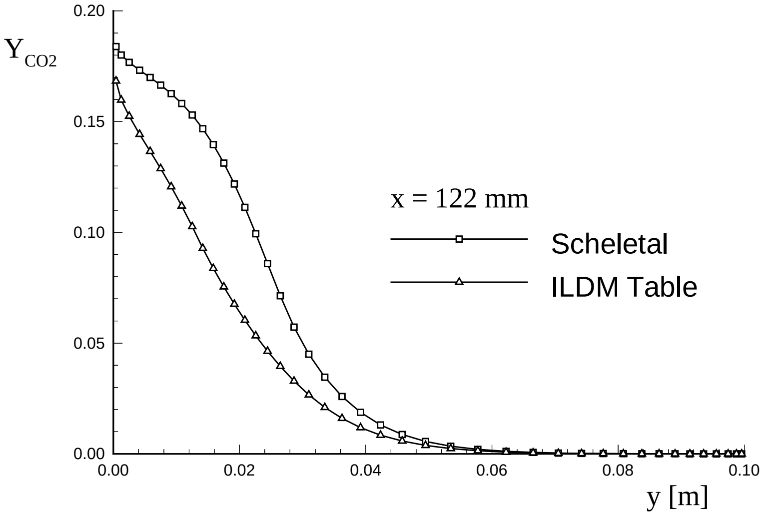

Figure 7.7: CO_2 mass fractions at 122 mm from inlets: comparison using different reduced reaction approaches.

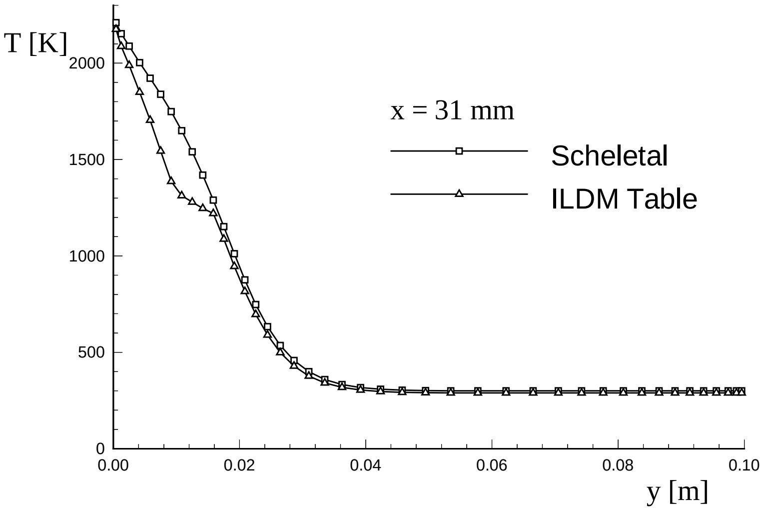

Figure 7.8: Mean temperature at 31 mm from inlets: comparison using different reduced reaction approaches.

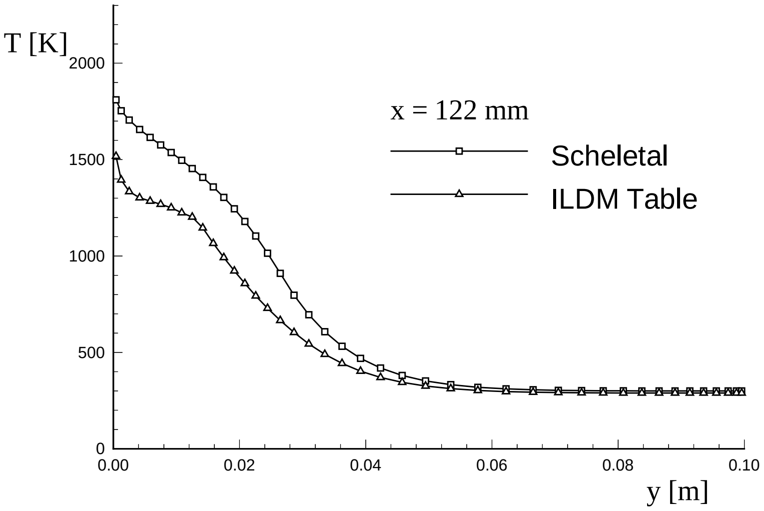

Figure 7.9: Mean temperature at 122 mm from inlets: comparison using different reduced reaction approaches.

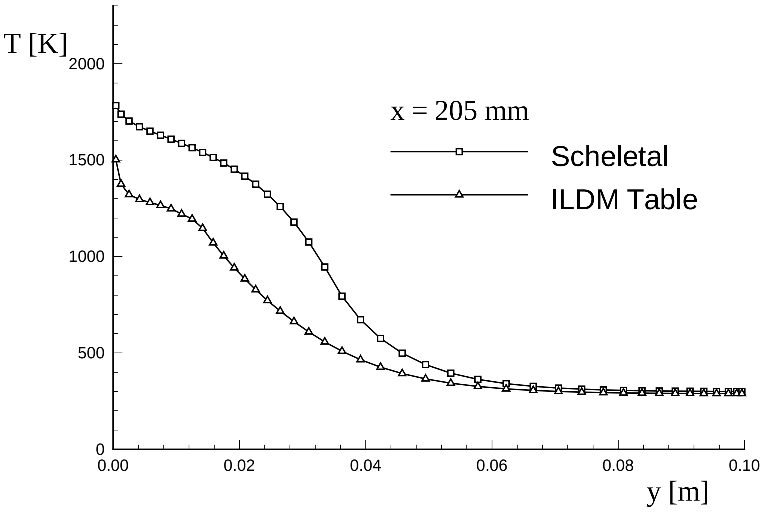

Figure 7.10: Mean temperature at 205 mm from inlets: comparison using different reduced reaction approaches.

7.5 New ILDM tables

The new generation of ILDM tables prepared by the University of Heidelberg incorporates some of the requisites defined after the testing of the first version tables. A schematic of this new tables is reported in Fig. 7.11. The `initial state` is a vector which characterize the system chemical state; it contains T, p, and Y_i. The rates of reactions cited are the rates of variations of temperature, CO_2, H_2O and f [28].

The user access to these new software offer the possibility of defining the output structure, to decide the set of chemical species to monitor besides progress variables. Chemical species source terms are not available among the output features.

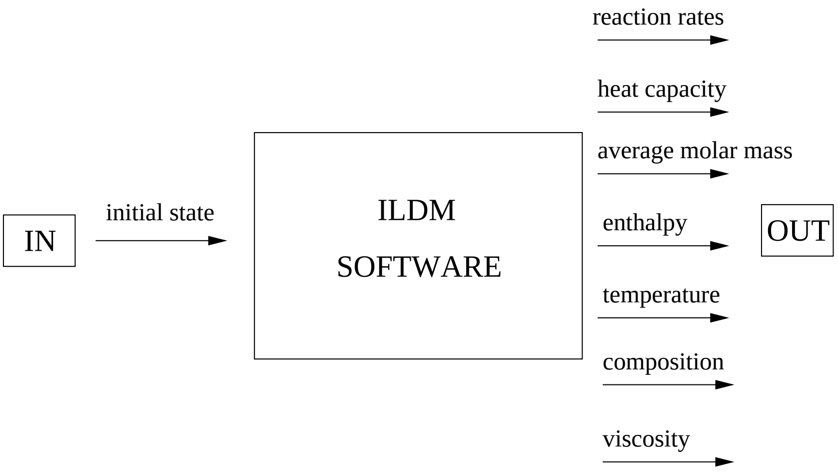

Figure 7.11: New ILDM tables schematic. Actually reaction rates

Chapter 8

EDC+PSR in CFX: an Application

8.1 Introduction

To make available the software developed at CRS4 to all the LowNOx III partners, the EDC-PSR model has been implemented in a commercial code, namely CFX [29]. For this issue, a package of `FORTRAN` routines has been designed and documented. The description of this software is reported in Appendix A. In this Chapter a simple application of this package is presented.

8.2 Test case description

The combustor chosen is an experimental combustor of simple geometry (see Fig. 8.1) feeded with a premixed propane-air mixture with equivalence ratio is $\phi = 0.65$ [30]. The combustor dimensions are: length $L_{ch} = 220mm$, height $H_{ch} = 28.8mm$, depth $W_{ch} = 160mm$. A flame holder ($L = 5mm \times H = 9.6mm$) is used in order to stabilize the flame.

The reduced chemical kinetics mechanism used for this preliminary experiment is a simple two steps mechanism proposed by Westbrook and Dryer [23]:

$$\begin{array}{ccccccccc} C3H_8 & + & 3.5\,O_2 & \rightarrow & 3\,CO & + & 4\,H_2O & & (I) \\ CO & + & \frac{1}{2}O_2 & \rightleftharpoons & CO_2 & & & & (II) \end{array} \qquad (8.1)$$

for which rates expressions can be found in Section 6.1.

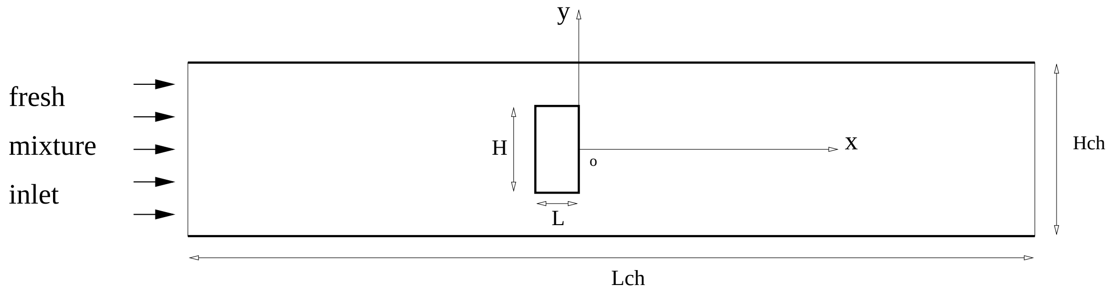

Figure 8.1: Schematic of the ENSMA combustor.

8.3 Inlet and boundary conditions

This test case has been assumed being two dimensional. The two velocity components profiles are reported in Fig. 8.2. A uniform composition profile has been adopted at inlet. Combustor and flame holder walls have been assumed being adiabatic and no-slip conditions have been applied. At combustor exit a pressure outlet condition has been assumed.

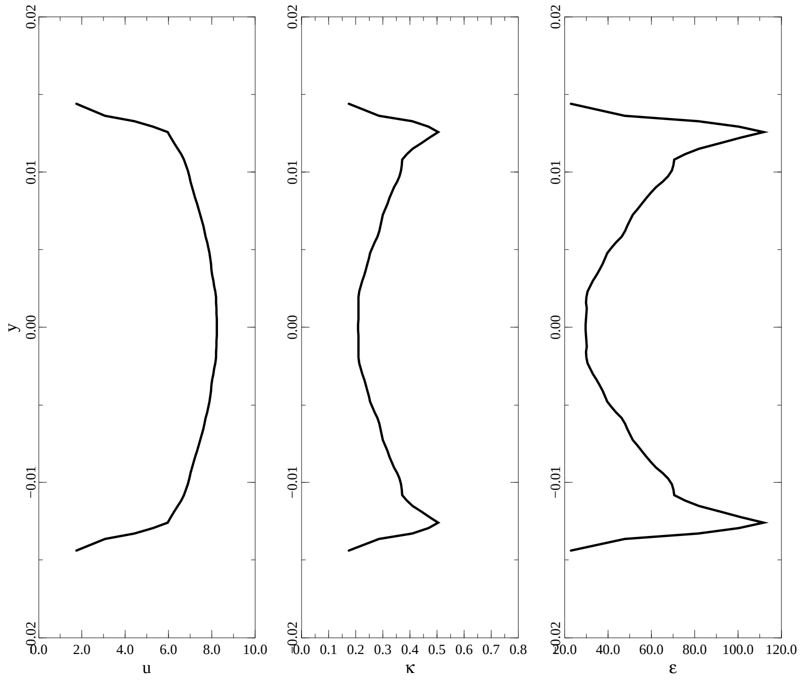

Figure 8.2: Inlet profiles.

8.4 Results

Figures 8.3–8.5 show some of the results obtained using the PSR-EDC combustion model.

Figure 8.3 shows the axial velocity distribution and puts in evidence, behind the obstacle, the presence of a recirculation zone which is able to stabilize the flame.

Figures 8.3–8.5 show the distribution of the fuel and CO mass fractions. The flame shape is qualitatively well represented.

With respect to experiments the temperature field has shown excessively high peak values.

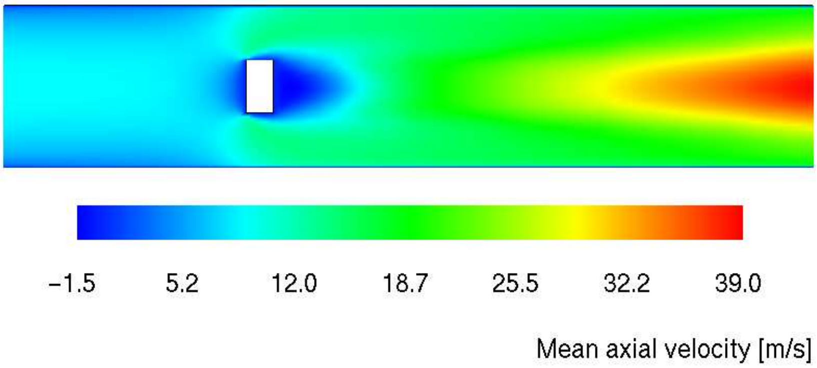

Figure 8.3: ENSMA combustor: axial velocity distribution.

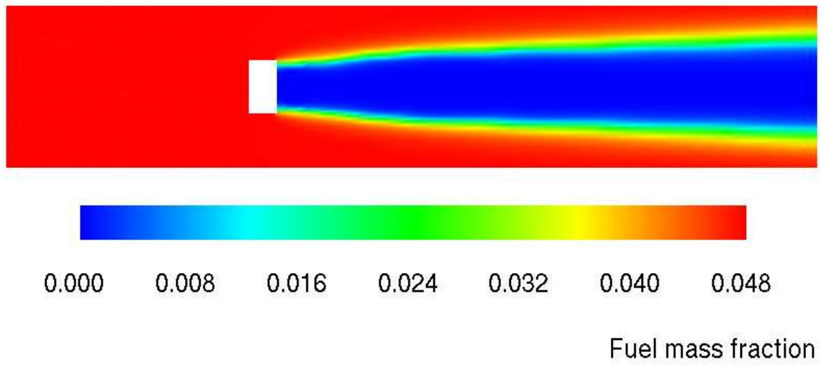

Figure 8.4: ENSMA combustor: fuel mass fraction distribution.

Figure 8.5: ENSMA combustor: CO mass fraction distribution.

Bibliography

[1] Magnussen, B.F. The Eddy Dissipation Concept for Turbulent Combustion Modeling. Its Physical and Practical Implications. *XI Task Leaders Meeting – Energy Conservation in Combustion, IEA*, 1989.

[2] Patankar, S.V. *Numerical Heat Transfer and Fluid Flow.* Hemisphere Publishing Corporation, New York, 1980.

[3] Biagioli, F. Modelling Combustion with PDF methods. *Ph.D. Thesis, University of Rome I, Mechanics and Aeronautics Dept.*, 1995 (in italian).

[4] Jones, W. P. Turbulence Modelling and Numerical Solution Methods for Variable Density and Combusting Flows. In P. A. Libby and F. A. Williams, editors, *Turbulent Reacting Flows*, pages 309–374. Academic Press, 1994.

[5] Batchelor, G. K.,. *An Introduction to Fluid Dynamics.* Cambridge University Press, 1967.

[6] Lilleheie, N.I., Ertesvåg, I., Bjørge, T., Byggstøyl, S., and Magnussen, B.F. Modeling and Chemical Reactions: Review of Turbulence and Combustion Models. *SINTEF Norvegian Institute of Technology, Division of Thermodynamics*, July 11, 1989.

[7] Chomiak J. *Combustion, A Study in Theory, Facts and Application.* Abacus Press/Gordon & Breach Science Publishers, New York, 1990.

[8] Glaborg, P., Kee, R.J., Grcar, J.F., and Miller, J.A. PSR: A Fortran Program for Modeling Well-Stirred Reactors. Technical Report SAND86-8209 UC-4, SANDIA National Laboratories, Reprinted Nov. 1993.

[9] Magnussen, B.F. On the Structure of Turbulence and a Generalized Eddy Dissipation Concept for Chemical Reactions in Turbulent Flow. *19th AIAA Sc. Meeting*, St. Louis - USA, 1981.

[10] Gran, R.I.,. *Mathematical Modeling and Numerical Simulation of Chemical Kinetics in Turbulent Combustion.* PhD thesis, University of Trondheim, Norway, 1994.

[11] Rasmussen, N.B.K. and Myken, A.N. The Eddy Dissipation Kinetic (EDK) Model for Turbulent Reacting Flow and Numerical Implementation. *presented at the 25th Symposium (International) on Combustion*, 21, July 31 - August 5, 1994, The University of California, Irvine, USA.

[12] Libby, P.A. and Williams, F.A. "Fundamental Aspects". In Libby P.A. and Williams F.A., editors, *Turbulent Reacting Flows*, Topics In Applied Physics, Vol. 44, pages 1–43. Springer-Verlag, 1980.

[13] Lilleheie, N.I., Byggstøyl, S., and Magnussen, B.F. Numerical Calculations of a Methane Turbulent Diffusion Flame Using Detailed Chemical Kinetics in the Eddy Dissipation Concept. *SINTEF Norvegian Institute of Technology, Division of Thermodynamics*, December 16, 1989.

[14] Rhie, C. M. and Chow, W.L. Numerical Study of the Turbulent Flow Past an Airfoil with Trailing Edge Separation. *AIAA Journal*, 2:1527–1532, 1983.

[15] Dener, C. *GEMS: Geometry Modeling and Mesh Generation System: User's Guide - Release 3.3.* SAMTEK-ITC, Inc., Hirfanli Sokak 7/1, 06700 Gaziosmanpasa, Ankara - Turkey, 1994.

[16] Amtec Engineering, Inc., P.O. Box 3633 - Bellevue, WA 98009-3633. *Tecplot: Interactive Data Visuaization for Scientists & Enginners. Version 6 User's Manual*, 1998.

[17] Moreau, P., and Boutier, A. Laser Velocimetry Measurements in a Turbulent Flame. In *Sixteenth Symposium (Int.) on Combustion*, pages 1747–1756. The Combustion Institute, 1976.

[18] Chang, W.C. and Chen, J.-Y. "Reduced Reaction Mechanism for the Oxidation of CH_4 Lean Flames", 1990. `http://firebrand.me.berkeley.edu/griredu.html`.

[19] Zimont, V.L. Gas Premixed Combustion at High Turbulence. Turbulent Flame Closure Combustion Model. In F. Beretta, editor, *Proceedings of the Mediterranean Combustion Symposium - 99*, pages 1155–1165, Napoli, 1999. Istituto Ricerche Sulla Combustione - CNR.

[20] Zimont, V.L., Barbato, M. and Murgia, F. On the Limits of Industrial Premixed Combustion Simulation Models. In F. Beretta, editor, *Proceedings of the Mediterranean Combustion Symposium - 99*, pages 372–383, Napoli, 1999. Istituto Ricerche Sulla Combustione - CNR.

[21] Maas, U. and Pope, S.B. Implementation of Simplified Chemical Kinetics Based on Intrinsic Low-Dimensional Manifolds. In *Twenty-Fourth Symposium (Int.) on Combustion*, pages 103–112. The Combustion Institute, 1992.

[22] University of Heidelberg. Low Emission Systems Simulation Procedures for The Development of Fuel Efficient Combustor Technology (LES/PDF-ECT): Final Report. Technical Report Project N. BE 95-1927, Heidelberg University, Germany, April 19, 1999.

[23] Westbrook, C.K. and Dryer, F.L. Simplified reaction mechanisms for the oxidation of hydrocarbon fuels in flames. *Comb. Sci. and Techn.*, 27:31–43, 1981.

[24] Peters, N. Reducing Mechanisms. In M.D. Smooke, editor, *Reduced Kinetic Mechanisms and Asymptotic Approximations for Methane-Air Flames*, Berlin, 1991. Springer-Verlag.

[25] Mauss, F., and Peters, N. Reduced Kinetic Mechanisms for Premixed Methane-Air Flames . In N. Peters and B. Rogg, editors, *Reduced Kinetic Mechanisms for Applications in Combustion Systems*, pages 58–75, Berlin, 1993. Springer-Verlag.

[26] Rogg, B.,. Sensitivity Analysis of Laminar Premixed $CH_4 - Air$ Flames Using Full and Reduced Kinetic Mechanism. In Mitchell D. Smooke, editor, *Reduced Kinetic Mechanisms and Asymptotic Approximations for Methane-Air Flames*, Berlin, 1991. Springer-Verlag.

[27] M. Frenklach, H. Wang, C.-L. Yu, M. Goldenberg, C.T. Bowman, R.K. Hanson, D.F. Davidson, E.J. Chang, G.P. Smith, D.M. Golden, W.C. Gardiner and V. Lissianski,. "Detailed Kinetic Mechanism for Methane Oxidation", 1992. `http://euler.Berkeley.EDU/gri_mech/`.

[28] Holger Niemann. *Interface to ILDM-chemistry*. Interdisziplinäres Zentrum für Wissenschaftliches Rechnen - University of Heidelberg, 3 March, 1998.

[29] CFX International - AEA Technology. *CFX-4.2: solver*, December 1997.

[30] Bailly, P., Garréton, D., Simonin, O., Bruel, P., Champion, M., Deshaies, S., Duplantier, S., and Sanquer, S. Experimental and Numerical Study of a Premixed Flame Stabilized by a Rectangular Section Cylinder. In *Twenty-Sixth*

Symposium (Int.) on Combustion, pages 923–929. The Combustion Institute, 1996.

[31] Coltrin M.E., Kee, R.J. and Rupley, F.M. CHEMKIN-II: A FORTRAN Chemical Kinetics Package for the Analysis of Gas Phase Chemical Kinetics. Technical Report SAND89-8009B . UC-706, SANDIA Laboratories, 1989.

[32] Moreau, P.,. Turbulent Flame Development in a High Velocity Premixed Flow. *AIAA Paper 77-49, AIAA 18th Aerospace Science Meeting*, Jan. 24-25 1977, Los Angeles, CA.

Appendix A

EDC+PSR in CFX

A.1 Routines structure

The EDC-PSR routines are written in `FORTRAN 77` and are all in `DOUBLE PRECISION`. They are grouped into three blocks (see Fig. A.1):

- CFX Users routines
- EDC routines
- Chemkin routines

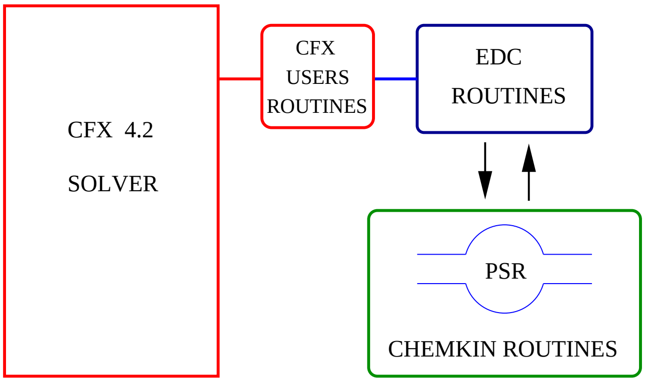

Figure A.1: Routines structure.

A.1.1 CFX Users routines

These routines are used to set up the source terms for chemical species and enthalpy transport equations inside CFX. Files of these routines can be found in the directory `CFX_RUN/Fort/CFX_USR_ROUTINES`.

A.1.2 EDC routines

These routines contain the Eddy Dissipation Concept Model implementation and the driver to call the Chemkin routines for solving the Perfect Stirred Reactor equations. Files of these routines can be found in the directory `CFX_RUN/Fort/PSR`.

A.1.3 Chemkin routines

These are the Chemkin-II package routines [8] to solve PSR equations. Specific routines have been written to calculate the reaction rates for the particular reduced reaction mechanisms. Files of these routines can be found in the directory `CFX_RUN/Fort/CHMKN`.

A.2 CFX Users routines in detail

A.2.1 USRSRC

This CFX-users routine has been used to include the source terms for the mean species mass fractions transport equations (Eq. 2.54)):

$$\tilde{w}_i = \frac{\dot{m}^* \gamma^* \chi \eta}{1 - \gamma^* \chi} \left(Y_i^* - \tilde{Y}_i \right) \qquad i = 1, ..., NS$$

Following the numerical approach used by CFX 4.2, the source term for the generic variable ϕ is linearized as:

$$S = S_U + S_P \phi_P \quad . \tag{A.1}$$

For mean mass fractions these terms read:

$$S_P = -\overline{\rho} V \frac{\dot{m}^* \gamma^* \chi \eta}{1 - \gamma^* \chi}$$

$$S_U(i) = \overline{\rho} V \frac{\dot{m}^* \gamma^* \chi \eta}{1 - \gamma^* \chi} \cdot Y_i^* \qquad i = 1, ..., NS$$

For the mean enthalpy equation the source term reads:

$$\tilde{\dot{Q}} = -\frac{\dot{m}^* \gamma^* \chi \eta}{1 - \gamma^* \chi} \sum_{i=1}^{NS} \left[\left(Y_i^* - \tilde{Y}_i \right) \Delta H_i \right] \tag{A.2}$$

where ΔH_i is the formation enthalpy for the chemical species i. It has been written (non linearized):

$$S_P = 0$$

$$S_U = -\bar{\rho} V \frac{\dot{m}^* \gamma^* \chi \eta}{1 - \gamma^* \chi} \sum_{i=1}^{NS} \left[\left(Y_i^* - \tilde{Y}_i \right) \Delta H_i \right] \quad .$$

The PSR solver call, which updates the Y_i^* is not done at each iteration, but each `NITEDC` iterations. This avoids to overload the CPU with `Chemkin` calculations. This procedure has a visible effect on the convergence history that shows wiggles which are synchronous with the PSR call. At the moment it is `NITEDC = 20`, but this value can be changed by the user by acting directly on the `USRSRC` FORTRAN routine (no input has been set for this variable).

A.3 EDC routines in detail

A.3.1 DRIVER_PSR

This subroutine calls the routine `PSR` of the Chemkin II package. Before calling the PSR solver it converts the mass fractions Y_i^* into molar fractions X_i^* (call to `XFROMY`). The reverse it is done after having the modified molar fractions (call to `YFROMX`).

A.3.2 EQRATIO_EDC

This subroutine set the filter to avoid the PSR calculation where it is not necessary. The filter for premixed combustion is based on mixture temperature whereas for non premixed combustion on temperature, equivalence ratio. The routine output is the flag `ERFLAG`:

`erflag = 1` – i.e. burning point, PSR calculation is on;

`erflag = 0` – i.e. non-burning point; PSR calculation is off.

Different `EQRATIO_EDC` routines have been set up for different fuels (see Makefile).

A.3.3 ETA_EDC

This subroutine calculates the quantity η (Eq. (2.55)):

$$\eta = \begin{cases} \frac{1}{\gamma} & \text{if} \quad \frac{1}{\gamma} \leq \eta_{lim} \\ \\ \eta_{lim} & \text{if} \quad \frac{1}{\gamma} > \eta_{lim} \end{cases}$$

where

$$\eta_{lim} = 1 + \frac{\tilde{Y}_{pr}}{\tilde{Y}_{min}(1 + r_{fu})}$$

A.3.4 INIT_PSR

This routine reads input files:

- `edc.inp`
- `namebin.inp`

and initializes:

- Chemkin package pointers (call to `PSPNT`)
- Chemkin binary file name
- Chemkin utility input files
- Chemkin utility output files
- ILDM tables file name
- Chemical species names (call to `NAMES_EDC`)
- Chemical species molar weights (call to `CKWT`)

A.3.5 NAMES_EDC

This subroutine sets chemical species names.

A.3.6 PSR_EDC

This subroutine is preliminary to the call of the PSR driver (`DRV_PSR_CFX`). For premixed combustion flows it sets:

$$T^\circ = \tilde{T}, \quad \rho^\circ = \tilde{\rho}, \quad Y_i^\circ = \tilde{Y}_i \quad \text{for} \quad i = 1, ..., NS$$

For the points where `erflag = 1` (see `EQRATIO_EDC`) the PSR mass flow rate is calculated:

$$\dot{m} = \dot{m}^* \rho^\circ \gamma^* V$$

and then the driver is called. Quantities passed to the PSR driver have units coherent with `Chemkin` standards: cm, gr, mole, atm. If the PSR run give a positive result the fine structure density ρ^* is updated (call to `RHOYT_EDC`). If the PSR run give a negative result, the routine assigns the “zero” values to the “starred” quantities:

$$T^* = T^\circ, \quad \rho^* = \rho^\circ, \quad Y_i^* = Y_i^\circ \quad \text{for} \ i = 1, ..., NS$$

A.3.7 RED_WYP

This subroutine calculates the chemical reaction rates which are used by the Chemkin PSR solver. Several version of this routine have been set up for CH_4, C_3H_8, and $C_{10}H_{22}$.

$$\dot{\omega}_i = \sum_{j=1}^{NR} a_{ij} \prod_{k=1}^{NS} [A_k]^{a_{kj}} \exp(Ea_j/\mathcal{R}T)$$

Specific reaction rates are set accordingly to the particular reduced reaction mechanisms. Corresponding files are:

- `red_wy_pet_ch4.f`: Methane, Peters (Section 6.2);
- `red_wy_wd_ch4.f`: Methane, Westbrook and Dryer (Section 6.1);
- `red_wy_wd_c3h8.f`: Propane, Westbrook and Dryer (Section 6.1);
- `red_wy_wd_c10h22.f`: Decane, Westbrook and Dryer (Section 6.1).

A.3.8 STAR_CFX

This subroutine calculate the EDC model fine structures characteristic quantities (mass flow rate, intermittency, burning probability).

Flow rate through fine structures per unit mass (Eq. (2.31)):

$$\dot{m}^* = (\frac{3}{C_{D2}})^{1/2}(\frac{\varepsilon}{\nu^*})^{1/2}$$

Mass fraction of fine structures regions (Eq. (2.30)):

$$\gamma = (\frac{3}{4}\frac{C_{D2}}{C_{D1}^2})^{1/4}(\frac{\nu^*\varepsilon}{\kappa^2})^{1/4}$$

Mass fraction of fine structures (Eq. (2.29)):

$$\gamma^* = 9.7(\frac{\nu^*\varepsilon}{\kappa^2})^{3/4}$$

The relation between fine structure regions and fine structure mass fractions is therefore:

$$\gamma^* = \gamma^\alpha \tag{A.3}$$

where $\alpha = 3$ in the original model. This exponent has been the main tuning parameter used for the combustion model; values $\alpha \leq 2$ have been found to give better agreement with experimental data. In any case, its value may depend on the specific test case.

The burning probability χ is assumed unit:

$$\chi = 1$$

A.3.9 XFROMY

This subroutine calculates molar fractions from mass fractions:

$$X_i = Y_i \cdot \frac{W}{W_i} \qquad i = 1, NS - 1$$

where

$$W = 1 / \sum_{i=1}^{NS} \frac{Y_i}{W_i}$$

Finally

$$X_{NS} = 1 - \sum_{i=1}^{NS-1} X_i$$

A.3.10 YFROMX

This subroutine calculates mass fractions from molar fractions:

$$Y_i = X_i \cdot \frac{W_i}{W} \qquad i = 1, NS - 1$$

where

$$W = \sum_{i=1}^{NS} X_i W_i$$

Finally:

$$Y_{NS} = 1 - \sum_{i=1}^{NS-1} Y_i$$

A.3.11 ZERO_EDC

This subroutine calculates the surrounding fluid related quantities (hereinafter called "zero" quantities) from Eq. 2.26, whereas "zero" density and temperature are obtained from state equation and enthalpy respectively. Mean temperature and density are then updated using Eq. 2.26.

In the premix test case this routine sets for the burning points (i.e., where `erflag = 1`):

$$T^{\circ} = \tilde{T}, \quad \rho^{\circ} = \tilde{\rho}, \quad Y_i^{\circ} = \widetilde{Y_i} \quad \text{for} \quad i = 1, ..., NS$$

and for the non burning points (`erflag = 0`) set also:

$$T^{*} = \tilde{T}, \quad \rho^{*} = \tilde{\rho}, \quad Y_i^{*} = \widetilde{Y_i} \quad \text{for} \quad i = 1, ..., NS$$

A.4 Chemkin routines in detail

A.4.1 General Information

The routines of the Chemkin-II package have been modified only to make them suitable to be called at running time by the CFD solver. This required to:

- modify the Chemkin memory space assignment which is done only once by the routine `INIT_PSR`.
- modify the PSR keyword input which is done by the routine `PSRKEY` (see in the following).
- exclude all the printing options to avoid unnecessary flow of data (the routine `PSPRNT` has been modified for this).
- Change the call to the routine which calculates the chemical rates of consumption (`RED_WYP`) to match it with the use of reduced chemical reaction mechanisms routines.

Modifies applied are made evident by the comment string `CMB`. The philosophy used is to modify as less as possible the original routines. Therefore, it is possible that a more deep programming revision of these routines can lead to better performances.

The only routine strongly modified is the `PSRKEY`. Therefore we will say some words about it in the following. For the other routines, the reader can understand the modifies having directly a look to the `FORTRAN` code.

A.4.2 PSRKEY

This subroutine is the modified version of the original Chemkin II Package `PSRKEY` routine. This routine sets the keywords for the PSR run. To make it faster, in the new version only the relevant choices have been retained. Some of the quantities which were set up here, as for example convergence criteria, have been included in a `DATA` block called `ATIM`

A.4.3 PSR

This routine drives the solution method for Eqs. (2.43) and (2.44) using an iterative Newton method. First attempt solution is obtained by calculating the equilibrium solution. Further information can be found in Ref. [8].

A.5 Makefile

The main `Makefile` is located in the `CFX_RUN` directory.

The Makefile has been set so that compilation of `FORTRAN` routines and linking can be done at once from the main directory. It calls automatically the auxiliary makefiles which are located in: `CFX_RUN/Fort/CHMKN`, `CFX_RUN/Fort/PSR`, and `CFX_RUN/Fort/CFX_USR_ROUTINES`. The files object once compiled in the different source code directories are linked in the main directory in to the files

- `m01.o` for CH_4;
- `m02.o` for C_3H_8;
- `m03.o` for $C_{10}H_{22}$;

Commands to produce these objects are:

- "*make prem_ch4*" to produce `m01.o` for CH_4;
- "*make prem_c3h8*" to produce `m02.o` for C_3H_8;
- "*make prem_c10h22*" to produce `m03.o` for $C_{10}H_{22}$.

A.6 Directories structure

The main directory is the `CFX_RUN` where the makefile to produce the object files is located. The structure of other directories can be seen in Fig. A.2.

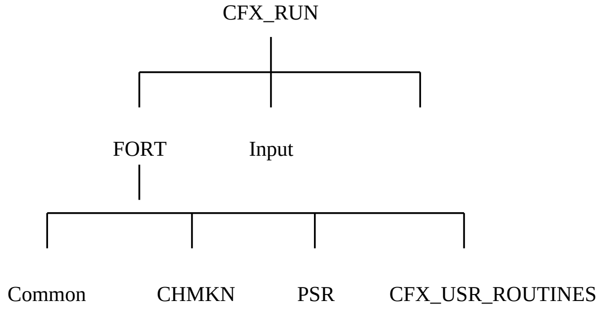

Figure A.2: EDC_PSR software for CFX: directories structure.

A.7 Auxiliary files

A.7.1 Common and Parameter files

Common and Parameter files are located in the directory `CFX_RUN/Fort/Common`.

- `parameter`: contains the maximum number of chemical species `NSPMX` for the EDC_PSR routines.
- `parameter_psr`: it assigns Chemkin vectors dimensions, and Chemkin input-output files and devices numbers
- `common_edc_inc`: it contains assignment and common areas for vectors used by the EDC_PSR routines.
- `common_edc_inp`: it defines EDC model related variables which are read from the file `edc.inp` and their related common areas. The flag `PREMIX` is defined here also.
- `common_names`: it defines character vectors and related common areas to store chemical species names.
- `common_psr`: `Chemkin` related integer assignment and common area which are used by the `PSR` routine.

A.7.2 Input files

- `edc.inp`: this file contains tuning parameters for the EDC Combustion Model:

  `FACTGM`: multiplicating factor for gamma (DOUBLE PRECISION);

  `LIMTGM`: limiter for γ (< 1) (DOUBLE PRECISION);

  `EXPGM`: exponent α for the $\gamma^* = \gamma^\alpha$ (DOUBLE PRECISION);

  `LIMTGMST`: limiter for γ^* (< 1) (DOUBLE PRECISION);

  `GMSTSET`: assigned constant value for γ^* (DOUBLE PRECISION);

  plus

  `PREMIX`: flag to discriminate between premix (1) and non premix (0) combustion (INTEGER);

  `PRS_EDC`: mean pressure of the flow in Pa (DOUBLE PRECISION) .

- `namebin.inp`: this file contains the Chemkin input binary file name (see next Section).

A.7.3 Chemkin binary files

Thermal data, molecular weight and chemical species names are stored in a binary files generated using the Chemkin-II package [31]. These files are those that in the Chemkin formalism are called **chem.bin**.

Usually these binary files contain, besides thermal data, chemical kinetics data for the specific chemical kinetics mechanism which are used by the Chemkin package routines. In our case the chemical consumption rates are set up directly from the specific reduced mechanisms (see routine `RED_WYP`), so the PSR solver needs information only about thermal data.

Therefore in the Chemkin file `chem.inp` we give just chemical elements and chemical species names in the order consistent with that used in the CFD code. For example for the Westbrook and Dryer two steps mechanism, 6 chemical species are involved (5 plus N_2 as inert gas).

```
ELEMENTS C H O N END
SPECIES CO2 H2O O2 CH4 CO N2 END
REACTIONS
END
```

No reactions are specified. Notice that N_2 must be always the last chemical species in the list.

Binary files are architecture dependent, therefore they have to be produced for the architecture on which the CFD code will run.

The name of the specific file to be used is defined as:

`chem_"mech"_"fuel".bin.`

and it is read by `INIT_PSR` (file `namebin.inp`).. For example for the Westbrook and Dryer mechanism for CH_4 oxidation the name is `chem_wd_ch4.bin`. Notice the specific file `chem.bin` for the chosen architecture *must* be put in the machine local directory `/tmp`.

Files already prepared are stored in the directory `CFX_RUN/Input/STORE_BIN`

A.7.4 CFX Command File

The CFX command file is presented in Appendix C. The main features which have to be underlined are:

- the flow is assumed to be COMPRESSIBLE in the approximation of WEAKLY COMPRESSIBLE flow (density depends on temperature but is not influenced by pressure fluctuations);

- CFX combustion features are not used. The flow is assumed to be a chemical reacting flow. Therefore the feature CHEMICAL SPECIES EQUATIONS has been used. This obliges to write equations for all chemical species involved (the BACKGROUND FLUID has not been used).

All other settings can be easily seen having a look to the CFX command file reported in the Appendix.

A.8 Example

As an example a test case is included in the package: it is the simulation of a CH_4 premixed flame in a plane combustor [17, 32]. In the directory `CFX_RUN` there are the files:

- `m01.geo` is the geometry file.
- `m01.fc` is the CFX command file.

The mechanism set to be used is the Westbrook and Dryer including 6 chemical species (N_2 as diluent).

For this test case convergence should be achieved with 5000 iterations.

Appendix B

Package usage check-list

The package has been set up to run CFX starting from the directory `CFX_RUN`. In this directory there are, in fact, the geometry and command files of CFX (e.g. m01.geo, m01.fc) and in this directory the makefile moves the object file.

- Define the fuel and the number of species involved in the reduced mechanism. Remember that this number has to be assigned to the parameter `NSCALEDC` in the `USRSRC` routine.
- Check the consistency of the chemical species order used in the CFX command file and for the `Chemkin` binary file `namebin.inp`. Remember that N_2 has to be always the last in the chemical species list.
- Copy the chemical source terms file for the specific reduced mechanism to the `red_wy_fuel.f` file.
- Compile the specific object file using make commands (see Section A.5);
- Check if the right name for the `Chemkin` binary file is updated in `namebin.inp`;
- Copy the fuel `Chemkin` binary file in the machine `/tmp` directory;
- Check the file `edc.inp` to define correctly EDC model parameters, kind of combustion and mean pressure;
- In the CFX "solve" menu check in "Advanced Options" to switch "Double Precision" ON and to set the number for the chosen object file (1, 2 or 3, see Section A.5).

Appendix C

CFX command file: example

```
>>CFX4
>>SET LIMITS
TOTAL INTEGER WORK SPACE 500000
TOTAL CHARACTER WORK SPACE 2000
TOTAL REAL WORK SPACE 2000000
MAXIMUM NUMBER OF BLOCKS 10
MAXIMUM NUMBER OF PATCHES 100
MAXIMUM NUMBER OF INTER BLOCK BOUNDARIES 20
END
>>OPTIONS
TWO DIMENSIONS
RECTANGULAR GRID
CARTESIAN COORDINATES
TURBULENT FLOW
HEAT TRANSFER
COMPRESSIBLE FLOW
STEADY STATE
CHEMICAL SPECIES EQUATIONS 6
MAXIMUM DEGREE OF POLYNOMIAL DEPENDENCE ON T 3
NUMBER OF PHASES 1
END
>>USER FORTRAN
USRSRC
END
>>VARIABLE NAMES
U VELOCITY 'U VELOCITY'
V VELOCITY 'V VELOCITY'
W VELOCITY 'W VELOCITY'
PRESSURE 'PRESSURE'
DENSITY 'DENSITY'
VISCOSITY 'VISCOSITY'
K 'K'
EPSILON 'EPSILON'
```

```
TEMPERATURE 'TEMPERATURE'
ENTHALPY 'ENTHALPY'
SPECIES1 'CO2'
SPECIES2 'H2O'
SPECIES3 'O2'
SPECIES4 'CH4'
SPECIES5 'CO'
SPECIES6 'N2'
END
>>UNITS
>>CHEMICAL SPECIES
MASS FRACTIONS
END
>>MODEL DATA
>>TITLE
PROBLEM TITLE 'EDC+PSR: MOREAU COMBUSTOR'
END
>>AMBIENT VARIABLES
U VELOCITY 6.5000E+01
V VELOCITY .0000E+00
PRESSURE .0000E+00
K 1.0000E+02
EPSILON 3.7000E+04
TEMPERATURE 6.0000E+02
CO2 .0000E+00
H2O .0000E+00
O2 2.2214E-01
CH4 4.6600E-02
CO .0000E+00
N2 7.3126E-01
END
>>SET INITIAL GUESS
>>SET CONSTANT GUESS
U VELOCITY 1.1000E+02
V VELOCITY .0000E+00
PRESSURE .0000E+00
K 7.9300E+02
EPSILON 2.8000E+06
TEMPERATURE 6.0000E+02
CO2 .0000E+00
H2O .0000E+00
O2 2.2214E-01
CH4 4.6600E-02
CO .0000E+00
N2 7.3126E-01
END
>>CHEMISTRY
```

```
>>CHEMICAL SPECIES PROPERTIES
>>REFERENCE STATES
>>ENTHALPY REFERENCE TEMPERATURE
ALL SPECIES 2.9800E+02
END
>>ENTROPY REFERENCE TEMPERATURE
ALL SPECIES 2.9800E+02
END
>>ENTROPY REFERENCE PRESSURE
ALL SPECIES 1.0133E+05
END
>>HEAT CAPACITY REFERENCE TEMPERATURE
ALL SPECIES 2.9800E+02
END
>>DIFFUSIVITIES
ALL SPECIES 4.1141E-05
END
>>MOLECULAR WEIGHTS
CO2 4.4000E+01
H2O 1.8000E+01
O2 3.2000E+01
CH4 1.6000E+01
CO 2.8000E+01
N2 2.8000E+01
END
>>SPECIFIC HEATS
CO2 5.708E+02 1.140E+00 -5.700E-04 1.000E-07
H2O 1.700608E+03 4.428E-01 2.3582E-04 -0.840E-07
O2 7.8768E+02 4.884E-01 -2.250E-04 0.400E-07
CH4 7.1074E+02 5.30568E+00 -1.7421E-03 1.960E-07
CO 9.47944E+02 2.8824E-01 -4.740E-05 -4.0E-09
N2 9.673192E+02 2.02232E-01 -1.5180E-05 -0.172E-07
END
>>MOLAR ENTHALPIES OF FORMATION
CO2 -3.9360E+08
H2O -2.4191E+08
O2 .0000E+00
CH4 -7.4902E+07
CO -1.1057E+08
N2 .0000E+00
END
>>MOLAR ENTROPIES AT REFERENCE STATE
CO2 2.1374E+05
H2O 1.8874E+05
O2 2.0507E+05
CH4 1.8606E+05
CO 1.9758E+05
```

```
N2 1.9155E+05
END
>>CHEMICAL REACTION SCHEME
>>REACTION
>>REACTION NAME
NAME 'FICTITIOUS CH4 OXIDATION !!!'
>>REACTANTS
CO2 .000000E+00
H2O .000000E+00
CH4 .000000E+00
O2 .000000E+00
CO .000000E+00
N2 .000000E+00
END
>>PRODUCTS
CO2 .000000E+00
H2O .000000E+00
CH4 .000000E+00
O2 .000000E+00
CO .000000E+00
N2 .000000E+00
END
>>FORWARD RATE
PREEXPONENTIAL FACTOR .0000E+00
ACTIVATION TEMPERATURE .0000E+00
TEMPERATURE EXPONENT .0000E+00
EDDY DISSIPATION MODEL
>>DEFAULT MIXING MODEL
EDDY DISSIPATION MODEL
>>CHEMISTRY SOLVER OPTIONS
NO BACKGROUND FLUID
MAXIMUM CORRECTION FACTOR .0000E+00
NUMBER OF PRELIMINARY OUTER ITERATIONS 10000
MAXIMUM NUMBER OF CHEMISTRY ITERATIONS 3
MAXIMUM MASS FRACTION CHANGE PER STEP 5.0000E-01
MAXIMUM TEMPERATURE CHANGE PER STEP 2.0000E+02
MASS FRACTION CORRECTION TOLERANCE 1.0000E-03
TEMPERATURE CORRECTION TOLERANCE 1.0000E+00
>>DIFFERENCING SCHEME
ALL EQUATIONS 'QUICK'
>>WALL TREATMENTS
WALL PROFILE 'LOGARITHMIC'
NO SLIP
>>PHYSICAL PROPERTIES
>>COMPRESSIBILITY PARAMETERS
WEAKLY COMPRESSIBLE
UNIVERSAL GAS CONSTANT 8.3140E+03
```

```
FLUID MOLECULAR WEIGHT 2.8000E+01
REFERENCE PRESSURE 1.0130E+05
>>FLUID PARAMETERS
VISCOSITY 1.5960E-05
>>HEAT TRANSFER PARAMETERS
THERMAL CONDUCTIVITY 2.2300E-02
COMBUSTION THERMAL DIFFUSIVITY 2.5857E-5
FLUID SPECIFIC HEAT 9.673192E+02 2.02232E-01 -1.5180E-05 -0.172E-07
ENTHALPY REFERENCE TEMPERATURE 2.8800E+02
>>TURBULENCE PARAMETERS
>>TURBULENCE MODEL
TURBULENCE MODEL 'K-EPSILON'
>>TURBULENCE CONSTANTS
CMU 9.0000E-02
C1 1.4400E+00
C2 1.9200E+00
C3 .0000E+00
CAPPA 4.1870E-01
END
>>TURBULENT PRANDTL NUMBER
K 1.0000E+00
EPSILON 1.2170E+00
ENTHALPY 9.0000E-01
CO2 9.0000E-01
H2O 9.0000E-01
O2 9.0000E-01
CH4 9.0000E-01
CO 9.0000E-01
N2 9.0000E-01
END
>>SOLVER DATA
>>PROGRAM CONTROL
MAXIMUM NUMBER OF ITERATIONS 15000
MINIMUM NUMBER OF ITERATIONS 15000
MASS SOURCE TOLERANCE 1.0000E-12
ITERATIONS OF TURBULENCE EQUATIONS 1
ITERATIONS OF VELOCITY AND PRESSURE EQUATIONS 1
ITERATIONS OF TEMPERATURE AND SCALAR EQUATIONS 1
ITERATIONS OF HYDRODYNAMIC EQUATIONS 1
SOLVER DEBUG PRINT STREAM 20
>>UNDER RELAXATION FACTORS
U VELOCITY 6.5000E-01
V VELOCITY 6.5000E-01
PRESSURE 1.0000E+00
VISCOSITY 1.0000E+00
K 7.0000E-01
EPSILON 7.0000E-01
```

```
ENTHALPY 7.0000E-01
CO2 7.0000E-01
H2O 7.0000E-01
O2 7.0000E-01
CH4 7.0000E-01
CO 7.0000E-01
N2 7.0000E-01
END
>>MODEL BOUNDARY CONDITIONS
>>INLET BOUNDARIES
PATCH NAME 'HOT-INLET'
U VELOCITY 1.1000E+02
V VELOCITY .0000E+00
K 7.9300E+02
EPSILON 2.8000E+06
TEMPERATURE 2.2400E+03
CO2 1.2134E-01
H2O 1.0466E-01
O2 3.8610E-02
CH4 .0000E+00
CO 4.1368E-03
N2 7.3126E-01
END
>>INLET BOUNDARIES
PATCH NAME 'COLD-INLET'
U VELOCITY 6.5000E+01
V VELOCITY .0000E+00
K 1.0000E+02
EPSILON 3.7000E+04
TEMPERATURE 6.0000E+02
CO2 .0000E+00
H2O .0000E+00
O2 2.2214E-01
CH4 4.6600E-02
CO .0000E+00
N2 7.3126E-01
END
>>PRESSURE BOUNDARIES
PATCH NAME 'OUTLET1'
PRESSURE .0000E+00
STATIC PRESSURE SPECIFIED
END
>>PRESSURE BOUNDARIES
PATCH NAME 'OUTLET2'
PRESSURE .0000E+00
STATIC PRESSURE SPECIFIED
END
```

```
>>INLET BOUNDARY CONDITIONS
VELOCITY SPECIFIED
>>STOP
```